

**Failure Mechanisms of Metallic Glasses via  
Atomic Scale Simulations**

by

Jian Luo

A Thesis Submitted to the Graduate  
Faculty of Rensselaer Polytechnic Institute

in Partial Fulfillment of the  
Requirements for the degree of  
DOCTOR OF PHILOSOPHY

Major Subject: Materials Science and Engineering

Approved by the  
Examining Committee:

---

Yunfeng Shi, Thesis Adviser

---

Liping Huang, Member

---

Pawel Koblinski, Member

---

Linda Schadler, Member

---

Catalin Picu, Member

Rensselaer Polytechnic Institute  
Troy, New York

December, 2014  
(For Graduation December, 2014)

© Copyright 2014  
by  
Jian Luo  
All Rights Reserved

# CONTENTS

LIST OF TABLES.....	vii
LIST OF FIGURES .....	viii
ACKNOWLEDGMENT .....	xv
ABSTRACT .....	xvii
1. Introduction.....	1
1.1 A brief history of metallic glasses.....	1
1.2 Metallic glasses as promising structural materials.....	1
1.3 Failure of metallic glasses.....	3
1.3.1 Failure of macroscopic samples.....	3
1.3.2 Failure of nano-scale samples .....	5
1.3.3 Failure modes and Poisson’s ratio.....	6
1.3.4 Fatigue failure of metallic glasses.....	7
1.4 Existing theories on the failure modes of metallic glasses .....	7
1.5 Existing simulation work on the failure mode of metallic glasses.....	10
1.6 Challenges and approaches .....	11
1.7 Outline of the thesis .....	13
2. Simulation Methods.....	15
2.1 Molecular dynamics simulations .....	15
2.1.1 Force fields.....	15
2.1.2 Ensembles .....	16
2.1.3 Boundary conditions .....	17
2.1.4 Mechanical tests in MD simulations .....	17
2.2 Force field tuning methods .....	18
2.2.1 Modified binary Lennard-Jones potential .....	19
2.2.2 Modified Stillinger-Weber potential .....	22

2.2.3	Modified BKS potential for silica system .....	24
3.	Intrinsic Ductility of Glassy Solids.....	26
3.1	Introduction .....	26
3.2	Simulation methodology .....	27
3.2.1	Interatomic force fields and potential tuning .....	27
3.2.2	Sample preparation.....	28
3.2.3	Mechanical testing procedures and conditions .....	30
3.3	The effect of potential tuning on the intrinsic ductility of amorphous samples.....	31
3.3.1	Uniaxial tension tests .....	32
3.3.2	Compact tension tests.....	33
3.4	Understanding BTB transitions: shear vs cleavage competition .....	35
3.4.1	Surface energy measurement .....	36
3.4.2	Shear band energy measurement.....	38
3.4.3	Comparing the shear band energy and surface energy.....	41
3.5	Link BTB transitions to the Poisson's ratio .....	41
3.5.1	A simple BTB model .....	44
3.6	Link angular constraint to the Poisson's ratio.....	46
3.6.1	The model of homogeneous harmonic bond.....	46
3.6.2	The model of homogeneous angular harmonic spring.....	47
3.7	Sample-size effects on the tensile ductility .....	50
3.8	Summary .....	52
4.	History-independent Properties of Running Shear Bands .....	53
4.1	Free volume in the running shear band .....	53
4.1.1	Introduction .....	53
4.1.2	Simulation methodology .....	55
4.1.3	The effect of quenching rate .....	56
4.1.4	The effect of temperature .....	58

4.1.5	The effect of strain rate .....	59
4.1.6	The effect of pressure.....	60
4.1.7	Summary .....	62
4.2	Liquid Feature of the Stress State in the Running Shear Band .....	62
4.2.1	Introduction .....	63
4.2.2	Simulation setup and methodology .....	64
4.2.3	Large-scale simulation in the mWA system .....	69
4.2.4	Small-scale simulation in the mWA system .....	70
4.2.5	The effect of temperature .....	72
4.2.6	The effect of shear flow .....	73
4.2.7	The effect of different glass formers .....	74
4.2.8	The effect of plastic confinement.....	76
4.2.9	Summary .....	77
5.	Size Dependent Tensile Fracture via Shear Band Cavitation .....	78
5.1	Introduction .....	78
5.2	Simulation methodology .....	80
5.2.1	Conventional uniaxial tension test .....	80
5.2.2	Perturbative static loading test .....	81
5.3	Size-induced ductile-to-brittle transition .....	83
5.3.1	Uniaxial tension test with PSL method.....	83
5.3.2	Thermomechanical evolution of the shear band .....	86
5.3.3	Mapping the thermomechanical condition for shear band cavitation ..	88
5.4	A thermomechanical model for shear band-to-crack transition.....	91
5.5	Summary .....	95
6.	Cavitation Map - A Concurrent Multiscale Simulation Study .....	96
6.1	Introduction .....	96
6.2	Multi-scale simulation setup .....	97

6.2.1	Elastic loading .....	98
6.2.2	Plastic loading .....	99
6.2.3	Temperature control during plastic loading .....	101
6.2.4	Verification of the multi-scale simulation method.....	103
6.3	Size dependent thermomechanical evolution of shear bands.....	103
6.4	Cavitation map .....	108
6.5	Summary .....	111
7.	Low Cycle Fatigue of Metallic Glass Nanowires.....	112
7.1	Introduction .....	112
7.2	Simulation methodology .....	113
7.3	Total-strain-controlled fatigue tests .....	114
7.4	Plastic-strain-controlled fatigue tests .....	117
7.5	Understand the power law from damage accumulation.....	119
7.6	Summary .....	121
8.	Conclusions and Outlooks .....	123
8.1	Conclusions .....	123
8.2	Outlooks .....	124
	References.....	126

## LIST OF TABLES

<b>Table 3.1. Sample dimension and preparation. The number in the bracket is the number of atoms in each sample. The amorphous nanowires are characterized by the radius <math>r</math> and the length <math>L</math>. The slab samples are for pure shear tests. The pre-cracked samples for compact tension tests are obtained from periodic duplication of these slab samples (<math>4 \times 4 \times 1</math> for the BLJ, <math>6 \times 6 \times 1</math> for SW systems and <math>3 \times 3 \times 1</math> for SW systems). .....</b>	<b>29</b>
<b>Table 4.1. The composition, the quenching rate, the sample size, the initial load <math>\sigma_L</math> and the testing temperature under NVT ensemble for the force fields employed in this study. Here compressive stresses are expressed as negative values.....</b>	<b>67</b>
<b>Table 5.1. The perturbation temperature <math>T_p</math> for PSL tests with different pre-strains. <math>T_p</math> was chosen to shorten the shear band formation time under tension. As shown in Fig. 5.2, a lower <math>T_p</math> leads to longer time for shear band formation, but identical fracture behavior for a sample just long enough to cause fracture at 5 % pre-strain. ....</b>	<b>83</b>
<b>Table 5.2. The material properties for the BLJ glass in the simulation and the <math>\text{Cu}_{46}\text{Zr}_{46}\text{Al}_8</math> glass in experiments.....</b>	<b>94</b>
<b>Table 6.1. Loading strain rate summary for different sized samples. The unit for strain rate is in Lennard Jones unit, which is <math>2ps^{-1}</math>. The common strain rate used is <math>10^{-4}</math>. ....</b>	<b>104</b>

## LIST OF FIGURES

**Figure 1.1. (a) A Zr-based fatigue pre-cracked metallic glass sample after bending test. The record-breaking fracture toughness is demonstrated by the exceptional crack shielding capability via profuse shear band formation. (b) The same Zr-based metallic glass before and after tensile testing. Nearly zero plasticity is observed. The fracture surfaces form an angle of 53 degrees to the loading direction. Both figures are taken from ref [17]..... 2**

**Figure 1.2. Illustration of the successive stages of shear banding and the resulted tensile fracture. (a) Nucleation of shear band. The shear band is believed to preferentially nucleate on the surface as denoted by the blue dot. (b) Propagation stage of shear band, which ends when the shear band penetrates the whole sample as in (c). The blue regions denote the propagating cold shear band. The arrow indicates the propagating direction. (d) The synchronized gliding of the two parts of the sample separated by the shear band. The temperature rises in the shear band<sup>37</sup>, which is illustrated by the red region. (e) The speculated cavitation process in the running shear band under tension. (f) The resulted tensile fracture with the corrugated fracture surfaces. .... 4**

**Figure 1.3. (a) Typical tensile fracture seen in macroscopic metallic glasses<sup>63</sup>. Bright field is the sample. (b) Ductile deformation up to 45% strain via non-catastrophic shear banding under tension for a nanometer scale sample.<sup>25</sup> Dark field is the sample and the frame. .... 5**

**Figure 1.4. (a) Intrinsically brittle behavior and (b) intrinsically ductile behavior. . 6**

**Figure 2.1. Comparison between the BLJ potential, the original Wahnstrom potential (essentially a shifted Lennard-Jones potential) and the Dzugutov potential. Both the distance and the potential energy are scaled to the proper internal length and energy units for each system. .... 21**

**Figure 2.2. Species-blind RDF curves (a) and ADF curves (b) are shown for glasses of the BLJ systems with  $\lambda$  from 0.25 to 0.375. .... 21**

**Figure 2.3. Schematic illustrations of the short range structure change in glasses of the BLJ systems with respect to the increasing bump height. .... 22**

**Figure 2.4. RDF curves (a) and ADF curves (b) are shown for glasses of the Stillinger-Weber systems with the prefactor of the angular term ranging from 21 to 33. .... 23**

**Figure 2.5. RDF curves (a) and ADF curves (b) are shown for glasses of the BKS systems with the OOR parameter ranging from 0.9 to 1.2. .... 24**

**Figure 3.1. Poisson's ratio for the BLJ, SW, and BKS systems as a function of  $\varepsilon_B$ ,  $\lambda$ , and OOR, respectively (a1, b1, and c1). True stress-true strain curves for bulk samples (a2, b2, and c2) and engineering stress-true strain for nanowire samples (a3, b3, and c3), for the BLJ, SW, and BKS systems under uniaxial tension tests, respectively. The sample morphologies for nanowire samples at 30% tensile strain (a4, b4, c4). It is clear that, for all three systems, BTD transition occurs as the bonding covalency decreases. Atoms are colored according to the local shear strain (red refers to 0% strain while yellow refers to 20% strain or above) as shown at the bottom..... 32**

- Figure 3.2.** Deformation distribution morphologies for compact tension tests samples with pre-existing cracks, below which the corresponding true stress-true strain curves are shown. High covalency in bonding leads to weak resistance to crack growth. The precise sample dimensions can be found in Table 3.1. The color scheme is identical to that in Figure 3.1..... 34
- Figure 3.3.** (a) Schematics of the competition in terms of the energy costs between cleavage and shear for a cylindrical sample under uniaxial tension: (left pane) sample in tension with stored elastic energy; (middle pane) cleavage releases elastic energy, but is penalized energetically for the newly created surfaces; (right pane) shear slip also releases elastic energy, but is penalized energetically for the extra potential energy within the shear band region.  $\theta$  is the shear band normal relative to the loading condition. The energy cost for shear, in terms of the shear band energy  $\gamma_{sb} / \cos(\theta)$ , and the energy cost for cleavage, in terms of the surface energy  $2 \cdot \gamma_{sf}$ , are plotted for BLJ (a), SW (b), and BKS (c) systems as a function of  $\varepsilon_B$ ,  $\lambda$ , and *OO*R, respectively. Surface energies with different definitions are also plotted ( $\gamma_{sf}^{unrelax}$ ,  $\gamma_{sf}^{ad}$  and  $\gamma_{sf}^{isothermal}$  refer to unrelaxed, adiabatically relaxed and isothermally relaxed surface energy, respectively). The angle  $\theta$  is taken as 45 degrees for simplicity. The small negative value for the BLJ system with high covalency is due to the presence of a low-density poly-amorphous state (more details in the text)..... 35
- Figure 3.4.** The deformation morphologies of pure shear tests on bulk amorphous samples with thin-slab geometries. The pure shear is conducted by tension in the X-direction and compression in the Y-direction with equal and opposite stresses. The Z-direction (thickness direction) is stress-free. The snapshots were taken at 12% of pure shear strain. The atoms are colored according to their local shear strain. Gray and black corresponds to 0% to 30% local shear strain, respectively. .... 39
- Figure 3.5.** The stress-strain curves for pure-shear tests on bulk amorphous samples with thin-slab geometries: (a1) BLJ; (b1) SW; and (c1) BKS systems. The potential energy increase due to shear band formation (excluding elastic energy stored) is plotted in (a2, b2, and c2) for BLJ, SW, and BKS systems, respectively. .... 40
- Figure 3.6.** The  $\nu$ -*CN* diagram showing the ductile regime and the brittle regime for three families of glassy solids (with zoomed-in views at the bottom). Amorphous samples exhibit either ductile (blue squares) or brittle behaviors (red crosses), depending on their covalency, processing, or testing conditions. The designation of brittle or ductile behaviors is according to the failure strain (Fig. 3.1) in uniaxial tension tests of bulk samples. The black dashed line of  $\nu_{BTD}$ -*CN* is from the simple model described in Eq. (3.9). .... 43
- Figure 4.1.** Simulation cell showing a snapshot of the atomic configuration (red and blue atoms represent Zr and Cu, respectively). Simple shear deformation is applied under isothermal-isobaric conditions. The three normal stresses are controlled independently to keep the same constant values. Periodic boundary conditions are applied in the three directions of the coordinate system..... 55

- Figure 4.2.** (a) Evolution of sample volume during isothermal simple shear deformation under zero hydrostatic stress and at  $T = 60\text{K}$  for samples quenched with various quenching rates,  $\Theta$ . The shear strain rate used is  $0.5 \text{ ns}^{-1}$ . (b) shear induced volumetric strain as a function of quenching rate. .... 57
- Figure 4.3.** (a) Variation of the volume of the as-quenched (aq) and steady shear (SS) states of G0.1 and G-instant samples with the temperature imposed during shear deformation,  $T$ . (b) The corresponding shear-induced volumetric strain as a function of temperature. .... 58
- Figure 4.4.** Volume of the steady shear state as a function of the shear strain rate for simple shear deformations performed at zero hydrostatic stress and  $T = 60 \text{ K}$ . .... 59
- Figure 4.5.** Evolution of sample volume during isothermal simple shear deformation under hydrostatic pressure (a)  $P = 8 \text{ GPa}$  and (b)  $P = -12 \text{ GPa}$ , and at  $T = 60\text{K}$  for samples quenched with various rates,  $\Theta$ . The shear strain rate used is  $0.5 \text{ ns}^{-1}$ . (c) Schematic illustration of the variation of volume with pressure for the SS state and the as-quenched state of G-instant and G0.1. (d) Volumetric strain as a function of pressure,  $P$ , for samples quenched with various rates. .... 61
- Figure 4.6.** The schematic illustration of the simulation setups. The left pane represents the uniaxial loading mode, in which the shear band is illustrated by the yellow region. The angle of the shear band away from the loading is  $\theta$ . Note that  $\sigma_L$  can be compressive or tensile. The right pane represents a simplified simulation setup for the small-scale simulations to explore more general loading conditions. The sample is first loaded in a general stress state with controlled normal stresses. Subsequent simple shear deformation to a large strain is applied to drive a shear band under the condition of fixed volume. .... 65
- Figure 4.7.** The local normal stresses distribution along  $z$  direction (perpendicular to the shear band) in PSL tests under tensile loading once a shear band forms across the sample with  $\theta = 39^\circ$  in (a) and  $\theta = 57^\circ$  in (b). .... 69
- Figure 4.8.** The deformation morphologies (colored by atomic shear strain, with blue corresponding to 0 strain and red corresponding to strain of 20% and above) and the corresponding local normal stresses distribution along the  $z$  direction before (a) and after (b) shear band formation. The applied shear strain is 6% and 8% in (a) and (b) respectively. The  $\theta$  parameter is set to be 0 degree. The local normal stresses become equal to each other at the location where the shear bands formed as indicated by the arrows. .... 71
- Figure 4.9.** The evolution in time of the local stress at the location where the shear band forms in simulations under NVE ensemble with the parameter  $\theta$  set from  $0^\circ$  to  $90^\circ$  in (a) to (d). The local HS stress state was achieved when the shear bands forms, independent of  $\theta$  .... 72
- Figure 4.10.** The evolution of the local stresses at the location where the shear band forms under the NVT ensemble with the temperature at  $10 \text{ K}$ . A representative result with the  $\theta$  parameter to be  $0^\circ$  is shown. (b). As a

- continuation of the tests in Fig. 4.9, relaxation without any deformation is conducted from 2.1 ns to 4 ns, as is indicated by dashed line. After 4 ns, shear deformation is resumed. A representative result with the  $\theta$  parameter to be  $0^\circ$  is shown..... 73
- Figure 4.11.** The evolution in time of the local stresses at the location where the shear band forms for the labeled force fields. The simulations are kept under the NVT ensemble with very low temperature (listed in Table 4.1). Representative results with the  $\theta$  parameter set to  $0^\circ$  are shown. The local HS stress state was achieved within atomic fluctuation in all these glasses when the shear band forms except in the FeP system and the SW-Si system. .... 75
- Figure 4.12.** The evolution in time of the local stresses at the location where the shear band forms in simulations with the  $\theta$  parameter set to  $0^\circ$  for the SW-Si system with modified angular constraint. The simulations are kept under the NVT ensemble with the temperature at 1 K..... 76
- Figure 5.1.** Conventional uniaxial tension tests of an amorphous slab. The left pane shows the stress-strain curve. The right pane shows the atomic configurations at 6% and 20% strain. The atoms are colored according to the local shear strain from blue (0% strain) to red (20% strain). A dominant shear band is apparent, which is similar to the experiment [<sup>25</sup>]. .... 81
- Figure 5.2.** The tensile stress-time curves in PSL tests for samples with different perturbation temperature  $T_p$ . The pre-strain is 5.0 %. The sample length is 360 nm, just long enough for tensile fracture (as shown in Fig. 5.4). The diamond symbol in each curve indicates the formation of the across-sample shear band and the circle symbol indicates the moment the first cavity appears in the shear band. The initial stress plateau corresponds to the shear band initiation or nucleation. Lower values of  $T_p$  increase the stress plateau duration and delay the shear band initiation, but do not suppress the subsequent fracture behavior of the sample. Cavitation only takes about 0.15 ns (from the diamond symbol to the circle) for this sample, independent of the shear band nucleation time. .... 82
- Figure 5.3.** (a) The overall tensile stress  $\sigma$  (solid lines) and shear off distance  $S$  (dashed lines) during PSL tests on samples with lengths of 180, 260, 360 nm (red, green, blue), with 5% pre-strain. (b) The local stress (solid lines) and temperature (circles) inside the shear band during PSL tests on the 360-nm-long sample with 5% pre-strain. The shear-band-based coordination system is shown in pane (c). The local thermomechanical states were coarse-grained and averaged according to a shear band angle  $\theta = 51^\circ$ . The resolved tensile stress  $\sigma \sin^2 \theta$  (blue dashed line) and shear stress  $\sigma \sin \theta \cos \theta$  (red dashed line) were also shown. (c) The morphology evolution of the samples during PSL simulations. The color represents the local temperature (1.6 nm-grid-size): blue for 0 K; red for 175 K and above. (d) Zoom-in atomic view of the shear band cavitation (black box region in pane c). .... 84
- Figure 5.4.** The PSL test results (red crosses denote fracture and blue circles denote no fracture) for samples with different lengths and the initial tensile stress.

Pre-strains were also given. The black dashed line shows the critical cavitation condition predicted by Eq. (5.7), without any free parameter. .... 85

**Figure 5.5.** Cavitation map in the normal stress ( $\sigma_{zz}$ ) and temperature (T) domain with the thermomechanical state evolution of the shear band during PSL tests for: (a) samples with lengths of 180, 260, 360 nm at 5% initial pre-strain; (b) samples with a length of 360 nm at pre-strains of 4, 4.5, 5.0 %. The thermomechanical states are the average over the shear band with a width of 0.89 nm. The critical cavitation conditions (black circles) were obtained from all PSL tests ending with fracture, with a linear fit as the cavitation line. .... 87

**Figure 5.6.** (a) The critical thermomechanical states for cavitation were mapped in the  $\sigma_{zz} - T$  domain from small-scale simulations with (solid lines) and without shear (broken lines). The error bar is calculated based on the results of five independent samples. In the label,  $\dot{\epsilon}$  and  $\dot{\gamma}_{zx}$  represent the hydrostatic tension strain rate and the shear strain rate. The cavitation stress decreases almost linearly with increasing temperature under pure hydrostatic tension. With shear flow, the cavitation stress at given temperature decreases dramatically with increasing  $\dot{\gamma}_{zx} / \dot{\epsilon}$ . (b) The critical thermomechanical states for cavitation (squares for hydrostatic tension tests; triangles and diamonds for hydrostatic tension with shear; circles for PSL tests) were mapped in the  $\sigma_{zz} - \sigma_{zx} - T$  domain for more values of  $\dot{\gamma}_{zx} / \dot{\epsilon}$ . The symbols were colored by temperature (green represents 0 K and yellow represents 328 K), with a color contour guiding the eye. The strain rate ratio  $\dot{\gamma}_{zx} / \dot{\epsilon}$  is given in the legend (groups of points with the same  $\dot{\gamma}_{zx} / \dot{\epsilon}$  are denoted by the dashed lines). .... 89

**Figure 5.7.** Gliding distance (S) as a function of time in PSL tests for samples with various lengths and pre-strains. The sliding starts with a parabolic increase in the gliding distance, almost independent of the sample length. For instance, at the 4% pre-strain (top-right pane), the S-t curves overlap very well once the curves are shifted horizontally accounting for differences in time when gliding begins. The only exception is the shortest sample with the highest pre-strain. Gliding velocity ( $\dot{s}$ ) can be calculated straightforwardly, from which the initial gliding acceleration ( $\ddot{s}$ ) can be obtained as shown in Fig. 5.8. .... 92

**Figure 5.8.** The initial acceleration ( $\ddot{s}$ ) in PSL tests as a function of the initial resolved shear stress ( $\sigma_i \sin \theta \cos \theta$ ). All PSL data (data shown in Fig. 5.7) is included except for the shortest sample with the highest pre-strain. The linear fitting provides  $\tau_f = 0.59$  GPa and  $d = 31$  nm according to Eq. (5.3), with  $\rho = 7142$  kg/m<sup>3</sup>. .... 93

**Figure 6.1.** Illustration of the plastic loading in the multi-scale simulation strategy. (a) The whole sample is under the tensile loading stress  $\sigma_L$  imposed by the continuum model. Yellow region represents the shear band. Red region is the small portion treated in MD simulation. The upper part of the sample glides along the shear band with a speed  $v_g(t)$  relative to the lower part. The gliding

- distance along the shear band is  $S_g(t)$ . (b) An “spring-shear band-spring” composite as an analogy to (a). (c) The flow chart of the multi-scale simulation during the plastic loading..... 97
- Figure 6.2. Stress and strain analysis during elastic loading before the shear band forms in the light green small slab in MD simulation. The red dash line indicate the orientation of the to-be-formed shear band..... 98
- Figure 6.3. Temperature coupling between MD simulation and continuum model. In the MD simulation, we slice the sample parallel to the shear band and record and feed the continuum model with the temperature in each slice. Then the continuum model updates the whole temperature profile and feeds the boundary temperatures back to the MD simulation. The middle part of the portion in MD simulation is kept in an NVE ensemble..... 102
- Figure 6.4. Thermomechanical evolution of the shear band in samples with listed length under original yield strength or artificially increased strength. There is a limit for temperature rise in the shear band, indicated by  $T_h$ , if the sample does not fracture. .... 105
- Figure 6.5. (a) Trajectories of the shear band in the domain of  $\sigma_z$  and  $T$  for the modified BLJ samples with sizes from 440 nm to 88  $\mu m$ . Red crosses indicate the cavitation states. (b) Cavitation states collected from the multi-scale simulations and full atomic simulations using perturbative static load (PSL)<sup>105</sup>. (c) Close-up view of the vicinity of the shear band the 0.88  $\mu m$  sample at the moments indicated by the dark green circles in (a)..... 106
- Figure 6.6. The cavitation stress a function of temperature in small scale hydrostatic tension tests with or without shear flow for (a) BLJ, (b)  $Cu_{50}Zr_{50}^{138}$ , (c)  $Zr_{50}Cu_{50}^{100}$ , and (d)  $Fe_{80}P_{20}^{139}$ . For BLJ, the strain rate  $\dot{\epsilon}$  and  $\dot{\gamma}$  are in the unit of 0.2 ns<sup>-1</sup>. For the other model glasses, the strain rate  $\dot{\epsilon}$  and  $\dot{\gamma}$  are in the unit of 0.5 ns<sup>-1</sup>..... 107
- Figure 6.7. The cavitation map. When  $\sigma_y \sin^2 \theta$  is smaller than  $\sigma_c(T_h)$ , the shear band trajectory is confined in the light green region in the thermomechanical domain, where no cavitation is expected to happen. When  $\sigma_y \sin^2 \theta$  is larger than  $\sigma_c(T_h)$ , the cavitation in the shear band will depend on sample size. If the sample size is larger, the shear band trajectory (black curve) has a higher possibility to touch the cavitation line (red line). If the sample size is small, the shear band trajectory (blue curve) can avoid the cavitation line. .... 108
- Figure 7.1. (a) The peak compression (negative) and tension (positive) stress during total-strain-controlled compression-tension fatigue tests. The applied total strain magnitudes are given in the legend. The stress amplitude decreases sharply towards fatigue fracture. (b) A representative stress-strain hysteresis loop for a fatigue test with a 6% strain amplitude. The strains are positive in tension and negative in compression. As indicated, the plastic strain is defined as half of the strain difference between the two zero-stress points. (c) The plastic strain of every cycle during typical total-strain-controlled fatigue tests.

The cycles are shown on a log scale. The applied total strain magnitudes are given in the legend..... 114

**Figure 7.2.** The side and top views of the deformation morphology of the model metallic glass nanowires during total-strain-controlled fatigue tests with strain amplitudes of 4% (upper panel), 5% (middle panel) and 6% (lower panel). Each arrow indicates the location of the crack inside the shear band after fracture. The atoms were colored according to the local shear strain. The opacity of atoms is also controlled by the local shear strain such that an atom with a shear strain lower than 0.2 is invisible and an atom with a shear strain higher than 0.6 is fully opaque..... 116

**Figure 7.3.** (a) The plastic strain  $\varepsilon_p$  as a function of the cycle number during plastic-strain-controlled fatigue tests. All five parallel tests are shown, each with initial total strain magnitude of 4% (black), 4.5% (red), 5% (green), 5.5% (blue) and 6% (orange), respectively. (b) Fatigue life as a function of plastic strain for all samples in a log-log plot. The red line is the best fitting according to the Coffin-Manson relation  $\varepsilon_p = \varepsilon_f N_f^c$ , where  $\varepsilon_f = 0.118$  and  $c = -0.6$ .... 117

**Figure 7.4.** (a) Accumulative damage  $D$  as a function of the cycle number in plastic-strain-controlled fatigue tests in a log-log plot. According to the damage evolution relation  $D = K(\varepsilon_p)N^\alpha$ , the exponent  $\alpha$  is taken as 1.5, independent of the plastic strain. All five independent tests are shown, each with the initial total strain amplitudes of 4% (black), 4.5% (red), 5% (green), 5.5% (blue) and 6% (orange), respectively. The damage at fracture  $D_f$  and life  $N_f$  are shown in the inset with the same color coding. (b) The prefactor  $K$ , defined as  $D/N^\alpha$ , is plotted as a function of the plastic strain  $\varepsilon_p$ . The red line is fitted by  $K = A\varepsilon_p^\beta$ , where  $A = 11.8$  and  $\beta = 2.4$ . (c) Accumulative damage  $D$  are plotted as a function of  $N^\alpha \varepsilon_p^\beta$  ( $\alpha = 1.5$  and  $\beta = 2.4$ , obtained from fitting of the previous two panes) in a log-log plot, showing data collapse for all samples under different plastic strains with an apparent slope of 1..... 120

## ACKNOWLEDGMENT

This work is powered by Dr. Yunfeng Shi's determined will to push the limit of MD simulations and keen insights on amorphous solids. Without his guide and persistent encouragement, four year's exciting research certainly would not be possible. I am also extremely grateful for the superb computing resources provided by Dr. Shi. Due to the large and long simulations required by my work, I almost single-handedly forced him to buy new hard drives for data storage. It is his strong support that enabled this work to be done in a timely fashion. My special thanks also go to his lasting passion for basketball, which brought me back from "retirement" to enjoy basketball again. We certainly had some amazing basketball time in the Mueller center and ECAV (excellent basketball court provided by RPI).

My research also benefits tremendously from the expertise and kind guidance from my stellar committee members. Dr. Liping Huang (and Dr. Shi) has been here every group meeting sitting through the frustration from my crowded slides, and guided me to think straight and to present clearly. The authentic Chinese food prepared by Dr. Huang (and Dr. Shi) on the group dinner at the end of every semester is what we all look forward to at the beginning of every semester. Dr. Catalin Picu is kind to provide extensive guide on conventional mechanics and extended to me the chance of an invited paper. I am very grateful for his personal encouragement and care. Dr. Pawel Keblinski's guidance on the sophisticated temperature control enabled my multiscale simulation. His insightful and interesting question style inspired me during every seminar. Dr. Linda Schadler's question of "how can we call metallic glasses tough when it's so brittle" has been an essential element of this work. I am also very grateful for her long lasting impact on me to improve my writing style and time management. Due to her suggestion, I thought and read extensively on the writing style and hopefully have made some progress to make the thesis more enjoyable to read.

This work was also inspired by the excellent work done in this field. I was fortunate to have eye-opening personal discussions or collaborations with some of the authors, who include but are not limited to Prof. Peter Liaw, Prof. Karin Darnen, Prof. Michael

Demcowicz, Prof. Michael Falk, Prof. Egami Takeshi, Prof. Evan Ma, Prof. John Lewandowski and Prof. Julia Greer.

I am also grateful for the help, encouragement, good humor and memories from all the colleagues and alumni from Dr. Shi and Dr. Huang's group- Dr. Xi Mi, Dr. Qing Zhao, Dr. Yanping Chen, Dr. Fenglin Yuan, Dr. Junwei Wang, Dr. Ashish Mishra, Michael Guerette, Kisung Chae, Muhammed Vargonen, Magdalene Pride, Qiran Xiao, Nicholas Tantisujjatham, Yongjian Yang, Garth Scannell, Siddharth Sundararaman, Siva Priya Jaccani and Binghui Deng. Special thanks for Nicholas Tantisujjatham's excellent help on the cluster recognition program.

This work received financial support from the National Science Foundation-United States under grant DMR-1207439 and computational support from XSEDE under award TG-DMR130089 and from the Center for Computational Innovations at Rensselaer Polytechnic Institute.

Finally, my special thanks go to my girl friend, Siyao Peng, for her supporting me through all the ups and downs, and my Mom, my Dad and the whole family in China for their warm support and best wishes.

## ABSTRACT

Metallic glasses (MGs) are an emerging class of structural materials that can achieve a combination of striking mechanical properties, such as high strength, large elastic limit, high fracture toughness, plastic-like processability, etc. However, the wide application of MGs in daily life is largely hindered by their extreme tensile brittleness and the uncertainty in their fatigue behavior. The underlying failure mechanisms are experimentally intractable due to spatiotemporal limitations.

Here, we designed several novel atomic simulation methods to reveal atomic insights on the tensile and fatigue failure mechanisms. Under tension, we found that the failure of MGs is triggered by cavitation and that the fast shear flow can decrease MGs' resistance to cavitation by a surprisingly large amount, which explains the extreme tensile brittleness. Under cyclic loading, we found that the life of MG nanowires follows the Coffin-Manson relationship, which can be further derived from the plastic strain controlled microscopic damage accumulation. By force field tuning methods, we demonstrated that the propensity of both the tensile brittleness and the fatigue failure of MGs is correlated with Poisson's ratio and the degree of covalency in the bonding. The atomic insights discovered here shed light on how to improve the tensile ductility and reliability of MGs, via tuning the elastic properties, thermal properties and sample size.

# 1. Introduction

## 1.1 A brief history of metallic glasses

Metals or alloys with amorphous structure were first made in the form of thin ribbon in the 1960's<sup>1</sup> by cooling from the melt with quenching rate higher than  $10^6$  K/s. The metallic glasses in the “bulk” form began to appear in the 1970's and 1980's as the critical cooling rate decreased to  $10^3$  K/s in Pd and Au based metallic glasses<sup>2,3</sup>. Since 1990's, multi-component metallic glasses have been intensively studied<sup>4,5</sup>. Many bulk metallic glasses made of less rare metals, such as Cu, Fe, La and Ca, emerged<sup>6</sup> as the critical cooling rate to prevent crystallization can get as low as 1 K/s.<sup>7</sup> So far, more than 30 elements have been reported as the components in metallic glasses<sup>4,6,8</sup>. Most metallic glasses require at least two, usually more than three, components to avoid crystallization, although single component metallic glass nanowires have been made recently under ultrafast quenching rate<sup>9</sup> around  $10^{14}$  K/s. The wide choices in the constitutional components and compositions hold wide possibilities in the design of metallic glasses. But it is challenging to efficiently search the vast compositional space for a desired glass former. Recent break-through in the combinatorial development of metallic glasses makes it possible to simultaneously fabricate and characterize 3000 alloy compositions<sup>8</sup>, which will significantly accelerate the discovery of more and better metallic glasses.

## 1.2 Metallic glasses as promising structural materials

As an emerging class of materials, metallic glasses attract a lot of attention primarily due to their unique mechanical properties<sup>10</sup>. Metallic glasses can simultaneously achieve very high strength<sup>10,11</sup>, high elastic limit (2% at macroscopic level<sup>12</sup> and more than 5% at nano-scale<sup>13,14</sup>), high hardness<sup>4</sup>, excellent wear and corrosion resistance<sup>4</sup> and even high fracture toughness<sup>15</sup>. In fact, the recently developed Pt-based and Zr-based (shown in Fig. 1.1a) metallic glasses are the most damage tolerant engineering materials in the world<sup>16,17</sup>, with a yield strength larger than 1.5 GPa and record-breaking fracture toughness larger than  $150 \text{ MPa}\sqrt{\text{m}}$ . Importantly, bulk metallic glasses also possess

plastic-like processability<sup>18,19</sup>, which paves the way for the convenient industrial scale production.

However, tensile ductility of metallic glasses is severely limited. This is particularly surprising when we consider that even the metallic glasses with record-breaking fracture toughness still have near zero tensile ductility<sup>16,17</sup> (shown in Fig. 1.1b) and that extensive ductility can be achieved under compression and bending<sup>20–23</sup>. The yield strength of metallic glasses was recently found to be notch insensitive<sup>24</sup>, which further indicates that the tensile brittleness in metallic glasses is fundamentally different from conventional brittle materials like ceramic glasses. Interestingly, when the sample size is reduced to the nano-scale, tensile ductility can be achieved<sup>25–27</sup>, suggesting a strong size effect.

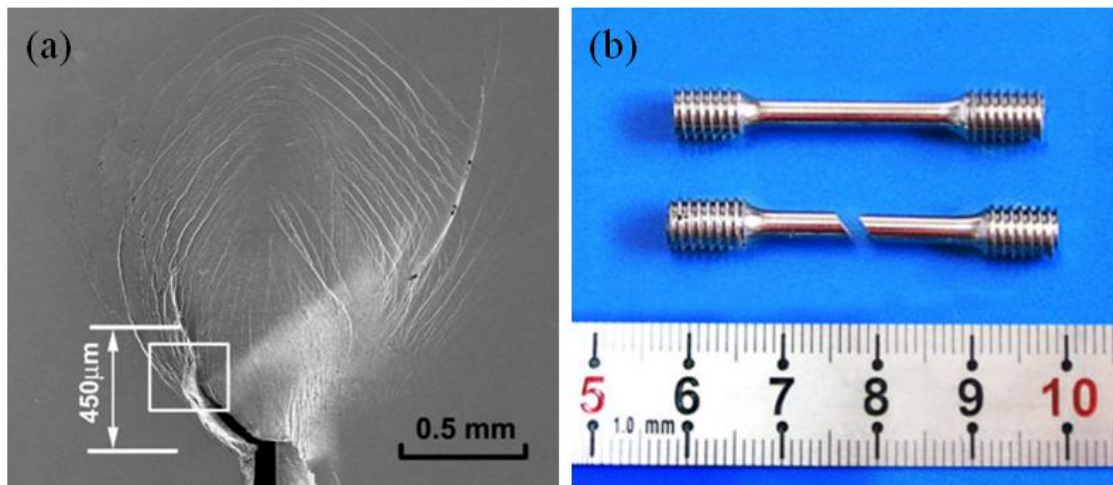


**Figure 1.1.** (a) A Zr-based fatigue pre-cracked metallic glass sample after bending test. The record-breaking fracture toughness is demonstrated by the exceptional crack shielding capability via profuse shear band formation. (b) The same Zr-based metallic glass before and after tensile testing. Nearly zero plasticity is observed. The fracture surfaces form an angle of 53 degrees to the loading direction. Both figures are taken from ref [17].

Another potential drawback of metallic glasses as structural materials is the uncertainty in their fatigue property. Fatigue property is important because fatigue failure accounts for more than 90% of mechanical failure in daily life<sup>28</sup>. For the macroscopic metallic glass samples, large discrepancy exists in the reported fatigue limits<sup>29–31</sup> and the fatigue-life properties are not well understood<sup>10</sup>. The understanding of

fatigue properties for nanometer sized metallic glasses is nearly blank. Nanometer-scaled metallic glasses are well suited for applications in the fields of microelectromechanical<sup>32</sup>, nanoelectromechanical systems<sup>33</sup>, micromachines<sup>34</sup> and biomedical applications<sup>35</sup>, as they possess an even better suite of mechanical properties, such as higher elastic limit<sup>13,14,26</sup>, higher strength<sup>26,36</sup> and higher ductility<sup>25,26,36</sup>, than their macroscopic counterparts. However, without a clear understanding of the fatigue properties, the reliability of such systems made of nanometer-scale metallic glasses is unknown, limiting their application.

## 1.3 Failure of metallic glasses

### 1.3.1 Failure of macroscopic samples

Catastrophic tensile failure of metallic glasses is mostly caused by shear banding<sup>10</sup>, the major plastic deformation mode of metallic glasses. Shear banding refers to the localization of plastic deformation into a band with a thickness of only 10~20 nm<sup>37-39</sup>. Several stages can be identified during shear banding<sup>40</sup> as illustrated in Fig. 1.2. The first stage is the nucleation of the embryo shear band as shown in Fig. 1.2(a). This stage was often considered as the stress driven shear transformation of several hundred atoms<sup>12,41,42</sup> acting like an Eshelby inclusion<sup>43-45</sup>. A most recent study suggests that the nucleation of a shear band involves less than ten atoms<sup>46</sup>. Once the shear band is nucleated, the shear band will continue to grow in an autocatalytic manner<sup>44,47,48</sup> with a propagating tip, comprising the second stage. Both the nucleation and the propagation of shear band are a form of structural transformation of local stable atomic clusters to less ordered ones, as was first suggested in the early experimental studies<sup>49,50</sup> and later in atomic simulations<sup>51-53</sup>. The propagation speed of the shear band tip was believed to be close to the speed of sound<sup>47,53</sup>. Therefore the second stage is so brief that it still has not been directly observed with state-of-the-art high-speed imaging techniques<sup>54,55</sup>. The third stage begins when the tip of the shear band penetrates the sample as shown in Fig. 1.2(c). The two parts of the sample separated by the shear band glide against each other in a synchronized manner as shown in Fig. 1.2(d), leading to fast continuous shear flow<sup>55</sup>

and significant heating<sup>56</sup> in the shear band. For macroscopic samples, the gliding speed is on the order of 4 mm/s under compressive loading<sup>54,55,57</sup>. The gliding speed under tension has not been directly quantified in experiment because catastrophic fracture happens immediately when the shear band penetrates the sample. The gliding speed is expected to increase with increasing yield stress or decreasing sample size<sup>58</sup>. When the sample size is within several hundred nanometers, the yield stress can be significantly higher, more than double that of the macroscopic sample<sup>13,26</sup>. The much higher yield stress of the nanoscale sample can significantly increase the gliding speed. Considering that the shear band thickness is around 10 nm,<sup>37-39</sup> the shear strain rate in the running shear band can be  $10^4$  /s in macroscopic samples and even higher in the nanoscale samples.

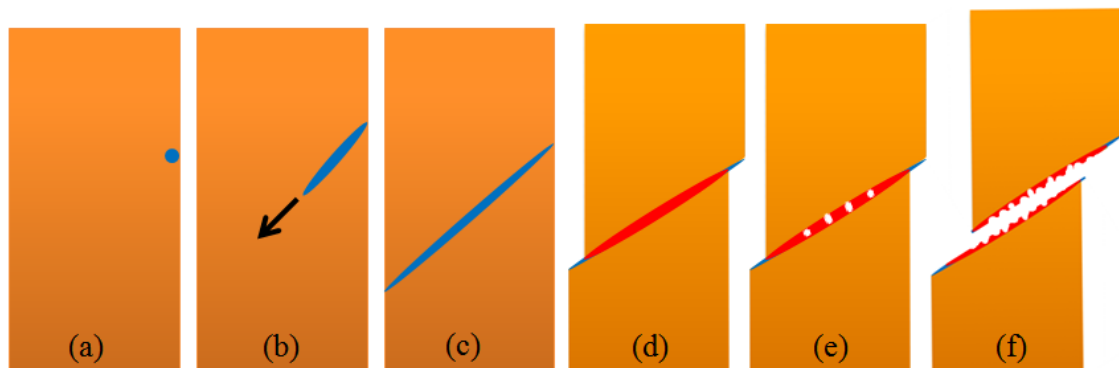


**Figure 1.2. Illustration of the successive stages of shear banding and the resulted tensile fracture. (a) Nucleation of shear band. The shear band is believed to preferentially nucleate on the surface as denoted by the blue dot. (b) Propagation stage of shear band, which ends when the shear band penetrates the whole sample as in (c). The blue regions denote the propagating cold shear band. The arrow indicates the propagating direction. (d) The synchronized gliding of the two parts of the sample separated by the shear band. The temperature rises in the shear band<sup>56</sup>, which is illustrated by the red region. (e) The speculated cavitation process in the running shear band under tension. (f) The resulted tensile fracture with the corrugated fracture surfaces.**

The shear band nucleation and propagation stages control the yield stress<sup>59,60</sup>, but it is in the synchronized gliding stage (Fig. 1.2d) when tensile fracture takes place. This is because synchronized gliding makes all the elastic energy stored in the sample available

to the shear band, while during nucleation and propagation only the local elastic energy is accessible to the shear band. When fracture happens in the stage shown in Fig. 1.2(d), the stored elastic energy will be released in a much more violent way than that conveyed by the gliding before fracture at the speed of 4 mm/s. With a high resolution ( $\sim 20 \mu\text{s}$ ) camera, the lower bound of the gliding speed during the onset of fracture under compression is estimated to be 170 m/s.<sup>54</sup> Tensile fracture should occur in a more violent way and it has not been quantitatively captured in experiments. It is speculated that during the gliding of the shear band under tension, cavities will nucleate in the shear band as illustrated in Fig. 1.2 (e). Such speculation is supported by the corrugated features in the fracture surfaces of MGs under tension<sup>61,62</sup> as illustrated in Fig. 1.2(f).

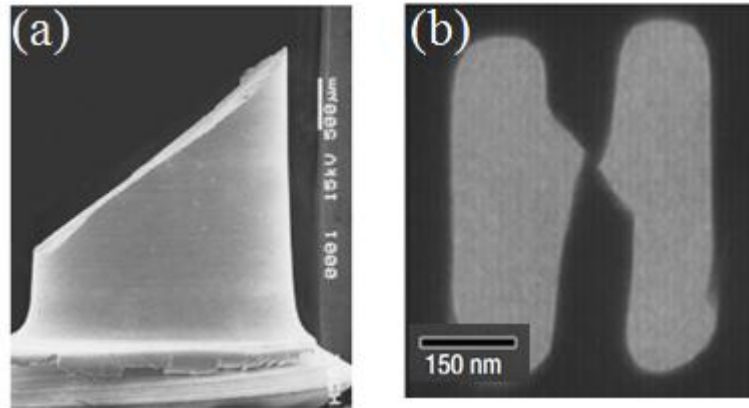


**Figure 1.3. (a) Typical tensile fracture seen in macroscopic metallic glasses<sup>63</sup>. Bright field is the sample. (b) Ductile deformation up to 45% strain via non-catastrophic shear banding under tension for a nanometer scale sample.<sup>25</sup> Dark field is the sample and the frame.**

### 1.3.2 Failure of nano-scale samples

It is known that the tensile fracture of MG materials is size-dependent. Brittle tensile fracture is the typical behavior of macroscopic metallic glass samples (Fig. 1.1a and Fig. 1.3a). Extensive tensile ductility via stable shear banding has been observed in  $\sim 300$  nm MG samples under tension tests<sup>25</sup> (Fig. 1.3b). Recently, Jang and Greer also reported that short MG samples exhibit tensile ductility while long MG samples do not<sup>26</sup>. In terms of Fig. 1.2, these observations suggest that smaller sized metallic glasses can avoid the

failure stages illustrated in Fig. 1.2(e) and (f). Brittle behavior emerges only when the sample size becomes large, which is in contrast with the intrinsically brittle behavior as illustrated in Fig. 1.4(a). The intrinsically brittle materials (such as silica glasses) remain brittle when the size is reduced to the nanoscale and the fracture surfaces are usually perpendicular to the loading direction.

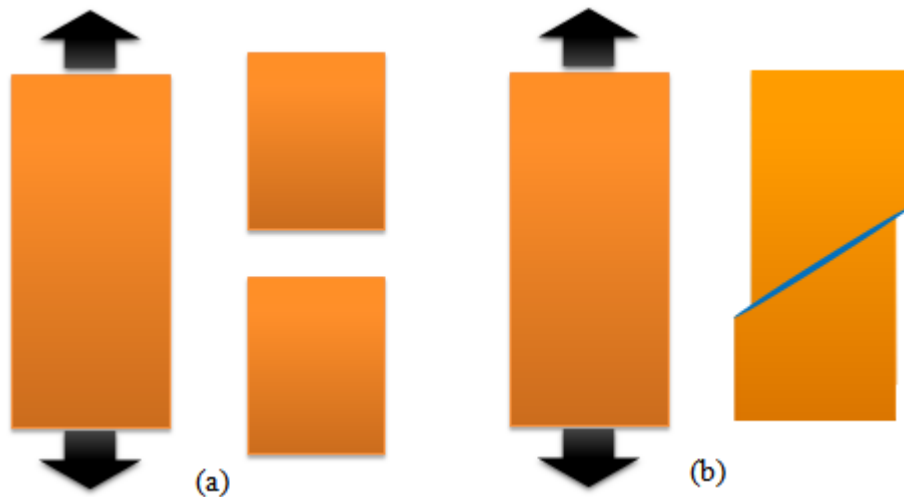


**Figure 1.4. (a) Intrinsically brittle behavior and (b) intrinsically ductile behavior.**

### 1.3.3 Failure modes and Poisson's ratio

The intrinsic ductility of metallic glasses or glasses in general is correlated with Poisson's ratio<sup>64,65</sup>. The glasses with a high Poisson's ratio have a high fracture energy. Such a correlation between far-from-equilibrium fracture and near-equilibrium elasticity is unexpected, yet highly useful to infer hard-to-measure fracture energy ( $G$ ) from an easy-to-obtain elastic constant ( $\nu$ ). The  $\nu$ - $G$  relation has already been successfully used as a guide to design tough metallic glasses.<sup>16,23,66,67</sup> When the correlation was first proposed for metallic glasses a decade ago, the critical Poisson's ratio for the sharp brittle-to-ductile (BTD) transition was found to be universally 0.31-0.32<sup>64</sup>. However, exceptions showed up as more studies were devoted to this topic. For example, it was

found that the Pd based metallic glass<sup>68</sup> is brittle, but its Poisson's ratio is as high as 0.4. The result suggests that although the Poisson's ratio to intrinsic ductility correlation is generally true, the critical Poisson's ratio might be alloy specific.

#### **1.3.4 Fatigue failure of metallic glasses**

The fatigue behavior of metallic glasses is not well understood and in some cases controversial. For example, the fatigue endurance limit of macroscopic metallic glass samples has been reported for the samples with the same composition to range from 4% to as high as 40% of the yield strength<sup>29-31</sup>. When the sample dimension is reduced to the micrometer scale, the fatigue limit increases to be even a little higher than the bulk yield strength<sup>69</sup>. Such controversy stems from the unclear understanding of fatigue fracture mechanisms in metallic glasses. Some studies have shown that no shear band was observed during fatigue tests and fatigue mechanism in BMG should be surface-defects based, which was different from the shear-band mechanisms during tensile testing<sup>70</sup>. Other experiments demonstrated that shear bands actually form on the surface at an angle to the applied load and will act as crack-initiation sites. The crack propagates from the outer surface of the specimen to the inside<sup>71</sup>. Furthermore, it was observed that crack growth or fracture under cyclic compression can be different than under cyclic tension. In cyclic compression the fracture occurred in a pure shear mode similar to monotonic compressive fracture behavior<sup>72,73</sup>. In cyclic tension the crack growth was perpendicular to the load<sup>73,74</sup>. Crack under cyclic loading advances via a repetitive blunting and resharping process similar to that commonly observed in polycrystalline metals<sup>75,76</sup>. It was also suggested that a fracture transformation zone ahead of the crack tip controls the crack growth<sup>77</sup>. Moreover, the fatigue crack propagation mechanism was observed to be strongly affected by the environment<sup>78</sup>.

### **1.4 Existing theories on the failure modes of metallic glasses**

Several models have been proposed to understand the failure modes of MGs. A major school of thought is that fracture in MGs is caused by a critical temperature rise<sup>56,58,79-81</sup> or thermal runaway<sup>82,83</sup> in the shear band. Such claims seem to be supported

by the often melted fracture surfaces. However, the melted fracture surfaces are only the result of fracture, which might or might not be the cause of fracture. The shear band is of nanoscale<sup>39</sup>, evolves with a temporal scale of from nanoseconds to microseconds<sup>56</sup>, and often propagates deep beneath the surface. As a result, the temperature rise in shear bands can only be inferred indirectly in bending<sup>56</sup> or compression<sup>84</sup>, not yet in tension. Moreover, the temperature based mechanism cannot explain the large differences in tensile ductility and compressive ductility considering that the temperature rise in the shear band before fracture should be very similar under tension or compression.

Another existing model on the fracture of metallic glasses is based on the critical shear offset distance<sup>61,62,85</sup>. It is argued that when the shear band gliding distance exceeds 16 microns, fracture would occur. While a large shear offset releases more elastic energy and therefore promotes fracture, the underlying mechanism cannot be the shear offset itself. Moreover, the value of the critical shear offset might not be universally 16 microns since in samples of smaller dimensions (for example, several microns) under tension, brittle fracture still occurs<sup>26</sup>. The critical shear offset should be strongly dependent on the loading conditions and sample geometry.

The third fracture model proposes the concept of the critical shear band energy density<sup>26,59</sup>. It is based on the asymmetry between the 3 dimensional elastic energy source (which is the whole sample) and a 2 dimensional energy sink (which is the shear band). If certain amount of elastic energy in the whole sample is concentrated in the shear band, the shear band energy density will increase and lead to catastrophic failure. Although the model can fit a wide range of experimental data<sup>59</sup>, the underlying atomic fracture mechanism inside the shear band remains unclear.

Since the failure modes of metallic glasses are clearly correlated with the Poisson's ratio<sup>64,65</sup>, efforts were devoted to understanding the Poisson's ratio and ductility relationship in metallic glasses. The existing theoretical work qualitatively explained the  $\nu$ -ductility relation by correlating the material resistance to dilatation (i.e., surface/void formation) with the bulk modulus (K), and the material resistance to shear deformation with the shear modulus ( $\mu$ ). Thus, materials with low  $\mu/K$  ratio (equivalently, high  $\nu$ ) prefer to shear flow rather than brittle fracture<sup>86,87</sup>. Continuum-treatment based on Anand-Su<sup>88</sup> model predicts that the fracture toughness does increase with  $\nu$ , cannot

predict a sharp BTD transition.<sup>89</sup> Further studies have related the fracture behavior of glasses to dilatation-induced softening<sup>89</sup>, activation barriers for plasticity and fracture<sup>90</sup>, or local stress fluctuations<sup>91</sup>. For example, Poon, Zhu, and Shiflet reasoned that the Poisson's ratio affects both the energy barriers for plastic deformation and brittle fracture at the yield point.<sup>90</sup> Interestingly, they argued that the critical Poisson's ratio for the BTD transition is system dependent, which was echoed by other reports.<sup>66,67,92</sup> However, the Poisson's ratio was introduced only through an elastic Eshelby factor which weakly depends on  $\nu$  (the Eshelby factor varies from 2.0 to 1.8 for  $\nu=0.2$  to 0.4). Knuyt developed a simple model relating elastic constants to a two-body potential, the position and dispersion of the first neighbor shell.<sup>93,94</sup> Using Knuyt's formula, Jiang and Dai found that the experimental atomic dispersion correlates well with Poisson's ratio.<sup>95</sup> Local stress fluctuations have also been linked to the brittleness of metallic glasses by a comparative study of two types of MG samples.<sup>91</sup> It is not yet clear whether the stress fluctuation is the cause or a result of the brittle fracture, and how general this correlation is among other amorphous systems.

Generally, we still understand little about the elasticity, plasticity and fracture in metallic glasses, or amorphous solids. Due to lack of long range order, there are no dislocations in metallic glasses. Well developed plasticity theory based on dislocation therefore is not relevant to plasticity in metallic glasses. The two widely used theories on plasticity of metallic glasses are free volume theory<sup>96</sup> and shear transformation zone theory<sup>41,97</sup>. However, continuum theory of inhomogeneous shear flow, fracture and fatigue process is still beyond reach<sup>10</sup> because the underlying atomic mechanisms are still unclear. Therefore we choose to employ atomic simulations to reveal the underlying atomistic mechanisms of the shear flow, fracture and fatigue failure in metallic glasses, which can serve as the foundation for further development of continuum level theory. In the following section, we outline the specific challenges and our approaches to solving them.

## 1.5 Existing simulation work on the failure mode of metallic glasses

To reveal the atomic mechanisms of failure and fracture, a sizeable simulation box, larger than the feature length scales of interest is needed. For example, to study the characteristics of a shear band, the minimum sample size should be larger than the thickness of a shear band, which is typically around 10 nm. This is extremely computational challenging for first-principles calculations since at most a few thousand atoms can be handled in first-principles calculations. This spatial limitation is one of the major reasons that first-principles simulations are rarely utilized to tackle the failure mode of metallic glasses. Even for short range order characterization and cohesive energy, first-principles calculations are practically difficult to use due to the lack of periodicity in metallic glasses.<sup>98</sup> As a result, first principles calculations are currently limited to electronic structure<sup>99</sup> and force field calibrations<sup>100,101</sup> for a small group of atoms.

MD simulation efforts are much more active<sup>98,102,103</sup> since the number of atoms that can be treated in MD simulations is much larger than that in first-principles calculations, increasing from  $10^3$ - $10^4$  in the 1980's, to  $10^6$ - $10^9$  in large scale simulations nowadays<sup>91,104</sup>. In early pioneering MD simulations<sup>48,105-107</sup>, the initial plasticity carried by shear transformation zones (STZ) was observed. However, the structural identification of STZ has not emerged until recently, enabled by order parameters such as the local shear modulus<sup>108</sup>, local Debye-Waller factor<sup>109</sup>, local low frequency normal modes<sup>110,111</sup>, and local atomic symmetry<sup>101,112-114</sup>. Thermal activation of the initial plasticity has also been clarified using MD simulations<sup>46,115</sup>. With increasing sizes in the simulations, the cascade or collaborative behavior of the individual initial plastic activities can be observed and strain localization into shear bands has been intensively studied<sup>51-53,101,116-120</sup>. The gist of these simulations is that plasticity in close packed glasses tends to initiate in the region with unfavorable local packing such as non-icosahedral clusters. The shear banding process will further amorphorize the stable clusters and form an across-the sample shear band. The temperature rise is not significant during the shear band nucleation and propagation.

MD simulations on the failure and fracture of metallic glasses require larger sample size than that needed for initial plasticity and strain localization, since the characteristic length scales (the plastic zone size for crack propagation<sup>91</sup> and critical length scale for shear band cavitation<sup>104</sup>) can easily approach micron scale. Existing pioneering MD simulations have demonstrated the importance of interaction range in the force field<sup>120</sup>, stress fluctuation<sup>91</sup>, and sample size<sup>60,79</sup> in controlling the failure of metallic glasses. Efforts have also been devoted to meso-scale simulations to overcome the spatiotemporal limitations in MD simulations<sup>44,83,121–123</sup>. The strain localization, damage evolution and extreme statistics observed in these meso-scale simulations are encouraging and helpful in understanding the failure of metallic glasses. However, the underlying atomic mechanisms cannot be revealed in meso-scale simulations because they inherently lack atomic detail. Direct observation of tensile fracture of intrinsically ductile metallic glasses in MD simulation is still lacking.

## 1.6 Challenges and approaches

To improve the ductility of metallic glasses, one of the most profound problems is the selection of glass-forming system, i.e., which elements to use and how much. The correlation between Poisson's ratio and intrinsic ductility provides a useful perspective to the design of tougher metallic glasses. Despite the above efforts, a clear understanding of the Poisson's ratio and intrinsic ductility relation from the perspective of bonding has yet to emerge. Atomic simulation should be a powerful way to help tackle this problem. But in most of the existing two body or many body force fields, the Poisson's ratio is generally too high compared to experimental results<sup>91,124–126</sup>, and the observed ductility in simulation is also too high<sup>101,116</sup>, making direct study of the  $\nu$ -ductility relationship very difficult. To reveal the bonding characteristics underlying the correlation between Poisson's ratio and ductility, we developed a new force-field tuning scheme that is applicable to both pair interaction and three-body interaction with angular constraint. The force field tuning scheme is shown to correct the overestimated Poisson's ratio and ductility of the model amorphous solids and reveals that higher covalency in the bonding

will decrease both the Poisson's ratio and ductility in metallic glasses and general amorphous solids.

Another challenge is to understand *quantitatively* why metallic glasses can be very tough and ductile in bending and compression but brittle in tension and why the tensile ductility depends on sample size. Current experiment spatial and temporal resolutions (10  $\mu\text{m}$  and 10  $\mu\text{s}$ , respectively) are not high enough to resolve the evolution in the shear band<sup>127</sup>. To resolve the puzzle regarding the size dependent tensile fracture, we designed a novel large scale atomic simulation method and a novel multi-scale simulation method. These methods overcome spatial and temporal limitations in atomic simulations by orders of magnitude and can offer realistic atomic details on the tensile fracture occurred in the shear band. It is found that the shear band to crack transition via cavitation in metallic glasses is triggered by the critical thermomechanical states in the running shear band. Notably, the materials' resistance to cavitation can be significantly reduced by the presence of fast shear flow, which explains why metallic glasses are so ready to fracture along a running shear band. Based on the simulations, we proposed a cavitation map to systematically understand the size dependency of shear band cavitation. An analytical material index is also derived to predict the tensile ductility of metallic glasses. In combination with the force tuning method, we found that the propensity of shear band cavitation is increased when the covalency in the bonding is increased.

The third major challenge is to improve the understanding of the fatigue failure of metallic glasses. Atomic simulations are a powerful way to unveil the microscopic damage accumulation mechanism in metallic glasses<sup>101,116</sup>. Yet no atomic simulation result on cyclic loading induced fracture has appeared in this field<sup>128,129</sup>. Therefore systematic atomistic simulation on the fatigue damage initiation, accumulation and final fracture is warranted and valuable. The foremost obstacle arises from the deficiency of the available atomic force fields<sup>130</sup>, which usually lead to model metallic glasses that are significantly more ductile than experimental metallic glass systems. For instance, the amorphous nanowire modeled by the widely used Lennard-Jones force field<sup>124</sup> exhibits little damage, let alone fracture, even after extensive push-pull cyclic loading with a strain amplitude as high as 36% in our preliminary result. To this end, we combined the force tuning method and the precise plastic strain controlled fatigue tests that are

difficult to conduct in experiments in order to quantitatively study the low cycle fatigue behavior of metallic glasses nanowires. The simulations revealed quantitative insight on how the atomic damage is accumulated in metallic glass nanowires under low cycle fatigue tests.

## **1.7 Outline of the thesis**

In this thesis, we first introduce the simulation method and force tuning methods in Chapter 2. In Chapter 3, we applied the force tuning methods to three different amorphous systems and uncovered a universal link between Poisson's ratio, fracture behavior and the covalency or angular constraint in the bonding. In Chapter 4, we discuss the history-independent properties of a running shear band and suggest that the key controlling parameters for tensile fracture in the shear band are the thermomechanical states rather than the widely used free volume, which serves as the foundation of the tensile fracture analysis in the following chapters. In Chapter 5, we designed large scale simulations that overcome three orders of magnitude in spatiotemporal scale to capture the tensile fracture in micron-scale metallic glass samples. The large scale simulations demonstrate that tensile fracture of metallic glasses is caused by shear band cavitation, which is activated by shear flow. The shear flow activated cavitation mechanism explains why metallic glasses can be tough but brittle. In Chapter 6, we further designed a multi-scale simulation method to simulate macroscopic samples under uniaxial tension. We summarized all the principles on cavitation in the cavitation map, which clarifies how to evaluate whether a given force field can display size dependent tensile fracture via shear band cavitation. The multi-scale simulation result demonstrates that the covalency will determine the propensity of shear band cavitation under tension. In Chapter 7, we present precise plastic strain controlled fatigue tests that are difficult to realize in experiments in order to quantitatively study the low cycle fatigue behavior of metallic glass nanowires. The simulations offered quantitative insight into the atomic damage accumulation controlled failure mechanism in metallic glass nanowires. In the mean time, we also find that increasing covalency will decrease

the fatigue resistance of metallic glass nanowires. Conclusions and future research directions are presented in Chapter 8.

## 2. Simulation Methods

### 2.1 Molecular dynamics simulations

Molecular dynamics (MD) is a computational simulation of the physical movement of particles (atoms, molecules, or pseudo-atoms representing groups of atoms) based on classical Newton dynamics<sup>131,132</sup>. The engine of molecular dynamics is the force field or inter-atomic potential, which defines the forces or potential energy between the particles as a function of the relative positions of the particles. At each configuration, the net force on a given atom can be calculated as the vector sum of the forces exerted by all the other particles that are within the interaction range. From the net force and the mass of a given atom, the acceleration of the given atom can be calculated. Given a time step, the velocity and the new position of the atom can be obtained. In this way, the trajectory of the system advances in time step by step. To resolve the motion of the atoms, the time step used in MD simulations should be smaller than the fastest vibrational frequency in the system, and is typically around 1 femto-second. Therefore, the time scale of MD simulations, increasing with the ever increasing computing power, is usually limited to the nanosecond or microsecond scale, although the longest MD simulation conducted in a specialized supercomputer has reached one millisecond<sup>133</sup>. The number of particles calculated in an MD simulation ranges from several hundred to several billion<sup>134</sup>. Correspondingly, the length scale in MD simulation is usually between the nanoscale and the sub-micron scale.

#### 2.1.1 Force fields

Force fields, or inter-atomic potentials are usually generated by fitting to the experimental data and/or First-principle calculations. Force fields can be categorized as pair potentials<sup>124</sup>, three-body potentials<sup>125</sup> and many-body potentials<sup>135</sup>. In a pair

---

Portions of this chapter previously appeared as: Shi, Y., Luo, J., Yuan, F. & Huang, L. Intrinsic ductility of glassy solids. *J. Appl. Phys.* **115**, 043528 (2014).

potential, the force between two atoms only depends on the distance between them. In a three-body potential, the bond angles between three atoms also affect the potential energy and the forces. Generally, in a many-body force field, the effect of the local environment is taken into consideration when evaluating the forces between atoms.

In this dissertation, we employed a wide selection of force fields that include pair potentials, three-body potentials and many-body potentials. The force fields used in this study include pair wise interaction as in the binary Lennard-Jones (LJ) potential parameterized by Kob Anderson (KA)<sup>136</sup>, Wahnstrom (WA)<sup>124</sup> and its modified version (mWA) based on angular constrain<sup>130</sup>, many body potential as in the widely used EAM potentials that describes CuZr<sup>137</sup> (developed by M. Mendeleev et al) and CuZr<sup>100</sup> (developed by H. Sheng termed) and FeP<sup>138</sup> and three body interaction (angular constraint) as in the Stillinger-Weber (SW) amorphous Si system<sup>139</sup>. Since we are interested in the simplest and most general physics underlying the atomic failure mechanisms, we mostly used the Wahnstrom LJ pair potential and the SW Si potential. The simple analytical form of these two potentials makes it possible for us to establish a clear connection between the failure mechanisms and the bonding characteristics via tuning the potential parameters. More details on the force field tuning methods will be discussed in Section 2.2. The more sophisticated many-body force fields were used in some cases to check the generality of the trends obtained in these simple force fields.

### 2.1.2 Ensembles

In a typical MD simulation that contains a fixed number of atoms in a fixed volume, the energy of the system will also conserve, which is dictated by Newton's law. The trajectory of such a system samples the configuration space of a microcanonical ensemble (NVE). During the simulation, we can also choose to keep the system temperature constant and let the system evolve in a canonical ensemble (NVT). One simple way to control system temperature is to rescale the current velocities of all the atoms by a calculated factor. However, the resulted velocity distribution would not follow that of an NVT ensemble. More sophisticated temperature control method has been developed to reproduce canonical ensemble statistics<sup>140,141</sup>, which is widely used in

MD simulations. Stresses can also be controlled independently during an MD simulation so that the volume/shape of the simulation box becomes a variable<sup>142</sup>, which is very useful and widely used in mechanical tests in MD simulations.

### **2.1.3 Boundary conditions**

In MD simulations, the commonly used simulation geometry is an orthogonal box, which is termed the simulation box. The boundary conditions for the simulation box usually follow periodic boundary conditions. For example, the atoms near the upper boundary of the simulation box will interact with those near the lower boundary of the simulation box. Therefore, no surface exists if the periodic boundary condition is applied to all three directions of the simulation box. Periodic boundary conditions are useful to overcome the length scale limitation and to simulate the bulk properties in MD simulations. If surfaces are desired in the simulation, periodic boundary condition can be canceled in selected or all directions. The surfaces will effectively face vacuum spaces. The free surfaces can be in any form. For example, a sample with a cylindrical surface can be used to model a nanowire.

### **2.1.4 Mechanical tests in MD simulations**

Almost all types of mechanical tests that can be done in experiments can be conducted in MD simulations via controlling the boundary conditions or the shape of the simulation box. For example, to conduct a uniaxial compression (tension) test under periodic boundary conditions, we can displace the upper boundary of sample toward (away from) the lower boundary while maintaining zero stresses in the other two directions. If we want to study the crack propagation behavior, a notch or a crack can be introduced before the test by removing the corresponding atoms that are in the notch region. Alternatively, mechanical tests that required more complicated boundary conditions can be done without the limitation of periodic boundary conditions. For example, to simulate the synchronized gliding via shear banding, no periodic boundary condition should be applied in the loading direction. To apply deformation without the periodic boundary condition, we can fix the atoms near the two boundaries in the loading

direction as “grips” and displace the grips accordingly. Optionally, the grips can still have the freedom to move in the directions other than the loading direction to mimic an ideal displacement controlled uniaxial test. Moreover, we can also use imaginary “walls” to apply loading to the sample. A wall is a defined mathematical plane, which exerts extra forces on nearby atoms.

One common feature and most of the time a limitation of the mechanical tests conducted in MD simulations is that the deformation rate is typically 10 orders of magnitude higher than the experimental deformation rate. This is determined by the short time span accessible for MD simulations. The ultrafast strain rate should always be considered when interpreting mechanical tests in MD simulations. Another limitation for mechanical tests in MD simulations is the length scale, which is limited to submicron scale. Therefore if a mechanical test requires large sample size (for example, to measure the fracture toughness of a tough material), it would be very challenging and even impossible for MD simulations with current computing resources. In this dissertation, we will present specialized simulation methods to overcome the spatiotemporal limitations in MD simulations. One such method is called perturbative static loading (detailed in Chapter 5), which can simulate micron scale samples under an ideal displacement controlled tensile test with zero strain rate. Another example is the concurrent multiscale method (detailed in Chapter 6) that combines the MD simulation with continuum models to simulate uniaxial tension tests on samples with sizes to the macroscopic scale.

## **2.2 Force field tuning methods**

In this thesis, force tuning is used to study ductility of metallic glasses for two specific reasons. First, force field tuning in Molecular Dynamic (MD) simulation is a powerful method to reveal the connection between atomic bonding and materials properties. Therefore force field tuning will be very effective in identifying what bonding characteristic controls the ductility in metallic glasses. Second, in most of the existing two body or many body force fields, the Poisson's ratio is generally too high compared to experimental results<sup>91,124–126</sup>. According to the Poisson's ratio to fracture toughness or ductility correlation observed in experiment<sup>64</sup>, these existing force fields

will overestimate the ductility and therefore are not suited to study the link between the ductility and the Poisson's ratio of metallic glasses.

Here, we will employ three well-studied but very different molecular systems, namely the Wahnstrom binary Lennard Jones (BLJ) potential for metallic glasses<sup>124</sup>, Stillinger Weber (SW) potential for amorphous Si<sup>125</sup> and the Beest-Kramer-Santen (BKS) potential for silica<sup>143</sup>. The force tuning methods for the all the distinct systems share a common strategy, which is to tune the convalency (angular constraint) of the bonding via a single parameter in the force field. It should be noted that, even for a two-body interaction force field, angular constraint can imposed by tuning the interactions between the 2<sup>nd</sup> nearest neighbors.

### 2.2.1 Modified binary Lennard-Jones potential

For the model metallic glasses, we chose a binary Lennard-Jones (BLJ) glass-forming system parameterized by Wahnstrom.<sup>144</sup> The alloy consists of two equimolar species, which will be referred to as  $S$  and  $L$  for small and large atoms, interacting via a Lennard-Jones potential of the form:

$$\phi_L(r) = \begin{cases} 4\varepsilon_{\alpha\beta} \left( \frac{\sigma_{\alpha\beta}^{12}}{r^{12}} - \frac{\sigma_{\alpha\beta}^6}{r^6} \right) - \varepsilon_{cutoff}, & r < r_{\alpha\beta}^c \\ 0, & r \geq r_{\alpha\beta}^c \end{cases} \quad (2.1)$$

where  $\varepsilon_{\alpha\beta}$  and  $\sigma_{\alpha\beta}$  provide the energy and length scales, respectively. Here the cutoff values  $r_{\alpha\beta}^c$  were chosen to be species dependent, such that all pair interactions are precisely 0.0163  $\varepsilon_{LL}$  at the cutoffs of  $r_{LL}^c = 2.5\sigma_{LL}$ ,  $r_{LS}^c = 2.2917\sigma_{LL}$ ,  $r_{SS}^c = 2.0833\sigma_{LL}$ . The  $SS$  and  $LL$  bond energies are equal to that of the  $SL$  bond energy:  $\varepsilon_{SS} = \varepsilon_{SL} = \varepsilon_{LL}$ . The  $SS$  and  $LL$  length scales are related to the  $SL$  length scale by,

$$\sigma_{SS} = \frac{5}{6}\sigma_{LL}, \sigma_{SL} = \frac{11}{12}\sigma_{LL} \quad (2.2)$$

The two types of atoms have different masses:  $m_L = 2m_0$ ,  $m_s = m_0$ , where  $m_0$  is the mass unit. The reference time scale is  $t_0 = \sigma_{LL} \sqrt{m_0 / \varepsilon_{LL}}$ . The closest binary experimental

MG system is Ni<sub>50</sub>Nb<sub>50</sub> in terms of composition and atomic radius ratio.<sup>145,146</sup> All physical quantities will therefore be expressed in SI units following the conversion in a previous report:<sup>147</sup>  $\sigma_{LL} \approx 2.7 \text{ \AA}$ ;  $m_0 \approx 46 \text{ amu}$ ;  $\varepsilon_{LL} \approx 0.151 \text{ eV}$ ;  $t_0 \approx 0.5 \text{ ps}$ . A standard velocity Verlet integrator was used with a timestep of  $5 \text{ fs}$ . This BLJ system has been used as a model MG system subjected to uniaxial compression,<sup>116</sup> uniaxial tension,<sup>148</sup> and nanoindentation tests.<sup>147</sup>

One interesting monatomic glass-former is the Dzugutov system,<sup>149</sup> which is brittle at low temperatures with a low Poisson's ratio of about 0.3. The key feature of the Dzugutov potential is an energy bump that mimics the Friedel's oscillations.<sup>116,149–151</sup> Based on first-principle studies, the Friedal oscillation could be modeled by a bump or more in the tail of the 2-body potential in MD simulations<sup>152–154</sup>. Moreover, the effective pair interaction for liquid iron obtained from tight-binding calculations also features a “bump,” which is due to contributions from the *d*-electrons.<sup>155</sup> Inspired by the efforts mentioned above, we superimposed an energy bump, between  $r_{\alpha\beta}^s$  to  $r_{\alpha\beta}^c$  with a varying height of  $\varepsilon_B$ , to the original Wahnstrom system. The interaction in BLJ system is thus,

$$\phi_{BLJ}(r) = \begin{cases} \phi_{LJ}(r), & r < r_{\alpha\beta}^s \\ \phi_{LJ}(r) + \varepsilon_B \varepsilon_{LL} \cdot \sin^2 \left( \pi \frac{r_{\alpha\beta}^c - r}{r_{\alpha\beta}^c - r_{\alpha\beta}^s} \right), & r \geq r_{\alpha\beta}^s \\ 0, & r \geq r_{\alpha\beta}^c \end{cases} \quad (2.3)$$

where  $r_{\alpha\beta}^s$  is taken as  $1.5\sigma_{\alpha\beta}$ , which is outside the first neighbor shell. As shown in Fig. 2.1, this additional repulsive bump term is chosen such that it does not affect the original potential well, while maintaining the same energy and force at the cutoff. The highest energy bump,  $\varepsilon_B$ , is about 0.375, above which the system becomes unstable in the condensed state.

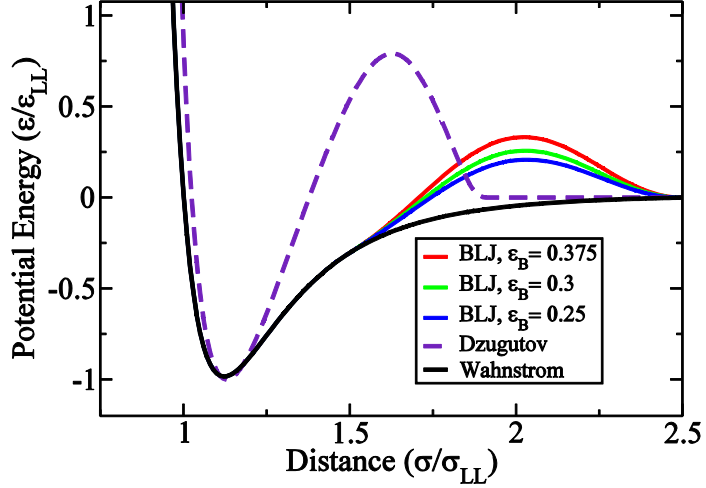


Figure 2.1. Comparison between the BLJ potential, the original Wahnstrom potential (essentially a shifted Lennard-Jones potential) and the Dzugutov potential. Both the distance and the potential energy are scaled to the proper internal length and energy units for each system.

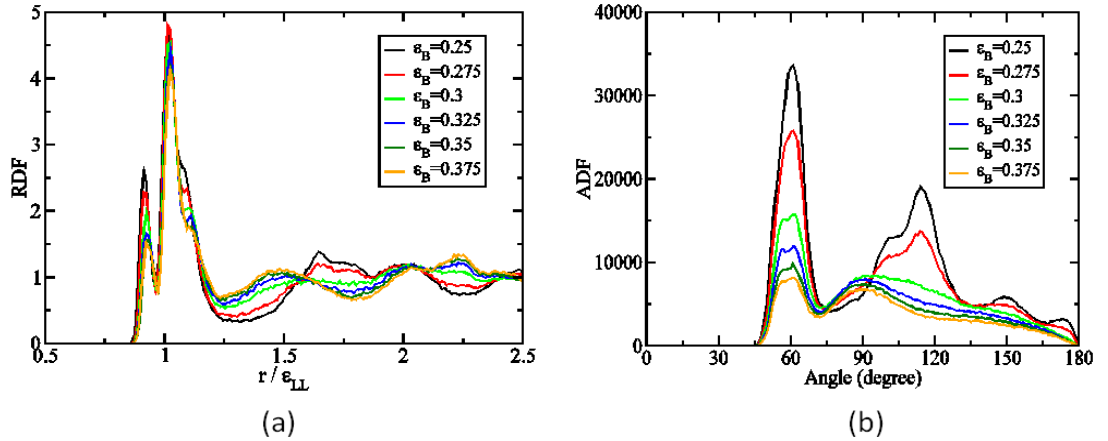
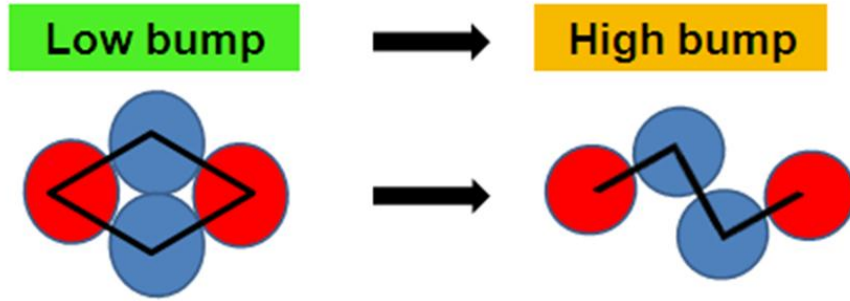


Figure 2.2. Species-blind RDF curves (a) and ADF curves (b) are shown for glasses of the BLJ systems with from 0.25 to 0.375.

In our BLJ potential system, as  $\epsilon_B$  increases, although the separation and strength of the bonding between an atom and its nearest neighbors stay the same, repulsion arises between atoms within the first-neighbor shell for large separations. As shown in Fig. 2.2, both the radial distribution function and the angular distribution function (ADF) vary significantly as a function of  $\epsilon_B$ . With  $\epsilon_B$  increased to 0.3, the second peak at distance

$1.7 \sigma_{LL}$  in  $g(r)$  splits into two sitting at  $1.4 \sigma_{LL}$  and  $2 \sigma_{LL}$  respectively. This is reasonable because the second nearest neighbor distance in the original LJ potential is close to the maximum of the newly added repulsive bump and therefore will not be stable if  $\varepsilon_B$  is sufficiently large. In Fig. 2.2(b), the ADF curves show that both the 60 and 120 degree peaks (corresponding to close-packed local structures) shrinks and a new 90 degree peak emerges when  $\varepsilon_B$  increases beyond 0.3, indicating an effective angular constraint in the structure or covalency in bonding arises due to the bump. Combining the change in both the RDF and the ADF, we find the structure change can be schematically represented by a simple adjustment at the short range as shown in Fig. 2.3.



**Figure 2.3. Schematic illustrations of the short range structure change in glasses of the BLJ systems with respect to the increasing bump height.**

### 2.2.2 Modified Stillinger-Weber potential

Despite the strong directional bonding makes Stillinger-Weber (SW) potential<sup>125</sup> simulated glasses very different from metallic glasses, far reaching similarities are found between the plasticity of SW potential simulated glass and metallic glasses<sup>117</sup>. To get more general insights, we also tuned the widely-used SW silicon force field. The original SW system has also been chosen as an example network glass to investigate generic features of plasticity in amorphous solids<sup>156</sup> with the form described as follows,

$$PE = \sum_{i < j} \varepsilon \phi_2(r_{ij}) + \sum_{i < j < k} \varepsilon \phi_3\left(\frac{\vec{r}_i}{\sigma}, \frac{\vec{r}_j}{\sigma}, \frac{\vec{r}_k}{\sigma}\right) \quad (2.4)$$

$$\phi_3\left(\frac{\vec{r}_i}{\sigma}, \frac{\vec{r}_j}{\sigma}, \frac{\vec{r}_k}{\sigma}\right) = h(r_{ij}, r_{ik}, \theta_{jik}) + h(r_{ji}, r_{jk}, \theta_{ijk}) + h(r_{ki}, r_{kj}, \theta_{ikj}) \quad (2.5)$$

$$h(r_{ij}, r_{ik}, \theta_{jik}) = \lambda \cdot e^{\frac{\gamma}{r_{ij} - a}} e^{\frac{\gamma}{r_{ik} - a}} \left(\cos \theta_{jik} + \frac{1}{3}\right)^2 \quad (2.6)$$

Here, the system potential energy is composed of two-body contributions and three-body contributions. The pair interaction  $\phi_2$  provides the bond length and bond strength, while the angular term  $\phi_3$  gives rise to covalent bonding. The complete formula and the parameters can be found in the original reference.<sup>156</sup>

Recently, Angell and co-workers introduced a force field tuning scheme, in which the prefactor,  $\lambda$ , of the angular term was systematically reduced, which leads to increased fragility of the liquid.<sup>157</sup> This potential tuning scheme was also used to show that  $\lambda$  affects the plastic behavior under shear.<sup>158</sup> We employed the same force field tuning scheme with a range of  $\lambda$  from 21 to 33 as opposed to 15 to 21.5 in the original paper.<sup>157</sup> The timestep for the SW system is 2.0 fs. SW glasses with higher  $\lambda$  will impose stronger angular constraint on the system. Thus, higher  $\lambda$  leads to higher covalency in amorphous silicon systems.

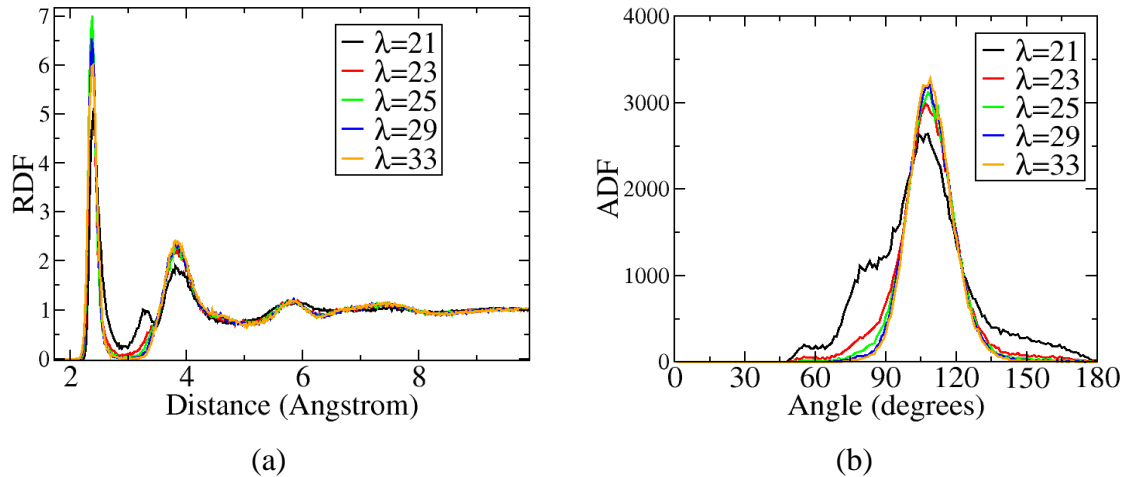


**Figure 2.4. RDF curves (a) and ADF curves (b) are shown for glasses of the Stillinger-Weber systems with the prefactor of the angular term ranging from 21 to 33.**

For the SW system, as can be seen from Fig. 2.4, the sample with  $\lambda = 21$  is structurally different from all other samples. There are extra peaks for the  $\lambda = 21$  sample in both the RDF curve and the ADF curve. This is due to over-coordination in the sample with the weakest bonding covalency. For samples with  $\lambda$  higher than 21, the RDF curves largely overlap. But with increasing  $\lambda$ , the angular distribution curves become slightly sharper, indicating enhanced angular constraints (covalency) of the bonding.

### 2.2.3 Modified BKS potential for silica system

For the silica system, the widely used Beest-Kramer-Santen (BKS) potential<sup>143</sup> was a two-body interaction following the formulation,

$$\phi_{ij}(r_{ij}) = \frac{q_i q_j}{r_{ij}} + A_{ij} e^{-b_{ij} r_{ij}} - \frac{c_{ij}}{r_{ij}^6} \quad (2.7)$$

The pair interaction consists of a Coulombic term, a short-range repulsion term, and a long-range Van der Waals attraction term. The latter two terms together form the Buckingham potential. The values of  $A_{ij}$ ,  $b_{ij}$  and  $c_{ij}$  for Si-O and O-O pairs (no direct Si-Si interactions) can be found in the original reference.<sup>143</sup>

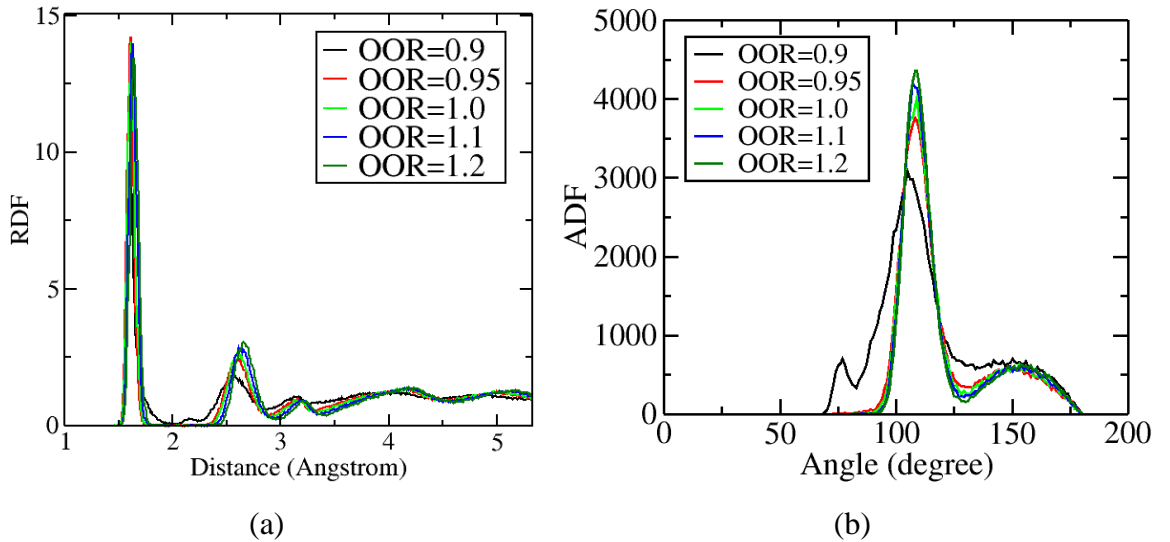


**Figure 2.5. RDF curves (a) and ADF curves (b) are shown for glasses of the BKS systems with the OOR parameter ranging from 0.9 to 1.2.**

Our rationale for force field tuning in the BKS system is as follows. In a  $\text{SiO}_4$  tetrahedron, the positively charged silicon atom is strongly attracted to four mutually repelling negatively charged oxygen atoms. The Si-O interaction favors high coordination for Si, while the O-O repulsion (*OO*R) favors low coordination for Si (enforcing covalency). Here, the parameter  $A_{ij}$  for O-O pairs was varied by scaling, such that  $A_{ij} = \text{OO}R \cdot A_{ij}^0$  ( $A_{ij}^0$  is the original parameter). The range of *OO*R is from 0.9 to 1.2 (*OO*R=1.0 corresponds to the original BKS parameterization).

For the BKS system (Fig. 2.5), the sample with *OO*R=0.9 is structurally different from the other systems. This is also due to over-coordination of the silicon, which is analogous to the  $\lambda = 21$  sample in the SW system. As *OO*R increases, the O-O distance increases and the angular distribution becomes sharper.

### 3. Intrinsic Ductility of Glassy Solids

In this chapter, we applied systematic mechanical tests to the glassy samples generated by the force tuning method discussed in the preceding chapter. A very similar correlation between the angular constraint in bonding and the mechanical behaviors (Poisson's ratio and ductility) emerges in these three very different systems (the BLJ system, the SW system and the BKS system): higher angular constraint leads to lower Poisson's ratio and lower ductility. Analytical models were derived to help rationalize the observed trend.

#### 3.1 Introduction

Recently, an intriguing empirical relation was observed in metallic glasses and oxide glasses: the fracture energy ( $G$ ) increases with the Poisson's ratio ( $\nu$ ), with a sharp brittle-to-ductile (BTD) transition at a critical  $\nu_{BTD}=0.31-0.32$ .<sup>86</sup> A similar Poisson's ratio vs ductility correlation was also reported previously in crystalline metals.<sup>159</sup> Such a correlation between far-from-equilibrium fracture and near-equilibrium elasticity is unexpected, yet highly useful to infer hard-to-measure fracture energy ( $G$ ) from an easy-to-obtain elastic constant ( $\nu$ ). The  $\nu$ - $G$  relation has already been successfully used as a guide to design tough metallic glasses.<sup>16,23,66,67</sup>

To comprehend the  $\nu$ - $G$  relation, one can start by linking the material resistance to dilatation (i.e., surface/void formation) to the bulk modulus ( $K$ ) and the material resistance to shear deformation to the shear modulus ( $\mu$ ). Thus, materials with low  $\mu/K$  ratio (equivalently, high  $\nu$ ) prefer to shear flow rather than brittle fracture.<sup>20,86,87</sup> Continuum-treatment based on the Anand-Su<sup>88</sup> model predicts that the fracture toughness does increase with  $\nu$ , yet absent a sharp BTD transition.<sup>89</sup> Recently, Poon, Zhu, and Shiflet reasoned that the Poisson's ratio affects both the energy barriers for plastic deformation and brittle fracture at the yield point.<sup>90</sup> Interestingly, they argued the

---

Portions of this chapter previously appeared as: Shi, Y., Luo, J., Yuan, F. & Huang, L. Intrinsic ductility of glassy solids. *J. Appl. Phys.* **115**, 043528 (2014).

critical Poisson's ratio for BTD transition is system dependent, which was echoed by other reports.<sup>66,67,92</sup> However, the Poisson's ratio was introduced only through an elastic Eshelby factor which weakly depends on  $\nu$  (the Eshelby factor varies from 2.0 to 1.8 for  $\nu=0.2$  to 0.4). Knuyt developed a simple model relating elastic constants to a two-body potential, the position and dispersion of the first neighbor shell.<sup>93,94</sup> Using Knuyt's formula, Jiang and Dai found that the experimental atomic dispersion correlates well with Poisson's ratio.<sup>95</sup> Local stress fluctuations have also been linked to the brittleness of metallic glasses by a comparative study of two types of MG samples.<sup>91</sup> It is not yet clear whether the stress fluctuation is the cause or a result of the brittle fracture, and how general this correlation is among other amorphous systems. Despite the above efforts, a mechanistic understanding of the  $\nu$ - $G$  relation has yet to emerge.

A systematic investigation of the  $\nu$ - $G$  relation requires means to control the Poisson's ratio, which is challenging experimentally: processing conditions such as cooling rate,<sup>66,67</sup> applied pressure,<sup>160</sup> or post-annealing<sup>86</sup> can only affect  $\nu$  moderately. On the other hand, although  $\nu$  is more sensitive to chemistry, the available elements are discrete, and the effects of alloying in metallic glasses or mixing of glass formers and modifiers in oxide glasses are still poorly understood. To this end, molecular simulations (MD) can generate model glasses with prescribed bonding, in addition to full control over the thermomechanical history of glasses.<sup>157,158,161</sup> To reveal why  $\nu$  correlates to the intrinsic ductility of glasses, herein we employed MD simulations to investigate glasses with tunable Poisson's ratio by varying the force-fields, as well as the processing and testing conditions.

## **3.2 Simulation methodology**

### **3.2.1 Interatomic force fields and potential tuning**

Three families of model glasses were investigated in order to delineate commonality: the binary Lennard-Jones (BLJ) potential parameterized by Wahnstrom<sup>144</sup>, the Stillinger-Webber (SW) potential<sup>125</sup> and the Beest-Kramer-Santen (BKS) potential<sup>143</sup> to model the amorphous metals (termed BLJ system), the amorphous silicon (SW system) and the

silica glass (BKS system), respectively. The force field formulations and potential tuning schemes are detailed in the preceding Chapter.

All three force field tuning schemes aim to tune the Poisson's ratio of the glassy solids by adjusting the covalency (angular constraint) using one single parameter, while preserving the force-field formulation, in order to obtain a series of glasses within the same family of glasses. The bonding covalency referred to is simply the angular constraints arising from the force fields. It should be noted that, even two-body force fields can impose angular constraints by tuning the interactions between the 2<sup>nd</sup> nearest neighbors.

### 3.2.2 Sample preparation

For all three amorphous systems, four types of amorphous samples were prepared: bulk samples (for uniaxial tension tests); nanowire samples (for uniaxial tension tests); slab samples (for pure shear tests); pre-cracked slab samples (for compact tension tests). Temperature control and stress control during the MD simulations follow the standard Nose-Hoover formulation.<sup>162,163</sup> The parameters of sample geometries and sample preparations are listed in Table 3.1. The glassy samples were prepared by quenching a well-equilibrated liquid at  $T_{\text{start}}$  to  $T_{\text{end}}$  isochorically for a total cooling time of  $t_{\text{cool}}$ . The final temperature is set roughly at about 10% of the glass transition temperature  $T_g$ .  $T_g$  is estimated as the temperature with the peak of the specific heat at constant volume during cooling, at which the system loses a considerable number of degrees of freedom. The initial density was chosen such that the residual stress due to cooling at  $T_{\text{end}}$  is almost zero. Note that, for the bulk samples and the slab samples, the periodic boundary conditions (PBCs) were applied in three-dimensions during the cooling process. For the nanowire samples, a “simulated casting” technique<sup>148,164,165</sup> was employed to ensure proper surface relaxation during cooling, in which the PBC was applied only in the nanowire axis direction. The pre-cracked slab samples were obtained from periodic duplication of the corresponding slab samples ( $4 \times 4 \times 1$ ,  $6 \times 6 \times 1$ , and  $3 \times 3 \times 1$ , for the BLJ, SW, and BKS systems, respectively). Pre-existing cracks were created by removing atoms within a diamond-shaped region at the center of the X-Y plane through the entire

slab thickness (the thickness direction is the Z direction for the slab). The short-diagonals of the diamonds along the Y-direction are 2.7, 3.0, and 2.0 nm, while the long-diagonals (crack size) along the X-direction are 16.2, 18.0, and 12.0 nm, for BLJ, SW, and BKS systems, respectively. The half crack size over the lateral size of the system is about 1/8 for all samples. It should be noted that the periodicity due to system-replication will not emerge, since the stress field due to the pre-existing crack is inhomogeneous. A similar technique has also been used in simulating nanoindentation, which also features an inhomogeneous stress field.<sup>147,166</sup>

**Table 3.1. Sample dimension and preparation. The number in the bracket is the number of atoms in each sample. The amorphous nanowires are characterized by the radius  $r$  and the length  $L$ . The slab samples are for pure shear tests. The pre-cracked samples for compact tension tests are obtained from periodic duplication of these slab samples ( $4 \times 4 \times 1$  for the BLJ,  $6 \times 6 \times 1$  for SW systems and  $3 \times 3 \times 1$  for SW systems).**

Amorphous system	$T_{\text{start}}$ (K)	$T_{\text{end}}$ (K)	$T_g$ (K)	$t_{\text{cool}}$ (ps)	Bulk Sample (nm <sup>3</sup> )	Nanowire Sample $r/L$ (nm)	Slab (nm <sup>3</sup> )	Density (g/cm <sup>3</sup> )
BLJ $\varepsilon_B = 0.25$	2105	39	390	2500	5.1×5.1×15.4 (24000)	5.1/20.6 (100668)	15.4×15.4×2.6 (36000)	6.8
BLJ $\varepsilon_B = 0.275$	2105	28	310	2500	5.2×5.2×15.6 (24000)	5.2/20.9 (100596)	15.6×15.6×2.6 (36000)	6.5
BLJ $\varepsilon_B = 0.3$	2105	28	290	2500	5.3×5.3×16.0 (24000)	5.3/21.4 (100616)	16.0×16.0×2.6 (36000)	6.0
BLJ $\varepsilon_B = 0.325$	2105	28	290	2500	5.4×5.4×16.3 (24000)	5.4/21.7 (100604)	16.3×16.3×2.7 (36000)	5.7
BLJ $\varepsilon_B = 0.35$	2105	28	280	2500	5.5×5.5×16.5 (24000)	5.5/22.0 (100568)	16.5×16.5×2.7 (36000)	5.5
BLJ $\varepsilon_B = 0.375$	2105	28	300	2500	5.6×5.6×16.8 (24000)	5.6/22.4 (100624)	16.8×16.8×2.8 (36000)	5.2
SW $\lambda = 21$	5000	120	1200	1000	4.3×4.3×12.8 (12288)	4.3/17.1 (51404)	12.1×12.1×2.1 (16384)	2.4
SW $\lambda = 23$	5000	160	1600	1000	4.4×4.4×13.0 (12288)	4.3/17.1 (51380)	12.3×12.3×2.2 (16384)	2.3
SW $\lambda = 25$	5000	200	2000	1000	4.4×4.4×13.2 (12288)	4.3/17.1 (51380)	12.4×12.4×2.2 (16384)	2.2
SW $\lambda = 29$	5000	250	2500	1000	4.4×4.4×13.2 (12288)	4.3/17.1 (51413)	12.5×12.5×2.2 (16384)	2.2

SW $\lambda = 33$	5000	290	2900	1000	4.4×4.4×13.3 (12288)	4.3/17.0 (51376)	12.5×12.5×2.2 (16384)	2.2
BKS <i>OOOR</i> =0.9	6963	220	2200	800	4.9×4.9×14.6 (31104)	2.4/9.8 (16380)	14.7×14.7×2.4 (46656)	3.0
BKS <i>OOOR</i> =0.95	6963	302	3000	800	5.2×5.2×15.7 (31104)	2.6/10.5 (16344)	15.7×15.7×2.6 (46656)	2.4
BKS <i>OOOR</i> =1.0	6963	325	3200	800	5.3×5.3×16.0 (31104)	2.7/10.7 (16404)	16.0×16.0×2.7 (46656)	2.3
BKS <i>OOOR</i> =1.1	6963	336	3400	800	5.4×5.4×16.4 (31104)	2.7/10.9 (16464)	16.3×16.3×2.7 (46656)	2.1
BKS <i>OOOR</i> =1.2	6963	348	3500	800	5.5×5.5×16.6 (31104)	2.8/11.0 (16228)	16.6×16.6×2.8 (46656)	2.0

### 3.2.3 Mechanical testing procedures and conditions

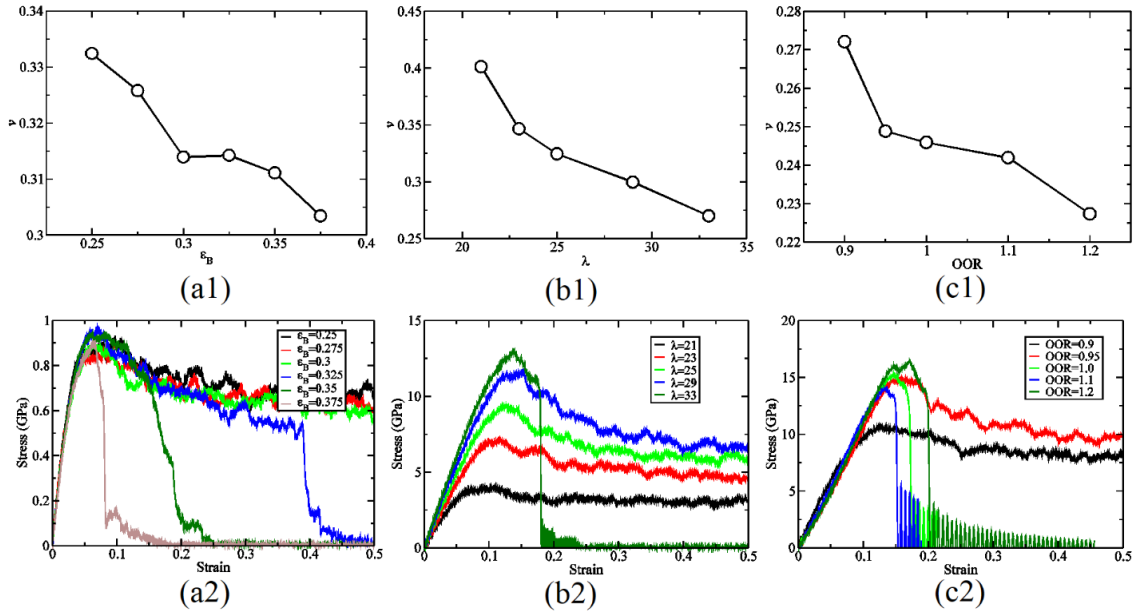
Four different types of mechanical tests were carried out on different amorphous samples: uniaxial tension tests on bulk amorphous samples, uniaxial tension tests on amorphous nanowires, simulated compact tension tests on the pre-cracked slab samples, and pure shear tests on slab samples. The first three mechanical tests are to reveal the intrinsic ductility of glassy systems, while the last mechanical test is for analyzing the energy penalty for shear band formation.

For uniaxial tension tests on a bulk sample, the simulation box was subjected to a constant true strain rate ( $\dot{\epsilon}_0$ ) in the loading direction (the Z-direction) of 0.2, 0.5, and  $1.25 \text{ ns}^{-1}$  for BLJ, SW, and BKS systems, respectively. The box sizes in the X- and Y-direction were coupled to barostats to maintain zero-stress, thus mimicking the stress states in uniaxial tension tests. For uniaxial tension tests on an amorphous nanowire, the sample was subjected to the same true strain rate as above along the axial direction (the Z-direction). Free surfaces ensure zero-stress in the transverse directions. For compact tension tests with pre-cracked samples, the sample was subjected to tension in the Y-direction with the same true strain rates as above. The sample was coupled to a barostat in the X-direction to maintain zero-stress. The thickness of the slab (box size in the Z-direction) is fixed to mimic the plane strain loading condition. For pure shear tests, slab samples were stretched in the X-direction, again at the above true strain rates for each amorphous system. The box sizes in both the Y-direction and Z-direction were coupled

to barostats to maintain  $\sigma_{YY} = -\sigma_{XX}$  and  $\sigma_{ZZ} = 0$ . For all of the above mechanical tests, a thermostat was coupled to the system to maintain the temperature at 10%  $T_g$  to prevent sample melting due to heat generation upon severe plastic deformation

### 3.3 The effect of potential tuning on the intrinsic ductility of amorphous samples

The intrinsic ductility of amorphous solids was revealed by uniaxial tension tests on bulk and nanowire samples, as well as compact tension tests with a pre-existing crack. Specifically, the failure modes of the amorphous samples under uniaxial tension are of primary interests. In addition, whether the pre-existing crack grows under compact tension tests and whether there is accompanying plastic deformation also correlate directly to the intrinsic ductility of these samples. In this section, the effect of bonding (adjusted by potential tuning) on the intrinsic ductility of amorphous solids is detailed below.



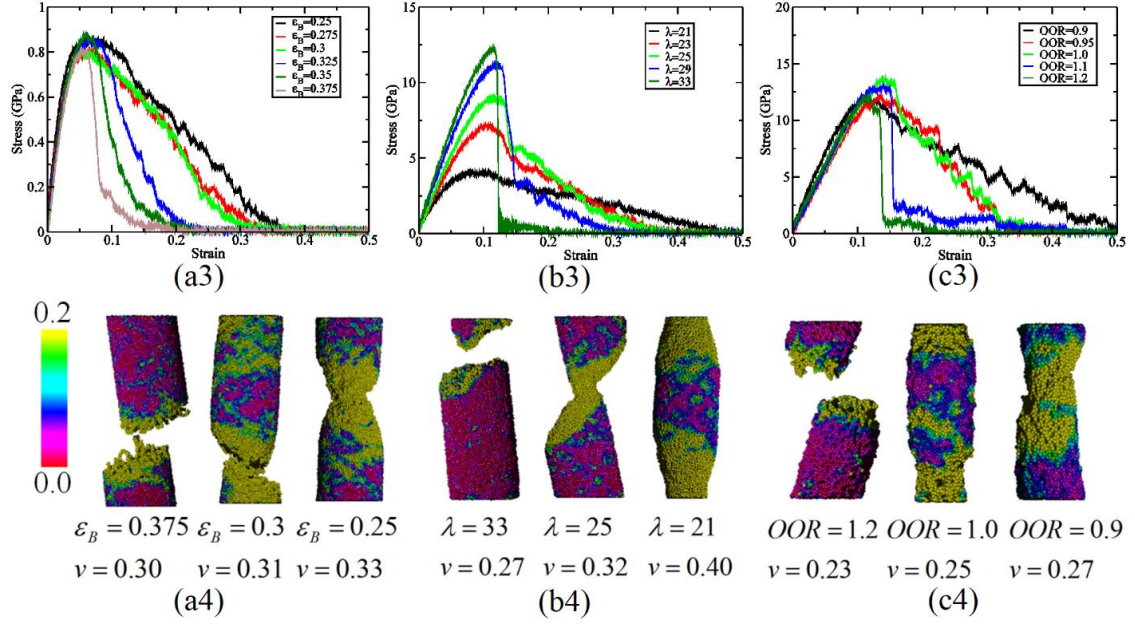


**Figure 3.1. Poisson's ratio for the BLJ, SW, and BKS systems as a function of  $\varepsilon_B$ ,  $\lambda$ , and OOR, respectively (a1, b1, and c1). True stress-true strain curves for bulk samples (a2, b2, and c2) and engineering stress-true strain for nanowire samples (a3, b3, and c3), for the BLJ, SW, and BKS systems under uniaxial tension tests, respectively. The sample morphologies for nanowire samples at 30% tensile strain (a4, b4, c4). It is clear that, for all three systems, BTD transition occurs as the bonding covalency decreases. Atoms are colored according to the local shear strain (red refers to 0% strain while yellow refers to 20% strain or above) as shown at the bottom.**

### 3.3.1 Uniaxial tension tests

Fig. 3.1(a1, b1, c1) show the Poisson's ratio as a function of the adjustable force-field tuning parameters. The Poisson's ratio was measured using its original definition

$$\nu = -\frac{\varepsilon_{Transverse}}{\varepsilon_{Loading}} \quad \text{within 1\% strain (within the elastic regime) in the uniaxial tension}$$

tests of the bulk amorphous sample. It is clear that, as bonding covalency increases, the Poisson's ratio decreases. Note that the amorphous samples were prepared under otherwise identical conditions. Such observed strong correlation indicates that, the Poisson's ratio, albeit defined and measured as an elastic constant, can serve as a sensitive indicator of the bonding covalency in amorphous samples.

The stress-strain responses of amorphous solids under uniaxial tension loading can be found in Fig. 3.1 (a2, b2, and c2 for bulk samples; a3, b3, and c3 for nanowire samples). Both bulk samples (with periodic boundary conditions, or PBCs, in all three directions) and glassy nanowires (PBC only in the loading direction; with surfaces) were systematically tested. The purpose is to investigate whether the PBCs and surfaces can affect the fracture behaviors of amorphous solids. It has been shown that both PBCs and surfaces can affect the yield point of glasses.<sup>167,168</sup> As shown in Fig. 3.1(a2), the BLJ bulk sample with the highest  $\varepsilon_B$  of 0.375 fails at a tensile strain below 10 %, while the sample with the lowest  $\varepsilon_B$  of 0.25 flows continuously. Fig. 3.1(a3) also shows the stress-strain curves for glassy BLJ nanowires, which are mostly consistent with the deformation behavior of bulk glasses. Moreover, the intrinsic ductility of these amorphous samples can be inferred from the morphologies of the nanowire samples under tension. As shown in Fig. 3.1(a4), the deformation mode of the amorphous nanowires transits from cleavage fracture, to shear fracture and eventually to necking, as the covalency decreases in the BLJ system. The same trends in terms of stress-strain responses and deformation morphologies were observed in the SW and BKS systems, as shown in Fig. 3.1 (b, and c). Thus, as the covalency decreases (equivalently,  $\nu$  increases), the amorphous solids exhibit BTB transitions.

### 3.3.2 Compact tension tests

In addition to uniaxial tension tests, simulated compact tension tests in samples with pre-existing cracks were carried out. These simulations provide a qualitative understanding of the resistance of amorphous solids to crack extension. Compact tension tests were conducted for only three levels of bonding covalency for each amorphous system. This is due to the substantially higher computational demand for the compact tension simulations than the uniaxial tension tests described in the preceding section. As shown in Fig. 3.2, amorphous samples with low covalency (low  $\varepsilon_B$ ,  $\lambda$ , and *OOR*, thus high  $\nu$ ), exhibit extensive plastic deformation leading to blunted cracks, while samples with high covalency (high  $\varepsilon_B$ ,  $\lambda$ , and *OOR*, thus low  $\nu$ ), fracture readily with little plastic deformation.

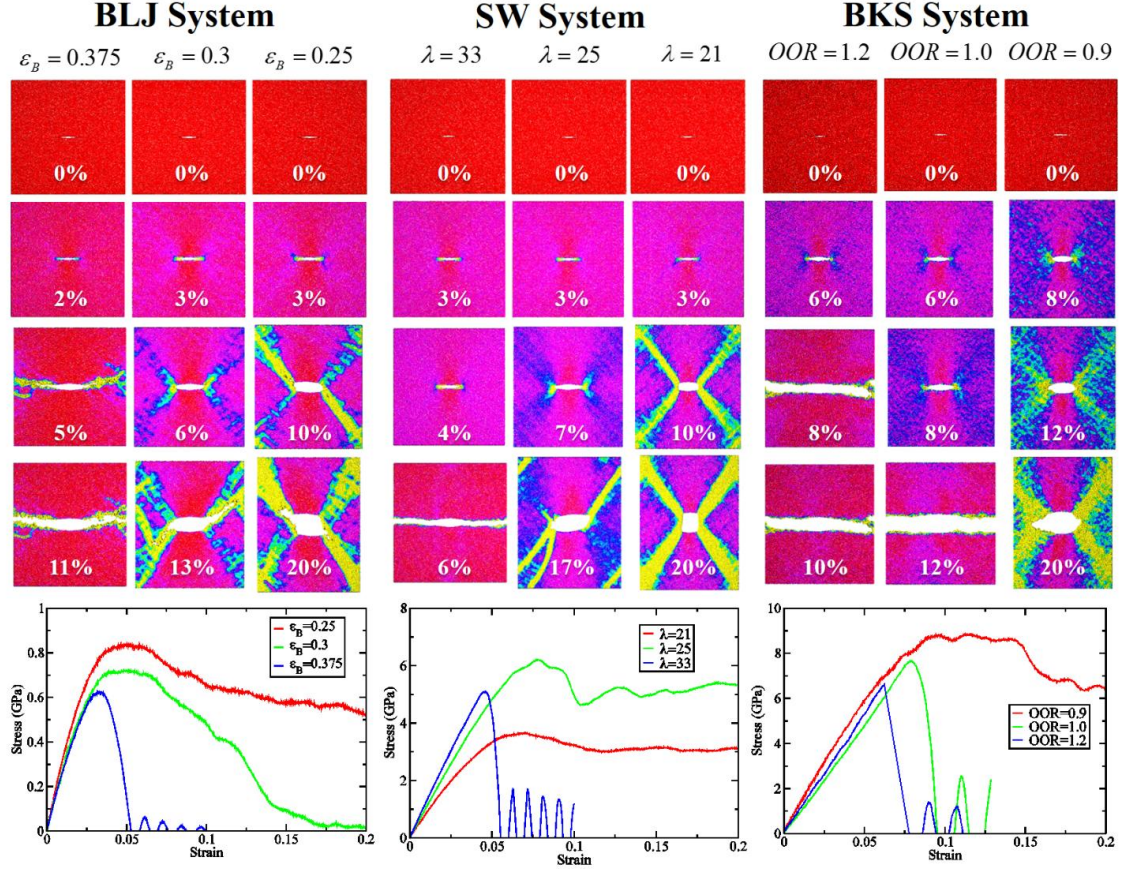


**Figure 3.2.** Deformation distribution morphologies for compact tension tests samples with pre-existing cracks, below which the corresponding true stress-true strain curves are shown. High covalency in bonding leads to weak resistance to crack growth. The precise sample dimensions can be found in Table 3.1. The color scheme is identical to that in Figure 3.1.

Due to the presence of the crack, the strength (taken as the peak stress in the stress-strain curves) of the brittle BLJ amorphous solid ( $\varepsilon_B=0.375$ ) reduces almost 30% from 0.91 GPa to 0.63 GPa, while the most ductile BLJ solid ( $\varepsilon_B=0.25$ ) reduces only 10% from 0.93 GPa to 0.84 GPa. Similarly, the crack causes the brittle SW solid ( $\lambda=33$ ) to suffer a 60% loss from 13 GPa to 5.1 GPa. However, upon introduction of the crack, the most ductile SW solid ( $\lambda=21$ ) reduces its strength by merely 10% from 4.1 GPa to 3.7 GPa. The crack leads to 60% strength reduction for the brittle BKS solid ( $OOOR=1.2$ ) from 16.5 GPa to 6.6 GPa, while decreases the strength of the ductile BKS solid ( $OOOR=0.9$ ) about 18% from 10.9 GPa to 8.9 GPa. Therefore, the presence of cracks

reduces the strength of brittle samples significantly, but only causes considerably less strength loss for ductile samples. The strength values of the sample without cracks were taken from the preceding section (uniaxial tension tests of bulk samples in Fig. 3.1). This observation is somewhat similar to experimental reports that tough MGs show similar values in notched and fatigue pre-cracked fracture toughness, while brittle MGs give different values.<sup>67</sup> The ductile or brittle responses in the simulated compact tension tests agree well with the uniaxial tensile tests of bulk samples and glassy nanowires.

### 3.4 Understanding BTD transitions: shear vs cleavage competition

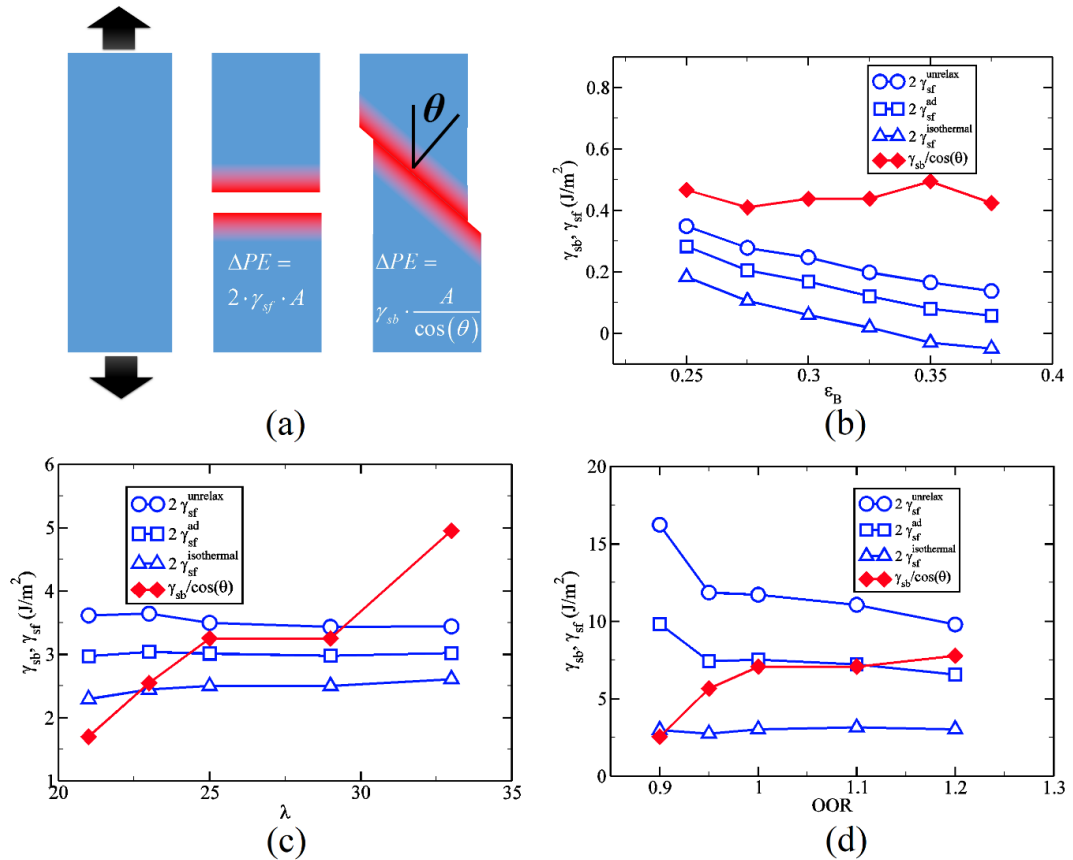


**Figure 3.3.** (a) Schematics of the competition in terms of the energy costs between cleavage and shear for a cylindrical sample under uniaxial tension: (left pane) sample in tension with stored elastic energy; (middle pane) cleavage releases elastic energy, but is penalized energetically for the newly created surfaces; (right pane) shear slip also releases elastic energy, but is penalized energetically for the extra potential energy within the shear band region.  $\theta$  is the shear band normal relative to the loading condition. The energy cost for shear, in terms of the shear

band energy  $\gamma_{sb} / \cos(\theta)$ , and the energy cost for cleavage, in terms of the surface energy  $2 \cdot \gamma_{sf}$ , are plotted for BLJ (a), SW (b), and BKS (c) systems as a function of  $\varepsilon_B$ ,  $\lambda$ , and OOR, respectively. Surface energies with different definitions are also plotted ( $\gamma_{sf}^{unrelax}$ ,  $\gamma_{sf}^{ad}$  and  $\gamma_{sf}^{isothermal}$  refer to unrelaxed, adiabatically relaxed and isothermally relaxed surface energy, respectively). The angle  $\theta$  is taken as 45 degrees for simplicity. The small negative value for the BLJ system with high covalency is due to the presence of a low-density poly-amorphous state (more details in the text).

To understand the BTD transitions observed in the MD simulations described in the preceding sections, an energy-based shear-cleavage competition was considered below. As shown in Fig. 3.1 (a4 and b4), the BTD transitions usually occur between samples that exhibit shear fracture (shear banding first and slipping along the shear band until fracture) and brittle cleavage (breaking with a fracture surface roughly normal to the uniaxial loading direction). Now consider a sample near the BTD transition under uniaxial tension tests. Immediately after yield, the sample has two options of either slipping via shear banding, or breaking via cleavage. Both deformation modes release elastically stored energy while cause additional energy penalties. The energy penalty associated with shear banding is the elevated potential energy inside the shear band region. For cleavage, the energy penalty arises from the exposed new surfaces. This is illustrated in Fig. 3.3. Thus, the BTD transition in amorphous solids can be understood from the competition between fracture and shear in terms of the surface energy and the shear band energy. This consideration is analogous to comprehending the intrinsic ductility of crystalline materials in terms of the unstable stacking-fault energy and the surface energy.<sup>169</sup>

### 3.4.1 Surface energy measurement

To estimate the surface energy, bulk amorphous samples were separated sufficiently far apart to introduce two new surfaces. The potential energy increase of the whole sample normalized by the total surface area created is the unrelaxed surface energy,  $\gamma_{unrelaxed}$ . The samples were then subjected to an adiabatic relaxation for 50 and 20 ps for BLJ and SW systems, respectively. Thus, the adiabatically relaxed surface energy,

$\gamma_{ad-relaxed}$ , can be calculated. The samples were further coupled to heat baths at their original working temperatures,  $T_{end}$ , for 100 and 40 ps for BLJ and SW systems, respectively. Upon such aggressive heat removal, the isothermally relaxed surface energy,  $\gamma_{isothermal-relaxed}$ , can be calculated.

As shown in Fig. 3.3, the surface energy decreases from the unrelaxed surface energy to the adiabatically relaxed surface energy, and then to the isothermally relaxed surface energy. It should be noted that  $\gamma_{unrelaxed}$  somewhat defines the upper bound for the surface energy for ideal cleavage (flat fracture surfaces). During fast crack propagation, heat generated upon relaxation cannot be dissipated quickly enough. Therefore,  $\gamma_{isothermal-relaxed}$  associated with aggressive cooling can be regarded as the lower limit of the surface energy for ideal cleavage.

For the BLJ system, the surface energy decreases as  $\varepsilon_B$  increases, as both the number density and the cohesive energy of the system decrease as the bonding covalency increases. For both the SW and BKS systems, the surface energy stays roughly the same. The only exception is the most ductile BKS sample ( $OOOR=0.9$ ), which has a substantially higher surface energy than the other BKS samples. This is because of the presence of five-coordinated silicon atoms (~26%), which leads to a much denser structure (the number density increases about 30% from the BKS system with  $OOOR=1.2$  to that with  $OOOR=0.9$ ).

On a last note, the isothermally relaxed surface energies for two of the most brittle BLJ samples appear to be negative. Due to the repulsive bump imposed in the interatomic potential, a BLJ sample with high bumps possesses a polyamorphous low-density state with a low potential energy. Therefore, atoms near the newly created surfaces relax to low-density local states, which lead to overall negative surface energy. It should be stressed that those two BLJ solids with negative  $\gamma_{isothermal-relaxed}$  are still cohesive and mechanically stable, which can be seen from various mechanical tests.

### 3.4.2 Shear band energy measurement

Shear band is a thin layer of material at which plastic deformation localizes. Once formed, the shear band can further broaden as the sample slips along the shear band.<sup>170–172</sup> The shear band energy,  $\gamma_{sb}$ , is defined as the excessive potential energy of the newly-formed shear banding layer over its area, thus has the same unit as the surface energy. It is apparent that fracture precedes shear band formation for brittle amorphous solids under uniaxial tension, preventing quantitative characterization of shear bands in those samples. To promote the formation of shear bands without the complication of fracture, we conducted isothermal pure-shear mechanical tests on amorphous thin slab samples to measure the shear band energy.

The potential energy increase ( $\Delta PE$ ) in the system due to loading, consists of the stored elastic energy ( $\Delta PE_{Elastic}$ ) and the potential energy increase due to shear band formation ( $\Delta PE_{SB}$ ). The stored elastic energy can be straightforwardly calculated as,

$$\Delta PE_{Elastic} = \frac{1}{2\mu} \tau^2 \cdot V, \text{ where } \mu, \tau, \text{ and } V \text{ are the shear modulus, shear stress, and}$$

system volume, respectively. Thus, the total potential energy increase as a result of shear band formation can be calculated as  $\Delta PE_{SB} = \Delta PE - \Delta PE_{Elastic}$ . Fig. 3.4 shows the typical deformation morphology, in which the shear band orients along the diagonal direction, with the shear band area being  $\sqrt{L_x^2 + L_y^2} \cdot L_z$ , assuming only one single shear band is present.  $L_x$ ,  $L_y$ , and  $L_z$  are dimensions of the system ( $L_z$  is the thickness of the amorphous slab). The calculated potential energy increase in excess to the stored elastic energy is shown in Fig. 3.5 at different strains. It remains zero in the elastic regime, climbs sharply as the shear band initiates, and then further increases at a significantly slower pace as the shear band broadens. A uniform deviatoric shear strain (8% for the BLJ system and 12% for the SW and BKS systems, for the lower yield strain in BLJ samples) was used to identify the completion of the shear band initiation. Thus, the shear band energy can be calculated as,

$$\gamma_{sb} = \frac{N \cdot \Delta PE_{SB}^0}{\sqrt{L_x^2 + L_y^2} \cdot L_z} \quad (3.1)$$

Here,  $N$  is the number of atoms in the system.  $\Delta PE_{SB}^0$  is the potential energy increase per atom for shear band initiation.

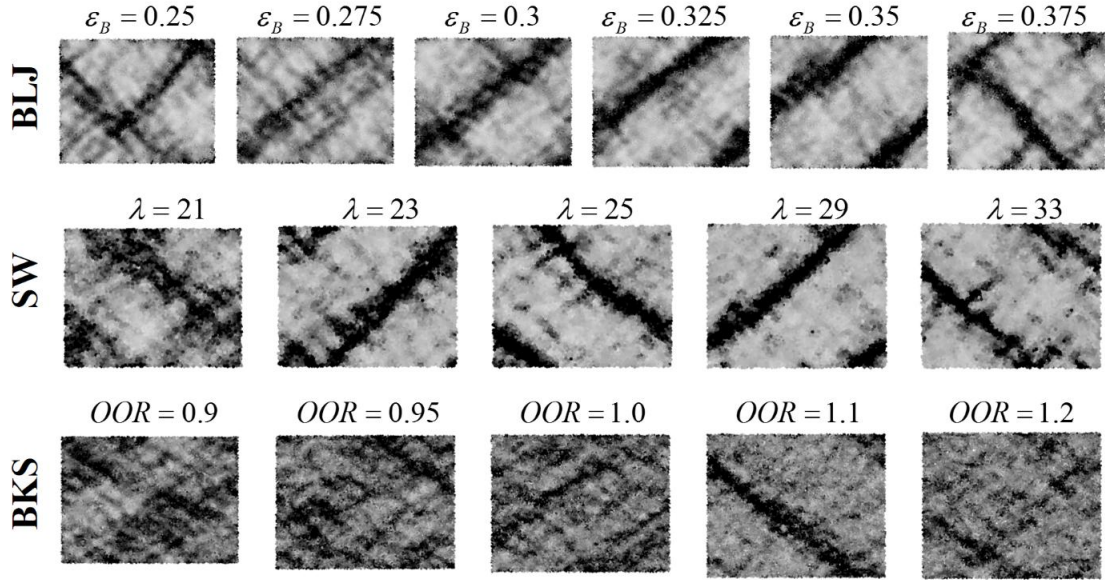


**Figure 3.4.** The deformation morphologies of pure shear tests on bulk amorphous samples with thin-slab geometries. The pure shear is conducted by tension in the X-direction and compression in the Y-direction with equal and opposite stresses. The Z-direction (thickness direction) is stress-free. The snapshots were taken at 12% of pure shear strain. The atoms are colored according to their local shear strain. Gray and black corresponds to 0% to 30% local shear strain, respectively.

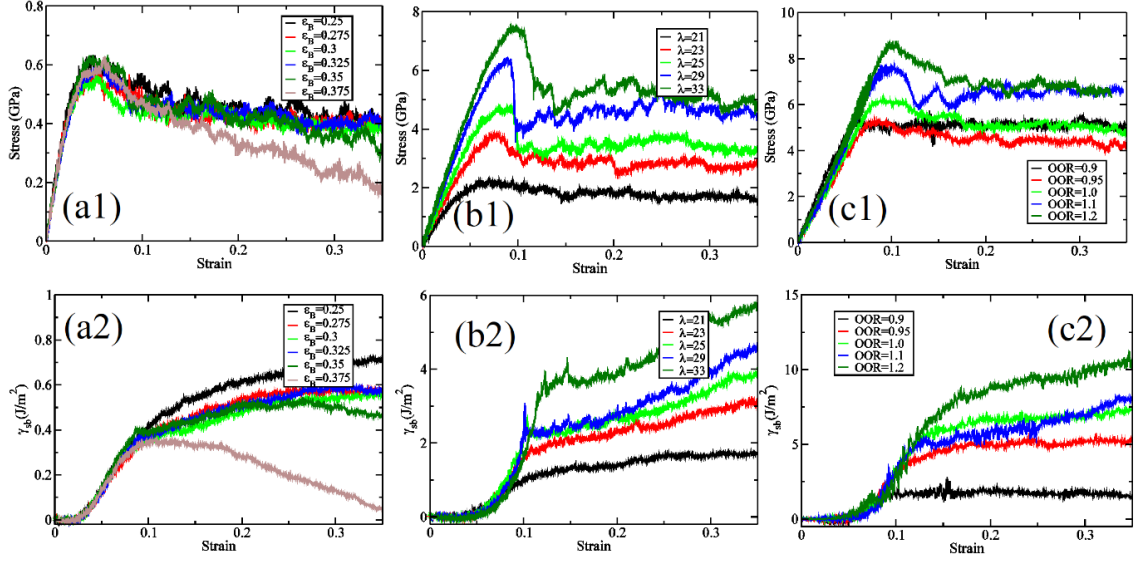


**Figure 3.5.** The stress-strain curves for pure-shear tests on bulk amorphous samples with thin-slab geometries: (a1) BLJ; (b1) SW; and (c1) BKS systems. The potential energy increase due to shear band formation (excluding elastic energy stored) is plotted in (a2, b2, and c2) for BLJ, SW, and BKS systems, respectively.

It should be noted that, as shown in Fig 3.4, the occurrence of one single shear band is rare. Instead, situations such as multiple shear bands or one dominant shear band with secondary shear bands are more common. This leads to overestimation of the shear band energy using Eq. (3.1). Moreover, the shear band energy estimated here does not include the heat generation upon shear band formation. The consideration of only the potential energy is reasonable at low temperatures. Thus, the shear band energy estimation described above should be considered semi-quantitative. We also carried out similar pure-shear loading without a thermostat. It was found that the heat generation upon the formation of the shear band roughly equals to the corresponding potential energy increase. This is different from later stage slipping along the shear band, in which the bulk of the mechanical energy is dissipated as heat with minor potential energy increases due to broadening.

The resulting shear band energies for different amorphous solids in all three systems are shown in Fig. 3.3 (b, c, and d). As the bonding covalency of the system increases,  $\gamma_{sb}$  increases for both the SW and BKS systems. However,  $\gamma_{sb}$  for the BLJ system stays roughly constant. This is because the BLJ system becomes less dense as  $\varepsilon_B$  increases

(23% decrease in number density from the BLJ sample with  $\varepsilon_b = 0.25$  to the BLJ sample with  $\varepsilon_b = 0.375$ ).

### 3.4.3 Comparing the shear band energy and surface energy

Based on the shear band energy and surface energy as measured above, one can evaluate the energy costs associated with shear fracture and brittle cleavage for samples under uniaxial tension. This analysis can help understand the BTD transitions triggered by the force field tuning. As illustrated in Fig. 3.3, the potential energy penalty for ideal cleavage with perpendicular fracture surfaces is  $2 \cdot \gamma_{sf} \cdot A$ , while the potential energy penalty for shear banding is  $\gamma_{sb} \cdot A / \cos(\theta)$ , where  $A$  is the cross section area of the sample and  $\theta$  is the angle between the shear band plane normal and the loading direction ( $\theta$  is taken as 45 degrees for simplicity). Fig. 3.3 (b, c, and d) plot  $2 \cdot \gamma_{sf}$  and  $\gamma_{sb} / \cos(\theta)$  of all three amorphous systems for direct comparison.

For the BLJ systems, as the covalency increases, the energy cost associated with shear banding stays roughly the same, while the energy cost associated with cleavage decreases dramatically. Therefore, it is increasingly more energetically favorable for the BLJ system to fracture, as  $\varepsilon_b$  increases. For the SW systems and BKS systems, samples with low covalency (low  $\lambda$  and low  $OOOR$ ) have a lower energy cost to shear and a high energy cost to cleave, and vice versa. The BTD transition occurs at the condition of equal energy cost for shear and cleavage. The actual cross-over points in Fig. 3.3 depend on the specific definition of the surface energy. It should be stressed that the energy cost estimated here for both shear and cleavage are only semi-quantitative. Nonetheless, the simple energetic arguments here agree quite well with the BTD transitions observed in our mechanical tests.

## 3.5 Link BTD transitions to the Poisson's ratio

The BTD transition in amorphous solids shown in Lewandowski et. al.'s work<sup>86</sup> was identified by the dramatic increase of the threshold elastic energy release rate (fracture

energy  $G$ ), which is difficult to measure directly in MD simulations due to the small sample size (particularly for ductile amorphous solids). Fortunately, we have shown in preceding sections that the uniaxial tension tests on bulk and nanowire samples, as well as compact tension tests on pre-cracked samples, reveal almost identical BTD transitions as the bonding covalency decreases. Brittle/ductile behavior in terms of tensile ductility (revealed by uniaxial tension tests) and crack extension resistance (revealed by compact tension tests on pre-cracked samples) can be very different. For instance, even BMGs with high fracture toughness exhibit zero tensile ductility, embrittled by size-dependent shear band-to-crack transition. In our uniaxial tension tests, the shear band-to-crack transition was suppressed by the short sample length, which leads to the excellent agreement between BTD transitions in uniaxial tensile tests and crack extension tests. Therefore, one can infer the crack resistance by its tensile ductility (given that embrittlement/toughening mechanisms are suppressed). Detailed discussions on possible embrittlement mechanisms can be found in Section 3.7.

For simplicity, we chose to use the failure strain in the uniaxial tension tests of the bulk glass samples (the true strain at which the true stress drops to half of the maximum value) to identify BTD transitions. A threshold failure strain was chosen to be 25%, higher than the failure strains of the apparent brittle samples of all three systems. Under the above failure strain criterion, it was found that the threshold Poisson's ratio ( $\nu_{BTD}$ ) corresponding to the BTD transition is about 0.31, 0.28 and 0.24 for the BLJ, SW, and BKS systems, respectively. It should be noted that, a different critical failure strain will only slightly modify the value of  $\nu_{BTD}$ . For instance,  $\nu_{BTD}$  remains at 0.28 for the SW system under a critical failure strain of 20%. Importantly, the critical Poisson's ratio seems to be system-dependent, which resonates with past theoretical prediction<sup>90</sup> and experimental results on metallic glasses.<sup>66,67,92</sup> Moreover, the critical Poisson's ratio of 0.31 for the BLJ system agrees well with the experimental value of 0.31-0.32 for metallic glasses.<sup>86</sup> Another encouraging piece of experimental evidence is that, densified silica with  $\nu$  approaching 0.25, was found to be capable of shear flow under indentation resulting in pile-ups.<sup>160</sup> To explore the commonality of the BTD transitions in the three families of amorphous solids, Fig. 3.6 maps out the intrinsic ductility of amorphous solids in the domain of the Poisson's ratio and the average coordination number ( $\nu$ - $CN$

diagram), clearly delineating a ductile regime and a brittle regime.  $CN$  conveniently differentiates various glassy systems. It can be seen that  $\nu_{BTD}$  increases with  $CN$ , which can be understood from a simple model described as follows. This  $\nu$ - $CN$  diagram can serve as a guide to rational design of tough glasses.

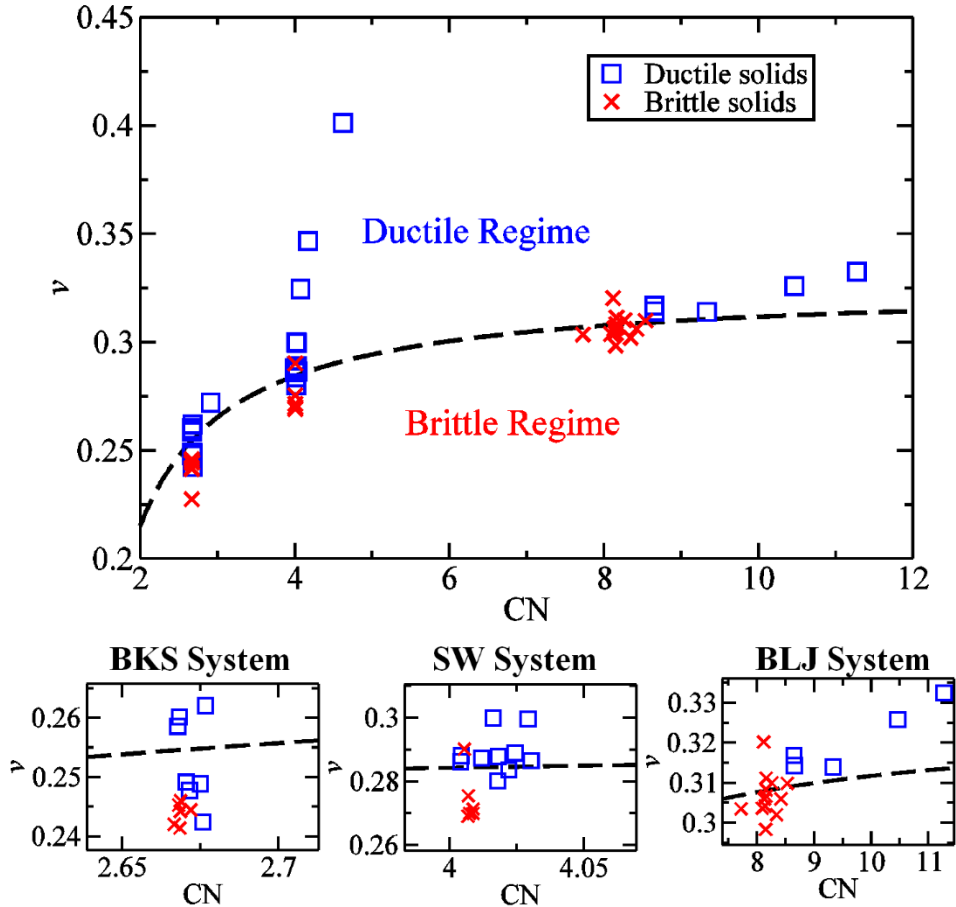


**Figure 3.6.** The  $\nu$ - $CN$  diagram showing the ductile regime and the brittle regime for three families of glassy solids (with zoomed-in views at the bottom). Amorphous samples exhibit either ductile (blue squares) or brittle behaviors (red crosses), depending on their covalency, processing, or testing conditions. The designation of brittle or ductile behaviors is according to the failure strain (Fig. 3.1) in uniaxial tension tests of bulk samples. The black dashed line of  $\nu_{BTD}$ - $CN$  is from the simple model described in Eq. (3.9).

### 3.5.1 A simple BTD model

The critical Poisson's ratio at the BTD transitions can be understood as a function of the average coordination number through a simple model described as follows. For simplicity, a single-component amorphous solid is considered here, which is closest to the SW system. The relevant physical parameters are bond strength  $\varepsilon_b$ , bond length  $b$ , average coordination number  $CN$ , and number density  $n_a$ . The surface energy can be estimated by the number of bonds broken per unit area, which can be written as,

$$\gamma_{sf} \sim b \cdot n_a \cdot \frac{CN}{2} \varepsilon_b \quad (3.2)$$

The shear band consists of amorphous materials that have been severely sheared with a minimal thickness of roughly twice the bond length. The shear band energy, in excess to the undeformed material, consists of the energy penalty due to angular deviation from the preferred covalent bond angle. The shear band energy also consists of energy penalty due to bond extension and compression upon shear, which was omitted here. It should be noted, however, the inclusion of this pair contribution will lead to identical conclusions of Eq. (3.5). Thus, the shear band energy can be estimated as,

$$\gamma_{sb} \sim 2b \cdot n_a \cdot \frac{CN^2}{2} \cdot \varepsilon_a \cdot [f(\theta_{sb}) - f(\theta_0)] \quad (3.3)$$

$\varepsilon_a$  is the energy scale for the angular constraints.  $\varepsilon_a \cdot f(\theta_{sb})$  and  $\varepsilon_a \cdot f(\theta_0)$  represent the potential energy terms from angular constraints for the shear banding region and the undeformed material, respectively. The bonding covalency can be defined as a dimensionless factor,

$$\chi = \frac{\varepsilon_a}{\varepsilon_b} \quad (3.4)$$

which characterizes the relative strength of the angular constraint over the pairwise bond strength.

Based on the shear-cleavage competition, the BTD transition occurs when the surface energy penalty matches the shear band energy penalty. Combining Eqs. (3.2-

3.4), one can obtain the covalency at the BTD transition ( $\chi_{BTD}$ ), that is inversely proportional to the coordination number:

$$\chi_{BTD} \sim \frac{1}{CN} \quad (3.5)$$

On the other hand, the strength of the angular constraint of the covalent bonding can also be correlated to the packing factor  $\alpha$  of the amorphous solids. Solids with strong covalent bonds usually have lower packing factors and vice versa. For the single-component amorphous solid considered here, the upper limit of the packing factor without any covalency ( $\chi = 0$ ) can be taken as the random close packing factor (RCP),  $\alpha_{RCP} \approx 0.64$ .<sup>173</sup> As covalency increases, the packing factor generally decreases. To a first order approximation, it was assumed that the covalency is linearly related to the amount of reduction in packing factor from the upper limit of  $\alpha_{RCP}$ :

$$\chi \sim \alpha_{RCP} - \alpha \quad (3.6)$$

From Eq. (3.5) and Eq. (3.6),

$$\frac{CN_0}{CN} = \alpha_{RCP} - \alpha_{BTD} \quad (3.7)$$

in which  $CN_0$  is assumed to be a constant comprising proportionality parameters in Eq. (3.5) and Eq. (3.6).

The Poisson's ratio can be linked to the above treatment using the empirical relation obtained by Makishima and Mackenzie, which relates the packing factor and the Poisson's ratio based on experimental data for oxide glasses,<sup>174</sup>

$$\alpha = \frac{1}{6\gamma\left(\frac{1}{2} - \nu\right)} \quad (3.8)$$

Note that the above equation originates from a Mie-type interatomic interaction appropriate for oxide glasses. Here,  $\gamma$  is the slope between the bulk modulus and the product of the packing factor and the Young's modulus, which was fitted to be 1.2 by Makishima and Mackenzie.<sup>174</sup> Now, combining Eqs. (3.7) and (3.8),  $\nu_{BTD}$  can be expressed as a function of  $CN$ ,

$$\nu_{BTD} = \frac{1}{2} - \frac{1}{6\gamma \left( \alpha_{RCP} - \frac{CN_0}{CN} \right)} \quad (3.9)$$

Eq. (3.9) rationalizes that the critical Poisson's ratio is indeed system dependent and increases with increasing CN. The black dashed line shown in Fig. 3.6 was obtained by fitting Eq. (3.9) to the MD results in which  $CN_0$  is found to be 0.5 and  $\gamma$  is about 1.5.

### 3.6 Link angular constraint to the Poisson's ratio

To understand the link between angular constrain and Poisson's ratio in an analytical form, also in terms of chemical bonding and atomic structure, is particularly challenging and has only seen limited success under highly simplified situations.<sup>93,94,175</sup> For instance, even for isotropic amorphous system with pair interactions, due to local non-affine relaxation, the Poisson's ratio can take a wide range of values (for instance, BLJ systems shown in Fig. 3.1), as opposed to  $\nu=0.25$  expected from the well-known Cauchy relation assuming no relaxation. To the best of knowledge, there has been no investigation on the analytical form of the Poisson's ratio for systems with many-body interactions.

Here we only attempt to derive the analytical expression for the Born term of Poisson's ratio ( i.e., for deformation without non-affine relaxation), which can help rationalize effect of the angular constraint on Poisson's ratio.

We first consider a system with the nearest neighbors interacting with a homogeneous harmonic bond. Then we consider the system with a homogeneous angular constraint on the bond angle.

#### 3.6.1 The model of homogeneous harmonic bond

Assume that in the system the harmonic bond is evenly distributed in all directions, i.e. we can set the density of harmonic bond

$$\vec{B}_d = (r \sin \theta \cos \phi, r \sin \theta \sin \phi, r \cos \theta) \quad (3.10)$$

at a certain spherical direction  $(\theta, \phi)$  to be a constant  $\rho$ . The bond length is  $r$ .

Uni-axial tension can be expressed as :

$$T_n = \begin{bmatrix} 1-v\epsilon & 0 & 0 \\ 0 & 1-v\epsilon & 0 \\ 0 & 0 & 1+\epsilon \end{bmatrix} \quad (3.11)$$

with the Poisson's ratio is set to be  $v$ , and the strain is  $\epsilon$ .

The bond after tension will be:

$$\vec{B}_d \times T_n = (r \sin \theta \cos \phi (1-v\epsilon), r \sin \theta \cos \theta (1-v\epsilon), r \cos \theta (1+\epsilon)) \quad (3.12)$$

The bond length change is  $\Delta \vec{B}_d$ :

$$\begin{aligned} |\Delta \vec{B}_d| &= \sqrt{r^2 \sin^2 \theta \cos^2 \phi (1-v\epsilon)^2 + r^2 \sin^2 \theta \cos^2 \theta (1-v\epsilon)^2 + r^2 \cos^2 \theta (1+\epsilon)^2} - r \\ &= r \left( \frac{\epsilon}{2} (1-v + (1+v) \cos 2\theta) + O(\epsilon^2) \right) \end{aligned} \quad (3.13)$$

The energy  $E_b$  stored in this bond is

$$E_b = \frac{1}{2} K |\Delta \vec{B}_d|^2 \quad (3.14)$$

$K$  is the bond strength. Integrating over all directions will give the total energy  $E$  stored in the system:

$$\begin{aligned} E &= \int_0^\pi \int_0^{2\pi} \rho E_b \sin \theta d\phi d\theta \\ &= r \rho K \int_0^\pi \int_0^{2\pi} \frac{1}{2} \left( \frac{\epsilon}{2} (1-v + (1+v) \cos 2\theta) \right)^2 \sin \theta d\phi d\theta \\ &= \frac{2}{15} \pi r \rho K (3-4v+8v^2) \end{aligned} \quad (3.15)$$

As the Poisson's ratio will give the lowest elastic energy state of the system, so minimizing  $E$  yields:

$$v = \frac{1}{4}. \quad (3.16)$$

which is the Cauchy relation<sup>176</sup>.

### 3.6.2 The model of homogeneous angular harmonic spring

We consider that the system consists of pairs of bonds (triplets) with uniform distribution in all possible directions. For simplicity, the bond angle (termed  $\Omega$  below) is

a constant. We can define the pairs in two steps. First, we define one bond in the pair in the spherical coordination  $(\theta, \phi)$ .

$$\vec{B}_{d1} = (\sin \theta \cos \phi, \sin \theta \sin \phi, \cos \theta) \quad (3.17)$$

with  $r$  set to be 1, since we only care about the orientation of the bond.

Then the other bond within the pair can be any bond that forms at an angle  $\Omega$  with  $\vec{B}_{d1}$ . We can define an reference pair, and generate other pairs by rotating the reference pair about  $\vec{B}_{d1}$  by an angle  $a$ ,  $a \in [0, 2\pi]$ . Therefore we obtain the other bond

$$\begin{aligned} \vec{B}_{d2} = & (\cos a \cos \theta \cos \phi \sin \Omega + \cos \Omega \cos \phi \sin \theta - \sin a \sin \Omega \sin \phi, \\ & \cos \phi \sin a \sin \Omega + \cos a \cos \theta \sin \Omega \sin \phi + \cos \Omega \sin \theta \sin \phi, \\ & \cos \Omega \cos \theta - \cos a \sin \Omega \sin \theta) \end{aligned} \quad (3.18)$$

$\Omega$  is the angle between  $\vec{B}_{d1}$  and  $\vec{B}_{d2}$ .

Applying uni-axial tension to the system will result in a change of the angle  $\Omega$  between  $\vec{B}_{d1}$  and  $\vec{B}_{d2}$ . Let's first consider two general vectors  $\vec{P}_1$  and  $\vec{P}_2$ , both of which have a length of 1. We set  $\vec{P}_1 = (x_1, y_1, z_1)$  and  $\vec{P}_2 = (x_2, y_2, z_2)$ .

After tension (by applying the matrix in 3.11 to  $\vec{P}_1$  and  $\vec{P}_2$ ), we obtain  $\vec{P}'_1 = (x_1(1 - \nu\varepsilon), y_1(1 - \nu\varepsilon), z_1(1 + \varepsilon))$  and  $\vec{P}'_2 = (x_2(1 - \nu\varepsilon), y_2(1 - \nu\varepsilon), z_2(1 + \varepsilon))$ .

Ignoring 2<sup>nd</sup> and higher order terms of  $\varepsilon$ , the change of the angle  $\Delta\Omega$  between the two vectors can be calculated as,

$$\begin{aligned}
\sin(\Omega)\Delta\Omega &= \cos(\Omega + \Delta\Omega) - \cos\Omega \\
&= \frac{\vec{P}'_1 \vec{P}'_2}{|\vec{P}'_1||\vec{P}'_2|} - \frac{\vec{P}_1 \vec{P}_2}{|\vec{P}_1||\vec{P}_2|} \\
&= \frac{\vec{P}_1 \vec{P}_2 + 2\epsilon(z_1 z_2 - v(x_1 x_2 + y_1 y_2))}{|\vec{P}_1||\vec{P}_2| + \epsilon(z_1^2 + z_2^2 + v(x_1^2 + x_2^2 + y_1^2 + y_2^2))} - \frac{\vec{P}_1 \cdot \vec{P}_2}{|\vec{P}_1||\vec{P}_2|} \\
&(\because |\vec{P}_1||\vec{P}_2| = 1) \\
&= \frac{\vec{P}_1 \vec{P}_2 + 2\epsilon(z_1 z_2 - v(x_1 x_2 + y_1 y_2)) - \vec{P}_1 \cdot \vec{P}_2 (1 + \epsilon(z_1^2 + z_2^2 + v(x_1^2 + x_2^2 + y_1^2 + y_2^2)))}{1 + \epsilon(z_1^2 + z_2^2 + v(x_1^2 + x_2^2 + y_1^2 + y_2^2))} \\
&= \frac{2\epsilon(z_1 z_2 - v(x_1 x_2 + y_1 y_2)) - \vec{P}_1 \cdot \vec{P}_2 \epsilon(z_1^2 + z_2^2 + v(x_1^2 + x_2^2 + y_1^2 + y_2^2))}{1 + \epsilon(z_1^2 + z_2^2 + v(x_1^2 + x_2^2 + y_1^2 + y_2^2))} \\
&= \epsilon[2(z_1 z_2 - v(x_1 x_2 + y_1 y_2)) - \vec{P}_1 \cdot \vec{P}_2 (z_1^2 + z_2^2 + v(x_1^2 + x_2^2 + y_1^2 + y_2^2))]
\end{aligned}$$

Replacing  $\vec{P}_1$  and  $\vec{P}_2$  with  $\vec{B}_{d1}$  and  $\vec{B}_{d2}$ , the change  $\Delta\Omega$  is calculated to be

$$\Delta\Omega = \frac{1}{8}(1+v)\epsilon(((3+\cos 2a)\cos 2\theta + 2\sin^2 a)\sin 2\Omega - 8\cos a \sin^2 \Omega \sin 2\theta) \quad (3.19)$$

The energy  $E_a$  stored in one angular spring with spring constant  $K_a$  is

$$E_a = \frac{1}{2} K_a (\Delta\Omega)^2 \quad (3.20)$$

Taking both the energy stored in angular and linear bond into consideration, the total energy E stored due to uni-axial tension is

$$\begin{aligned}
E &= \int_0^\pi \int_0^{2\pi} \rho_b E_b \sin \theta d\phi d\theta + \int_0^{2\pi} \int_0^\pi \int_0^{2\pi} \rho_a E_a \sin \theta da d\theta d\phi \\
&= \frac{2}{15} \pi r \rho_b K_b (3 - 4v + 8v^2) \epsilon^2 + \frac{8}{15} \sin^2 \Omega \pi^2 \rho_a K_a (1+v)^2 \epsilon^2
\end{aligned} \quad (3.21)$$

$K_a$  and  $K_b$  are the spring constants for the angular spring between the bonds and the linear springs between atoms.  $\rho_a$  and  $\rho_b$  are the density of the angular and linear spring. The additional 1/2 pre-factor of the integration of energy of the angular spring is because each pair has been counted twice.

Minimizing the total energy E will give the Poisson's ratio as

$$\nu = -1 + \frac{5B}{4B + 2A \sin^2 \Omega} \quad (3.22)$$

in which  $A = \pi \rho_a K_a r$ ,  $B = \rho_b K_b$ .

If the angular constraint A is much larger than the linear bonding term B, then the Born term of Poisson's ratio will be close to -1. If A is small comparing to B, then the Born term of Poisson's ratio will be close to 1/4. So we can see that increasing the angular constraint, or covalency, will decrease the born term of the Poisson's ratio. At the current moment, the analytical derivation of the relaxation term is still beyond reach.

### 3.7 Sample-size effects on the tensile ductility

Common to MD simulation studies, the sample size is significantly smaller than bulk samples. Particularly, as the uniaxial tensile tests were used to reveal the intrinsic ductility of the amorphous sample, it is important to discuss whether any embrittlement or toughening effects are applicable here. There are three size effects frequently referred to in nanoscale mechanical tests, which will be discussed below in the context of our MD simulations.

First, smaller samples store less elastic energy to drive fracture, leading to a “toughening” size effect for small samples. For a sample under uniaxial tension without a crack, an energy argument analogous to Griffith's theory can be made as follows: upon brittle failure, the stored elastic energy ( $\frac{1}{2} E \varepsilon_f^2 V$ ) at failure has to be higher than the surface energy ( $2A \gamma_{sf}$ ). Here,  $E, \varepsilon_f, V, A, \gamma_{sf}$  is the Young's modulus, failure strain, volume, cross-section area, and the surface energy, respectively. Thus, the *necessary* condition for perfect samples to cleave upon uniaxial tension is to have a minimal length of  $\frac{4\gamma_{sf}}{E \varepsilon_f^2}$ . It can be shown that both BLJ and SW samples are much longer than the above minimal length requirement. To test this size effect further, additional uniaxial tension tests were carried out on bulk amorphous samples that are twice as long in the loading direction. Those longer samples behave very similarly to the samples with the original lengths.

The second possible size/shape effect is that, for a slender sample, once slip is initiated, the stress-drop due to elastic unloading is less than the stress increase due to cross-section area reduction, resulting in unstable slipping.<sup>177</sup> This is a shape-induced embrittlement effect for slender samples. According to the above unstable slipping mechanism, the critical aspect ratio for our sample was calculated to be between 10:1 to 6.7:1 (assuming a slip angle of about 45 °, and a yield strain of ~10 to 15%, depending on the amorphous system). Note that, the aspect ratio of the glassy nanowires investigated here is about 2:1 (length to diameter), which is far below the critical aspect ratio estimated above to invoke the unstable-slipping mechanism. Thus, the brittle fractures observed here are not a result of the unstable-slipping induced by the shape.

The third size effect is the embrittlement effect due to the maturation of stable shear banding to unstable crack propagation.<sup>178-180</sup> The transition from shear bands to cracks is thermomechanical in nature and occurs over a typical distance of sub-microns. Thus, a sufficiently long length of a sample permits crack formation and “embrittles” the material. The amorphous samples considered here are much smaller than the typical length scale for the shear band-to-crack transition. Furthermore, all brittle amorphous samples observed in this study cleave directly without a preceding shear slipping. Therefore, the shear-band-to-crack thermomechanical embrittlement effect is not applicable in our simulations. But as a potentially important fracture mode for large sized metallic glasses, cavitation inside a shear band will be investigated thoroughly in the following chapters.

All three size- or shape-induced toughening or embrittlement effects discussed are not applicable to the size/geometry of the amorphous samples used here. In other words, the brittle or ductile behaviors observed in our MD simulations results from the intrinsic ductility of the sample, instead of the above three size/shape effects. Nonetheless, there might be other unknown size-effects that could affect the fracture behavior, which might systematically shift the actual brittle-to-ductile transition points. Such systematic shift, if any, is likely to be small, as the  $v_{BTD}$  transition (0.31) for model metallic glasses (the BLJ system) agrees well with the experimental observation (0.31-0.32)<sup>86</sup> for bulk samples.

### 3.8 Summary

In summary, extensive MD studies on three distinct amorphous systems using one force-field tuning scheme reveal that the angular constraint or covalency in bonding controls both the BTD transition and the Poisson's ratio of amorphous solids. A higher angular constraint increases the ratio of the shear band energy to the surface energy, and therefore promotes brittle fracture. We also observed that a higher angular constraint decreases the Poisson's ratio. Such a link between the angular constraint and Poisson's ratio is analytically understood for the non-affine relaxation situation. Based on the shear banding VS cleavage model and the empirical relations between Poisson's ratio, packing density and covalency, we build a simple model to rationalize that the critical Poisson's ratio for BTD transition is system (CN) dependent. This study may also have implications for other empirical relations linking the Poisson's ratio to densification,<sup>181</sup> fragility,<sup>182,183</sup> and glass-transition.<sup>184</sup>

## 4. History-independent Properties of Running Shear Bands

Since the tensile fracture of metallic glasses always occurs in the running shear band (a shear band in operation), in this chapter we aim to introduce the fact, via the examples of free volume and stress state, that the properties of the running shear band, controlled by the thermomechanical state in the shear band, are history independent. The insight gained here serves as the foundation of the simulation design and the choice of parameters in fracture analysis presented in the following chapters.

### 4.1 Free volume in the running shear band

While free volume is widely believed to be the controlling parameter to the flow and the fracture properties of shear bands in amorphous solids<sup>185,186</sup>, here we show that free volume inside a running shear band, being history independent, is controlled by the thermomechanical state. On the other hand, we find that changes in the thermomechanical state can induce subtle changes in properties that cannot be detected by means of free volume. Here we choose to focus on the thermomechanical state inside the shear band rather than on free volume in the fracture analysis presented in Chapter 5 and 6.

#### 4.1.1 Introduction

Shear localization or shear banding phenomenon controls the fracture behavior of metallic glasses<sup>40</sup>. The leading concept for shear band initiation is athermal softening associated with disordering of local short range ordered atomic clusters<sup>60,187</sup>. This structural transformation is usually accompanied by free volume generation. The shear-induced volumetric strain (SIS) is also observed in other dense-packed disordered materials, including granular and colloidal assemblies<sup>188,189</sup>. The free volume generated by shear has been considered as a representative parameter for the mechanical behavior

---

Portions of this chapter previously appeared as: Luo, J., Shi, Y. & Picu, C. R. Shear-induced volumetric strain in CuZr metallic glass. *Int. J. Eng. Sci.* **83**, 99–106 (2014).

of these disordered materials<sup>41,186,189</sup>.

Despite the recognized importance of the issue, the answers to several fundamental questions related to free volume production in metallic glasses remain elusive. For instance, the magnitude of SIS and its dependence on external thermomechanical loads is not entirely understood. While some calculations suggested that SIS is larger than 10%<sup>10,38,190,191</sup>, recent experiment results<sup>192,193</sup> indicate that its value is limited to a few percent. The difficulty of free volume evaluation during shear stems from the extreme spatial and temporal localization of deformation in the shear band. During the evolution of a shear band, the local material is far from equilibrium and has a complicated thermo-mechanical history<sup>56</sup>. This makes it difficult to evaluate the “state” of the material in experiments. In addition, cavitation occurs preferentially in the shear band<sup>85,104,194,195</sup>, which complicates the interpretation of experimental results. Therefore, further studies of SIS under well-controlled thermo-mechanical conditions are warranted. A related question is whether shear always induces dilatational hydrostatic strain, and whether compaction is possible under certain conditions. While small amplitude cyclic shear deformation is known to induce overaging, or compaction in glasses<sup>196,197</sup>, it is interesting to ask whether compaction may occur during monotonic, large strain shear deformation.

To address these issues, we perform molecular dynamics (MD) simulations of shear deformation of a model CuZr glass under a range of temperature, pressure and shear strain rate conditions. Multiple samples of the same composition are produced by quenching from the melt at different cooling rates. Samples subjected to shear reach a steady flow state after yielding. The free volume increases during the transient and is constant in the steady state (SS). We find that the steady state free volume is controlled by the temperature, hydrostatic stress and shear strain rate in the shear band, and is independent of the initial as-quenched state of the sample. Interestingly, under compression we find that SIS can be negative.

### 4.1.2 Simulation methodology

The CuZr glass considered in this study is described by an embedded atom potential<sup>100</sup> which has been validated against a large set of experimental and *ab initio* data, such as cohesive energies, enthalpies of mixing, elastic constants, etc. The potential has been used in a number of simulation studies on CuZr metallic glass<sup>100,194,198,199</sup>.

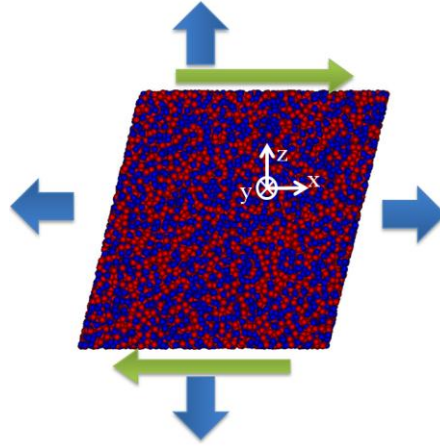


**Figure 4.1. Simulation cell showing a snapshot of the atomic configuration (red and blue atoms represent Zr and Cu, respectively). Simple shear deformation is applied under isothermal-isobaric conditions. The three normal stresses are controlled independently to keep the same constant values. Periodic boundary conditions are applied in the three directions of the coordinate system.**

The model contains 27,000 atoms of which 50% are Cu and 50% are Zr. MD simulations are carried out using the LAMMPS package<sup>200</sup>. The integration time-step is 1 fs. The number of atoms and the temperature are constant during each simulation. The hydrostatic stress is also kept constant and is imposed by independently controlling the normal stress in the three directions of the reference frame (Fig. 4.1). The Nose-Hoover equations of motion are used<sup>162,163</sup> and periodic boundary conditions are applied in all directions.

The system is equilibrated for 0.1 ns in the liquid state, at 2,000K. The glassy samples are prepared by quenching the liquid under zero pressure from the temperature of the equilibrated melt to selected lower temperatures ranging from 60K to 1000K. The cooling rates used are  $\dot{\Theta} = 0.1$  K/ps, 0.5 K/ps, 2K/ps, and 10 K/ps (denoted as G0.1,

G0.5, G2 and G10, respectively). To explore the limit, we also generated a set of “instantly quenched” samples (denoted as G-instant) by imposing a temperature step from 2,000 K to 60 K at zero pressure followed by equilibration at the lower temperature for 0.2 ns. The quenching rate in this case is dictated by the rate of response of the thermostat. The temperature stabilizes within the first 2 ps of the equilibration and hence we estimate the cooling rate for these “instant quenched” samples to be  $\dot{\Theta} \sim 1,000$  K/ps.

The as-quenched samples are cubic, with an edge length of about 8 nm. This dimension varies slightly with the quenching rate and temperature. The samples are then equilibrated for 20 ps at the pressure and temperature of the shear test, after which shear deformation is applied under NPT conditions. The shear strain rate is kept constant in each test and equal to  $0.5 \text{ ns}^{-1}$ , if not stated otherwise. The maximum deformation applied is 200% engineering shear strain.

#### **4.1.3 The effect of quenching rate**

Let us study first the effect of the quenching rate on the SIS. Samples quenched at different rates are considered and deformed in shear at zero pressure and a temperature of 60K. Figure 4.2(a) shows the variation of the volume of all samples. The starting point is the volume of the as-quenched state, which decreases as the quenching rate decreases. Upon start-up of the shear deformation, the volume increases rapidly and then gradually converges to a steady state (SS). The volume and the applied shear stress become constant in SS, within the inherent (but small) atomic fluctuations. It is noted that the slowest quenched sample takes longer to reach the steady state due to a stronger tendency of shear localization.

In the initial phase of shear deformation, dilatation takes place heterogeneously in the sample. The shear strain is also non-uniform. As deformation proceeds, these incipient shear bands broaden and eventually engulf the entire sample. Steady state is reached at that stage. The thickness of the shear band has been shown to grow diffusively<sup>97</sup>. This phenomenon is more evident in sample G0.1 which has the slowest convergence to the steady state. A similar dependence of the degree of strain localization on the quenching rate was observed before in metallic glasses<sup>60,201</sup>.

Despite the difference between the as-quenched states, the SS of all samples overlap. The memory of the initial state is erased by the shear flow which creates a characteristic structure. This conclusion holds for the SS resulting from shear deformation applied with other strain rates and at other temperatures and pressures. An equivalent conclusion was obtained earlier<sup>19</sup> relative to the shear stress corresponding to the steady state. This flow stress is also independent of the history of the material.

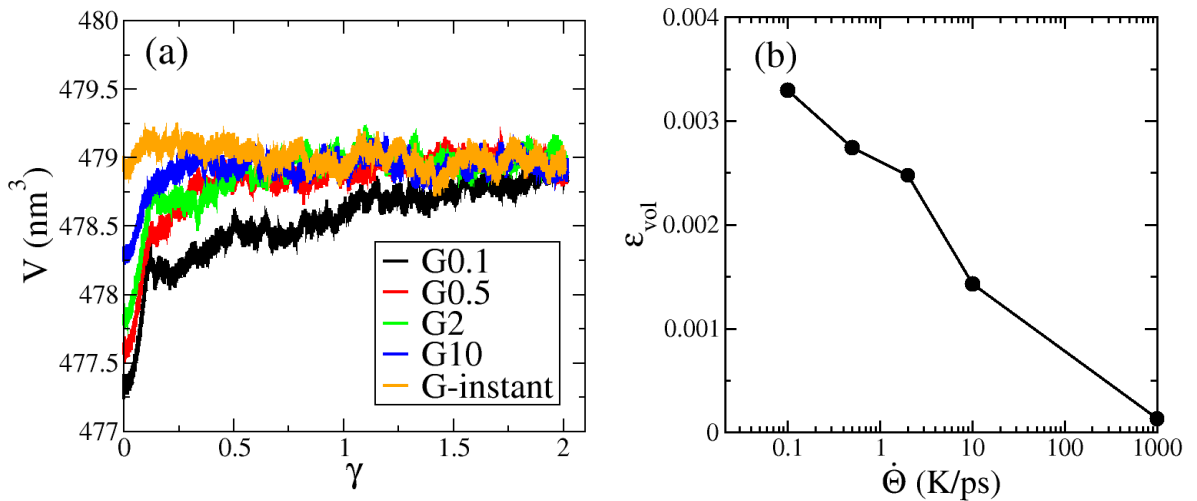


**Figure 4.2.** (a) Evolution of sample volume during isothermal simple shear deformation under zero hydrostatic stress and at  $T = 60\text{K}$  for samples quenched with various quenching rates,  $\dot{\Theta}$ . The shear strain rate used is  $0.5 \text{ ns}^{-1}$ . (b) shear induced volumetric strain as a function of quenching rate.

Figure 4.2(b) shows the volumetric strain measured from the curves in Fig. 4.2(a) as a function of quenching rate. The SIS effect disappears when the quenching rate is sufficiently high; specifically, the “instant quenched” samples exhibit essentially no shear-induced volumetric change. The overall dependence of the SIS on the quenching rate is logarithmic, which is in agreement with the experimental measurement of volume relaxation over much longer time scales<sup>202</sup>. The slope of the curve in Fig. 4.2(b),  $\partial\epsilon_{vol}/\partial\log\dot{\Theta}$ , is approximately 0.08%, which is higher than the experimental observation of 0.03%<sup>202</sup>. The magnitude of the volumetric strain is small, ranging from approximately 0 to 0.3%. Since the volumetric strain increases with decreasing  $\dot{\Theta}$ , we expect that these simulations provide values significantly lower than the experimental

ones. The slowest quenching rate of 0.1K/ps used here, is still 10 orders of magnitude faster than common quenching rates used in experiments. With the slope measured in Fig. 4.2(b) it is possible to extrapolate to the experimental range of  $\dot{\Theta}$ . The predicted SIS for a glass quenched at  $\dot{\Theta} = 1\text{K/s}$  is 1.3%, which is in reasonable agreement with recent experimental observations by two groups reporting shear-induced dilatation strains of 1.14%<sup>193</sup> and approximately 2%<sup>192</sup>, respectively.

#### 4.1.4 The effect of temperature

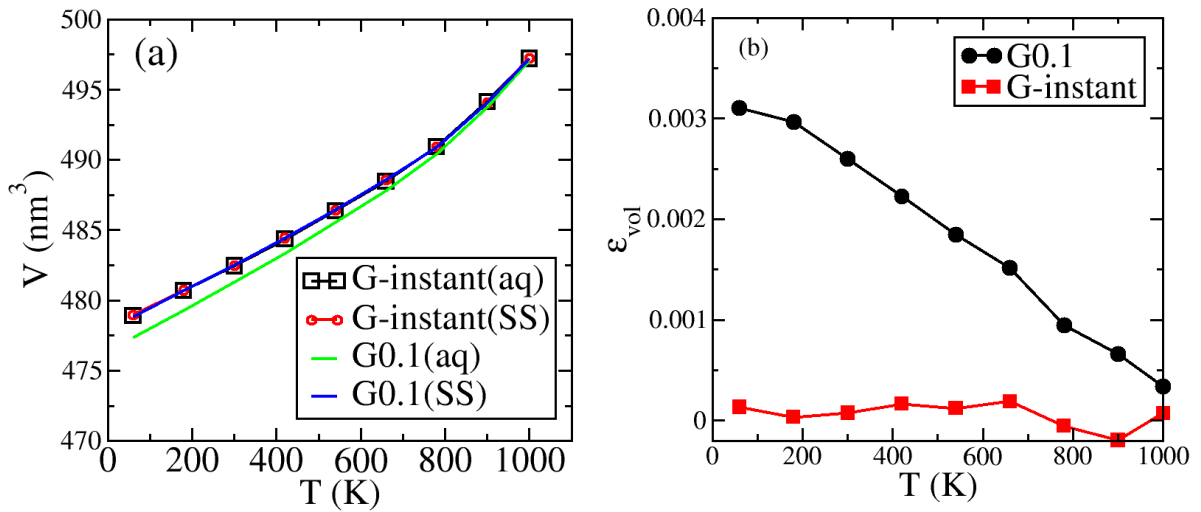


**Figure 4.3. (a) Variation of the volume of the as-quenched (aq) and steady shear (SS) states of G0.1 and G-instant samples with the temperature imposed during shear deformation,  $T$ . (b) The corresponding shear-induced volumetric strain as a function of temperature.**

We discuss next the effect of the temperature of the shear test on SIS. To this end, we consider samples G0.1 and G-instant and deform them at zero pressure and temperatures ranging from 60K to 1000K. Fig. 4.3(a) shows the variation of the volume of the as-quenched and SS states as a function temperature. For the G0.1 glass, the volume difference between the SS and as-quenched states (or the SIS) is noticeable at lower temperatures and decreases with increasing temperature. Therefore the SIS decreases with increasing temperature as shown in Fig. 4.3(b). In the case of the G-instant glass, the volumes of the as-quenched and SS states are identical; therefore, SIS

is zero for all temperatures (Fig. 4.3(b)). Remarkably, the volume-temperature curves of the SS state for G0.1 and G-instant overlap over the entire temperature range, reinforcing the observation that the density of the SS state is quenching rate independent.

The as-quenched state curves in Fig. 4.3(a) can be used to estimate the glass transition temperature to be approximately 700K for the G0.1 sample and 900K for G-instant. Since the SS state has the same density as the instantly quenched state (G-instant), we speculate that the glass transition temperature of G-instant defines the temperature at which the SIS vanishes for all glasses quenched with smaller  $\dot{\Theta}$ .

#### 4.1.5 The effect of strain rate

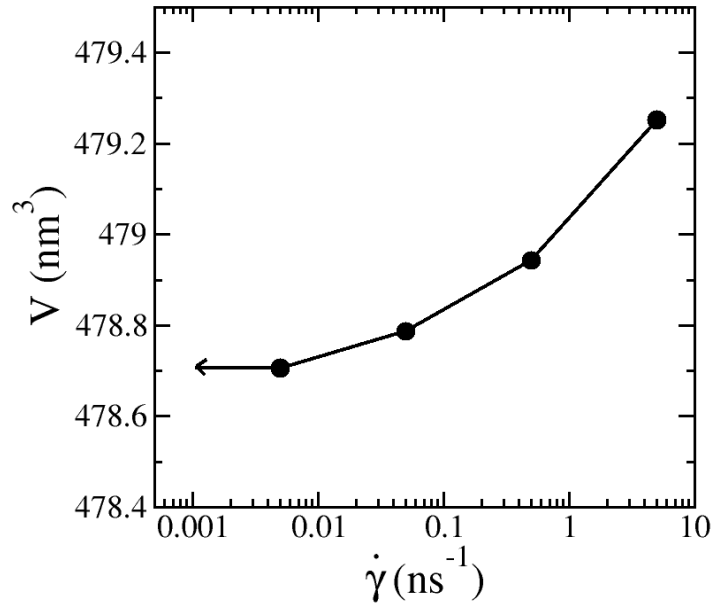


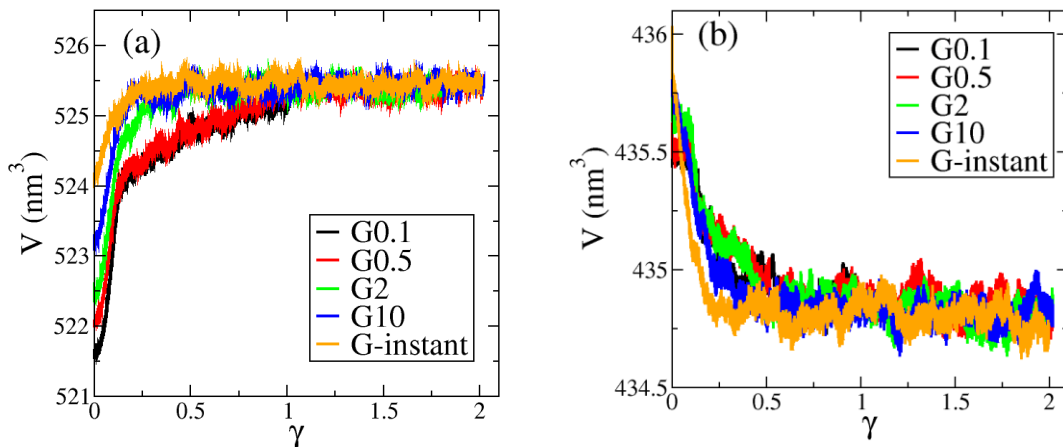
**Figure 4.4. Volume of the steady shear state as a function of the shear strain rate for simple shear deformations performed at zero hydrostatic stress and  $T = 60$  K.**

Relaxation is expected to take place dynamically during shearing. Fig. 4.4 shows the variation of the sample volume under SS conditions with the applied strain rate,  $\dot{\gamma}$ . It is seen that indeed, the volume of the SS state decreases when the shear strain rate decreases. This dynamic relaxation contributes to the reduction of the SIS effect with increasing temperature (Fig. 4.3). However, the effect of temperature is more

pronounced than that of strain rate, at least in the range of parameters accessible by MD simulations.

#### 4.1.6 The effect of pressure

Hydrostatic stress is usually present in shear bands forming in bulk metallic glasses. Due to the transient nature of the shear banding process, real-time in situ measurements of the dependence of SIS on the local pressure is still absent with current experimental techniques. Therefore we proceed to estimate the dependence of the SIS on the applied pressure. The pressure is applied from the beginning of the equilibration stage that precedes shear deformation. Pressures in the range of -12 GPa (compressive) to 8 GPa (tensile) are considered. Fig. 4.5(a) and (b) show the variation of the sample volume during shear deformation under pressures of 8 GPa and -12 GPa, respectively, for all glasses considered in this study. The trends in Fig. 4.5(a) are identical to those in Fig. 4.2(a). The density of the SS state is independent of the quenching rate under both compressive and tensile pressures. In Fig. 4.5(b) compaction is observed during shear. Since the pressure is constant along the entire sample trajectory, this effect can only be due to the variation of the effective bulk modulus during shearing.



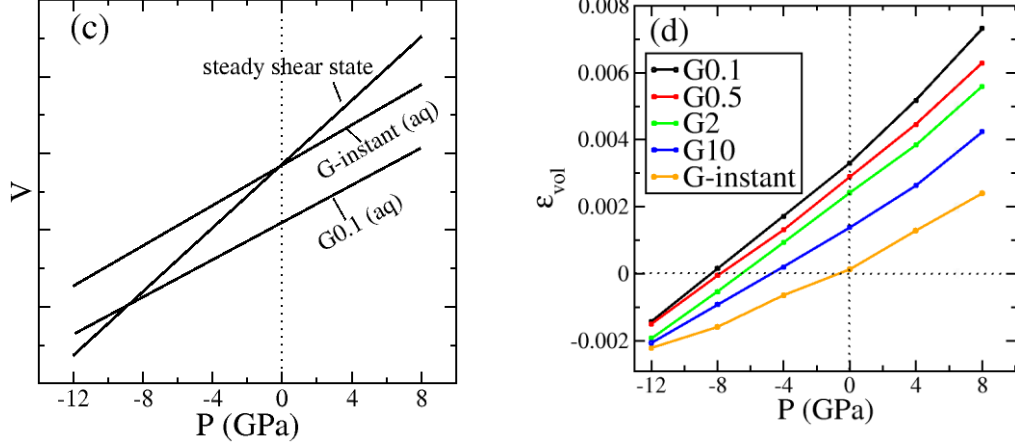


**Figure 4.5. Evolution of sample volume during isothermal simple shear deformation under hydrostatic pressure (a)  $P = 8$  GPa and (b)  $P = -12$  GPa, and at  $T = 60$  K for samples quenched with various rates,  $\dot{\Theta}$ . The shear strain rate used is  $0.5 \text{ ns}^{-1}$ . (c) Schematic illustration of the variation of volume with pressure for the SS state and the as-quenched state of G-instant and G0.1. (d) Volumetric strain as a function of pressure,  $P$ , for samples quenched with various rates.**

Fig. 4.5(c) shows a schematic representation of the variation of the sample volume with the applied pressure. As the quenching rate increases, the volume of the sample in the as-quenched state increases (Figs. 4.2(a) and 4.5(a)). The volume of SS and G-instant states are identical (Fig. 4.2(a)). The bulk moduli of the as-quenched states are insensitive to the quenching rate<sup>126,194</sup>. The bulk modulus of G-instant is only 1% smaller than that of G0.1. However the bulk modulus of the SS is lower than that of G0.1 by 5%. This effect is seen in Fig. 4.5(d) which shows the dependence of the SIS effect on the applied pressure. The slopes of the curves can be computed as:

$$\partial \epsilon_{vol} / \partial P = \partial \left( \frac{V_{ss} - V_{aq}}{V_{aq}} \right) / \partial P = \frac{V_{ss}}{V_{aq}} \left( \frac{1}{K_{ss}} - \frac{1}{K_{aq}} \right) \quad (4.1)$$

where  $V$  and  $K$  represent the volume and effective bulk modulus, respectively. The subscript  $aq$  and  $ss$  stand for as-quenched and steady shear states. Using the values of  $V_{ss}$  and  $V_{aq}$  from Figs. 4.5(a) and (b), the results in Fig. 4.5(d) indicate that the effective bulk modulus of SS state,  $K_{ss}$ , is smaller than that of the as-quenched state,  $K_{aq}$ .

Therefore one may write the superposition of the shear-induced dilatation strain and the volumetric strain associated with the variation of the bulk modulus during the isobaric shearing as:

$$\varepsilon_{vol}(P) = \varepsilon_{vol}(0) + \frac{V_{ss}}{V_{aq}} \left( \frac{1}{K_{ss}} - \frac{1}{K_{aq}} \right) P. \quad (4.2)$$

where  $\varepsilon_{vol}(0)$  stands for the SIS effect, while the second term represents the variation of the volumetric strain due to the variation of the bulk modulus from the as-quenched value to the SS value. Note that  $\varepsilon_{vol}(0)$ ,  $K_{aq}$  and  $V_{aq}$  depend on the quenching rate, while  $K_{ss}$  and  $V_{ss}$  does not since it refers to the SS state which is independent of the sample history.

An interesting observation is that while the free volume content is the same in G-instant and the corresponding SS state, the effective bulk modulus is not, indicating that there exist subtle differences between G-instant and the SS state that cannot be captured by free volume.

#### 4.1.7 Summary

In summary, the MD simulation results discussed here reveal that the steady shear state of the CuZr glass exhibits a density equal to that of the instantly quenched liquid over a wide temperature range under zero pressure, independent of the initial state of the glass. The SIS is a result of the rejuvenation of aged glass state to the “instantly quenched” liquid state. Hence, SIS does not have to be dilatational if the instantly quenched liquid state possesses a higher density. Indeed, this was observed in amorphous Si in an earlier study<sup>117</sup>. The magnitude of SIS depends on the quenching rate, and is estimated to be on the order of few percent even for glass cooled at experimental cooling rates. This is in agreement with recent experimental results<sup>192,193</sup>. The effective bulk modulus of the SS state is lower than that of the as-quenched state which, in turn, is also known to be independent of the quenching rate for this material system. This observation suggests that there exist subtle differences between the instantly quenched liquid and SS state that cannot be described by free volume alone.

## 4.2 Liquid Feature of the Stress State in the Running Shear Band

The stress state in the running shear band is expected to be one of the controlling factors for the fracture in shear bands and yet has not been carefully studied before. In

this chapter, via systematic atomic simulations on seven distinct amorphous solids, we reveal that the stress state of a running shear band will always be liquid-like hydrostatic plus shear stress state. However, the liquid-like stress state does not hold for network glasses or phase segregated glasses.

#### 4.2.1 Introduction

Similar to dislocations in crystalline materials, shear bands are the major plasticity carriers in metallic glasses, and control the yielding and even fracture<sup>10,40</sup>. Despite the vital importance, the nature of shear banding in metallic glasses has not been completely understood. The shear banding process can be separated into the initiation stage (the formation of a cross-the-sample shear band) and the subsequent gliding stage (the shear slip along the shear band)<sup>53,58</sup>. The initiation of a shear band has long been ascribed to work softening or shear thinning<sup>203</sup>. Structural disorder inside the shear band was predicted to be the origin of work softening, instead of thermal softening<sup>203</sup>. This notion was supported by experiments<sup>2,49,39,56</sup> and atomic simulations<sup>60,204</sup>. Specifically, the structural disorder has been characterized as a break-down of the local stable clusters or the short-range order<sup>52,53,101,204</sup> in atomic simulations.

During the subsequent gliding stage, the shear band endures high local shear strain under extremely high rate, which can lead to temperature rise<sup>56,58</sup>, void formation<sup>96,186,205–207</sup> and the final fracture<sup>40,79</sup>. The transient dynamics a shear band experiences also depend on the materials properties and the machine stiffness<sup>55,58,208</sup>. Multiple remarkable scaling behaviors discovered in the flow state<sup>198,209,210</sup> indicate that the shear banding can be considered a mechanically driven glass-to-liquid transition. It should also be noted that this liquid-like state of the shear band appears to be weakly dependent on the quenching history of the glass<sup>60,97</sup>.

Despite the above recent advances in understanding the shear band, the local stress state in the running shear band (RSB), a shear band that is in the flow state, has not been clearly understood<sup>40</sup>. Experimentally, it is generally difficult to examine the local stress state in the RSB in experiments due to the limited spatio-temporal resolution<sup>40,127</sup>. Among existing theoretical or simulation studies,<sup>58,195</sup> it is commonly assumed that the

hydrostatic stress and shear stress in the RSB are different from the rest of sample, without direct measurements of the full stress tensor. However, complete knowledge of the stress state is essential to develop any plasticity theory involving the description of shear banding. Particularly, the thermomechanical evolution of an RSB sensitively depends on its stress state. Here, we aim to systematically investigate the stress state of a shear band once it reaches the mechanically driven flow state.

In this chapter, we conducted molecular dynamics (MD) simulations to examine the stress state of an RSB in a number of distinct model glasses. MD simulation was employed, as it can provide the necessary spatio-temporal resolution to resolve the shear banding process. The shear band features a time-scale around nanoseconds<sup>56</sup> and a thickness on the order of nanometers<sup>211</sup>. We used two types of simulation methods: large-scale simulations to study the stress state during the realistic transient evolution of the shear band under uniaxial tension tests (the method will be detailed in the Section 5.2.2), and small-scale simulations to examine the RSB under more general loadings. We found that in both the small scale and large scale simulation, the local stress state in the RSB in all of the studied model metallic glasses (except the FeP and the amorphous Si system) exhibit a liquid like hydrostatic plus shear (HS) stress state, regardless of the loading conditions and the temperature. Note that the third invariant of the HS stress state is zero, indicating that the stress state of an RSB is fundamentally changed by the shear flow and cannot be achieved by merely rotating the coordination system. The results support the notion that the shear banding is a form of shear-driven glass-to-liquid transition in metallic glasses, but not in network glasses or phase segregated glasses.

#### **4.2.2 Simulation setup and methodology**

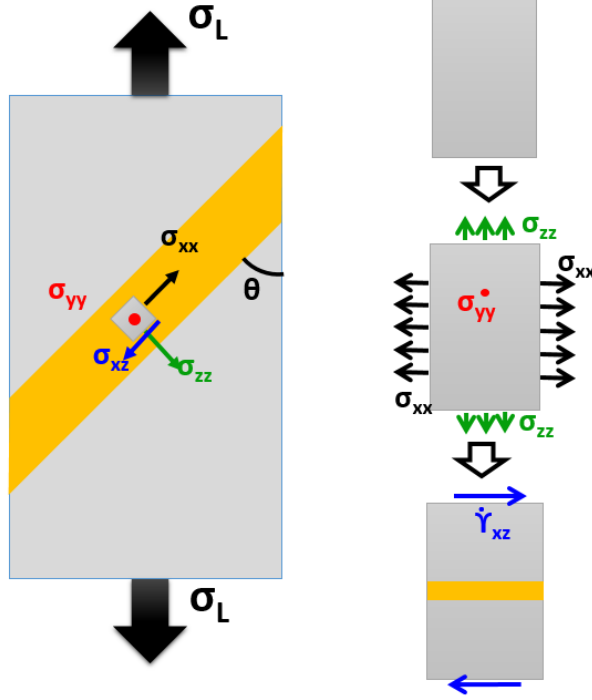


**Figure 4.6.** The schematic illustration of the simulation setups. The left pane represents the uniaxial loading mode, in which the shear band is illustrated by the yellow region. The angle of the shear band away from the loading is  $\theta$ . Note that  $\sigma_L$  can be compressive or tensile. The right pane represents a simplified simulation setup for the small-scale simulations to explore more general loading conditions. The sample is first loaded in a general stress state with controlled normal stresses. Subsequent simple shear deformation to a large strain is applied to drive a shear band under the condition of fixed volume.

We aim to explore the stress state in an across-the-sample RSB as illustrated in Fig. 4.6. Consider first an across-the-sample shear band forms during a uniaxial test as illustrated in Fig. 4.6(a). Prior to the shear band formation, the local stress state should follow (assuming plain strain condition),

$$\sigma_{zz} = \sigma_L \sin^2 \theta, \quad \sigma_{xx} = \sigma_L \cos^2 \theta \quad \text{and} \quad \sigma_{yy} = \nu \sigma_L \quad (4.3)$$

with  $\theta$  to be the shear band angle with respect to the loading direction,  $\nu$  to be Poisson's ratio, and  $\sigma_L$  to be the global tensile stress. Note that  $\sigma_L$  can be either compressive (expressed as negative values) or tensile (expressed as positive values).

We use two types of simulation setups to explore the stress state in a shear band. One type is the large-scale simulation with the perturbative static loading (PSL)

method<sup>104</sup> to directly examine the transient shear band stress state under uniaxial tension or compression tests. PSL method will be used to study the tensile fracture of metallic glasses in Chapter 5. Particularly, the shear band angle can be conveniently controlled, which allows us to study how the stress state of a shear band is affected by the shear band angle. The procedure of a PSL test (details can be found in Ref. [<sup>104</sup>]) is briefly described as follows. We first subjected the glassy sample to a conventional uniaxial tension test to 5% of tensile strain. Then the sample was replicated to the desired length and width. A shear band at an oblique angle is not affected by the periodicity because it travels through different portions of the replicas. Subsequently, two surfaces were created to allow sample gliding along the shear band. After that, we applied a heat pulse with 5 ps duration to perturb the local structure of a thin band region, in which the shear band will later nucleate. Note that after the perturbation, the thin band was relaxed at its original temperature for another 5 ps. The property of the resulting RSB will not be affected by the details of how it is initiated, due to its independence from its thermomechanical history<sup>60</sup>. To avoid high loading speed in the sample, we kept the strain rate zero after the perturbation. The setup mimics deal displacement controlled uniaxial loading under zero strain rate. Here we applied the PSL test to the modified binary Lennard-Jones (mWA)<sup>130</sup> sample with the sample size of  $120 \times 2.7 \times 360 \text{ nm}^3$  under 5% tensile strain. This model glass former, together with the other glass formers studied here, will be discussed later in this section.

The second type of mechanical test is the small-scale simulation to probe the stress state of RSB under more general temperature and stress conditions, as illustrated in Fig. 4.6(b). We controlled the initial normal stresses  $\sigma_{zz}$  and  $\sigma_{xx}$  of the small slab according to Eq. (4.3). Different from the physical meaning of  $\theta$  and  $\sigma_L$  in the context of uniaxial tension tests as illustrated in Fig. 4.6(a), in small-scale simulations,  $\theta$  and  $\sigma_L$  should be considered as two free adjusting parameters that control the initial normal stresses of the small slab system shown in Fig. 4.6(b). Although the shear band angle observed in the experiment only ranges from 30 to 45 degrees under compression and 45 to 60 degrees under tension<sup>212</sup>, in the small-scale simulation, one can tune  $\theta$  from 0 to

90 degrees to explore initial stress states that are more general. We kept  $\sigma_L$  at a constant (see Table 4.1) for a given glass, as it was found to have little effect on the attainment of HS stress state in the shear band. Consistent with the large-scale PSL test, the plane-strain condition was implemented in the small-scale tests. After the initial normal stress is stabilized, simple shear with constant strain rate was applied in the xz direction to drive the sample to form a shear band. During the simple shear deformation, the system was kept in an NVE (i.e. constant number of particles, constant volume and total energy) ensemble. The tests under NVT (i.e. constant number of particles, total volume and system temperature) ensemble will also be discussed. Temperature control and stress control used in the MD simulations follow the standard Nose-Hoover formulation<sup>162,163</sup>. The shear strain rate applied is  $2 \times 10^8 \text{ s}^{-1}$  for all systems. Periodic boundary conditions are present in all directions in the small-scale simulations.

**Table 4.1. The composition, the quenching rate, the sample size, the initial load  $\sigma_L$  and the testing temperature under NVT ensemble for the force fields employed in this study. Here compressive stresses are expressed as negative values.**

	Composition	Quenching rate	Sample size	Initial load	Testing Temperature
WA <sup>124</sup>	50:50	0.9 K/ps	$23 \times 2.7 \times 90 \text{ nm}^3$	-1.23 GPa	10 K
mWA <sup>130</sup>	50:50	0.9 K/ps	$23 \times 2.7 \times 90 \text{ nm}^3$	-1.23 GPa	10 K
KA <sup>136</sup>	80:20	0.6 K/ps	$23 \times 2.5 \times 45 \text{ nm}^3$	-1.23 GPa	10 K
FeP <sup>138</sup>	80:20	6 K/ps	$17 \times 1.7 \times 55 \text{ nm}^3$	-4 GPa	1 K
M-CuZr <sup>137</sup>	50:50	6 K/ps	$18 \times 1.9 \times 61 \text{ nm}^3$	-3 GPa	1 K
S-CuZr <sup>100</sup>	50:50	6 K/ps	$19 \times 1.9 \times 58 \text{ nm}^3$	-2 GPa	1 K
SW-Si <sup>139</sup>		5 K/ps	$24 \times 2.1 \times 60 \text{ nm}^3$	-2.5 GPa	1 K

To explore the commonality among different model metallic glasses, we applied the small-scale simulations on six commonly used model metallic glasses and a model amorphous Si. It is interesting to point out that the model amorphous silicon has been explored as a metallic glass analogue, which exhibits a number of behaviors including

shear localization similar to those in metallic glasses<sup>117</sup>. The force fields used in this study include pair wise interaction as in the binary Lennard-Jones potential parameterized by Kob Anderson (KA)<sup>136</sup>, Wahnstrom (WA)<sup>124</sup> and its modified version (mWA) based on angular constraint<sup>130</sup>, many body potential as in the widely used EAM potentials that describes CuZr<sup>137</sup> (developed by M. Mendeleev et al., termed M-CuZr here) and CuZr<sup>100</sup> (developed by H. Sheng termed S-CuZr here) and FeP<sup>138</sup> and three body interaction (angular constraint) as in the Stillinger-Weber (SW) amorphous Si system<sup>139</sup>. The simulation parameters for all these systems are listed in Table 4.1. The as-quenched temperature is 10 K for the WA, mWA and KA systems, 1 K for the three EAM systems and the SW-Si system. We choose such low temperatures in order to demonstrate that high temperature is not necessary for the attainment of the HS stress state in the shear band.

To assess the local stress state in the shear band, we partitioned the glassy sample into thin bins with thickness of about 1 nm. The choice of the bin thickness allows us to resolve the shear band yet with sufficiently low fluctuations benefited from averaging. The bins extend parallel to the shear band direction. First, virial stresses (in energy units) are calculated for each atom without dividing by atomic volume since atomic volume in a glass is usually hard to define accurately. Then the atomic stresses in each bin are summed and divided by the volume of the bin to yield the local stresses for each bin. The local stresses calculated in this way are identical to the corresponding global components before the formation of the shear band. The bin with the highest local temperature, most likely in the middle of an RSB, is taken as a representative bin to represent the stress state of the RSB. All the simulations were performed using LAMMPS<sup>200</sup>.

The primary simulation results on the stress state inside the shear band will be described below for the mWA system. First, we used the large-scale PSL tests to produce the shear band dynamically during zero strain rate uniaxial unloading. Then, we employed the small-scale tests to investigate the stress state in RSB under a more general stress state. In both situations, the shear band attains the liquid-like HS stress state.

### 4.2.3 Large-scale simulation in the mWA system

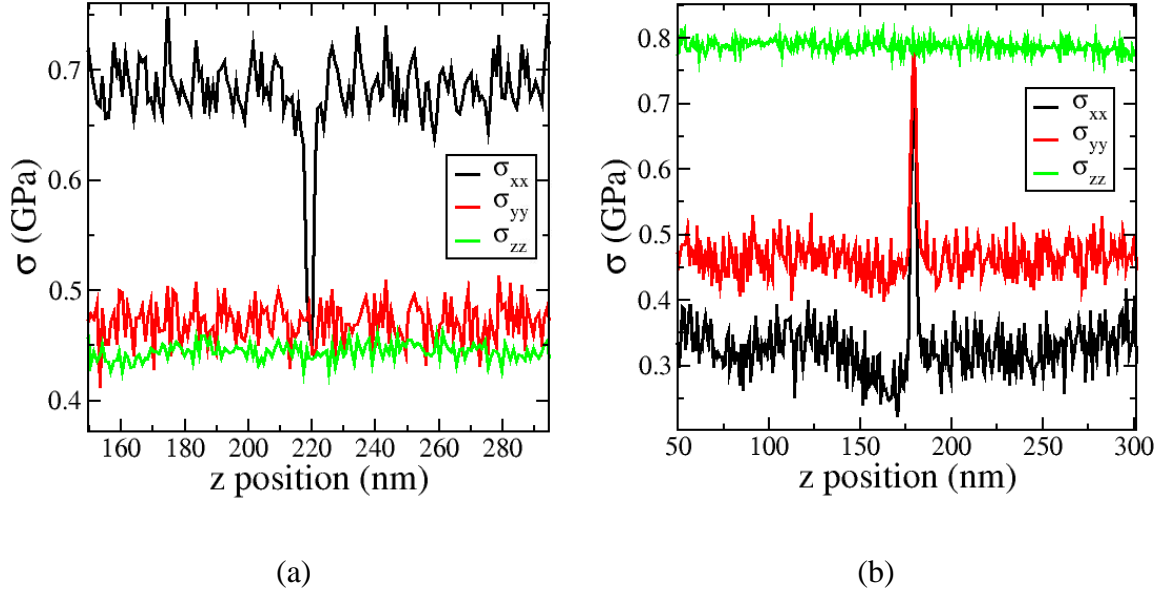


**Figure 4.7. The local normal stresses distribution along z direction (perpendicular to the shear band) in PSL tests under tensile loading once a shear band forms across the sample with  $\theta = 39^\circ$  in (a) and  $\theta = 57^\circ$  in (b).**

We directly examined the stress state of a shear band under uniaxial tensile loading in the PSL tests (note that similar observations have been made in compressive PSL tests). To assess the effect of the shear band angle, it was tuned by controlling the angle of perturbation within the range from 39 degrees to 57 degrees. Before the shear band nucleates and grows across the sample, the normal stress is uniform throughout the sample. As soon as an across-the-sample shear band forms, the HS state is attained in the running shear band as shown in Fig. 4.7. It is interesting to note that when the shear band angle is lower than 45 degrees in Fig. 4.7(a), the hydrostatic stress in the RSB is lower than the rest of material. This is different from the situation in the confined shear band at the crack tip<sup>195</sup>, which will be discussed in details later (section 4.2.8). When the shear band angle is higher than 45 degrees, the hydrostatic stress is elevated above the rest of material as in Fig. 4.7(b). The common feature in Fig. 4.7(a) and (b) is that  $\sigma_{zz}$  stay uniform inside and outside the shear band, thus maintaining mechanical equilibrium perpendicular to the shear band. Moreover,  $\sigma_{zz}$  is equal to the magnitude of the

hydrostatic stress, which dictates the value of  $\sigma_{xx}$  and  $\sigma_{yy}$  in the shear band. Importantly, the hydrostatic stress in the shear band can be easily calculated as,

$$\sigma_{hydrostatic} = \sigma_{zz} = \sigma_L \sin^2 \theta \quad (4.4)$$

Here the dynamical effect of shear band formation and associated elastic waves are neglected. From Eq. (4.4), the hydrostatic tensile stress inside the shear band sensitively depends on the shear band angle, which may contribute to the generally larger than 45 degrees tensile fracture angle observed in experiment<sup>212</sup>. For instance, once the shear band angle under uniaxial tension increases from 45 to 60 degrees<sup>212</sup>, the tensile hydrostatic stress in the shear band increases by 50%.

#### 4.2.4 Small-scale simulation in the mWA system

Small-scale simulation enables one to study the stress state in RSB under more general initial stress states. The initial stress state is set using Eq. (4.3). We set  $\sigma_L$  to be compressive (see Table 4.1) to achieve extensive shear loading without the complication of cavitation<sup>104</sup>. During the small-scale simulation, the system was kept in an NVE ensemble. Fig. 4.8 shows the stress distribution as a function of  $z$  positions (in the direction perpendicular to the shear band) with a spatial resolution of 1 nm. Prior to the formation of the shear band, the local stress distribution along the  $z$  direction is uniform with atomic fluctuation as shown in Fig. 4.8(a). Immediately after the shear band forms as shown in Fig. 4.8(b), the local normal stresses of  $\sigma_{xx}$ ,  $\sigma_{yy}$  and  $\sigma_{zz}$  in the shear band become equal to each other, indicating the shear band becomes liquid-like. Similar to the large-scale simulation,  $\sigma_{zz}$  is uniform across the sample even after the formation of the shear band. However, the shear band region exhibits differences in the  $\sigma_{xx}$  and  $\sigma_{yy}$  distributions compared to other regions.

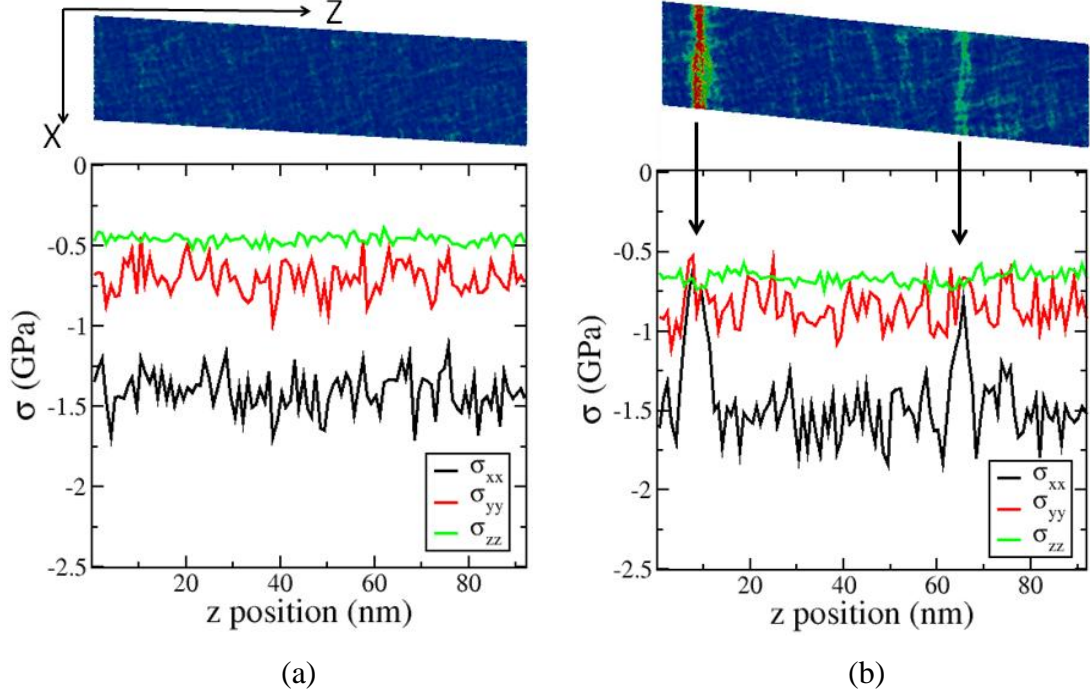


**Figure 4.8.** The deformation morphologies (colored by atomic shear strain, with blue corresponding to 0 strain and red corresponding to strain of 20% and above) and the corresponding local normal stresses distribution along the z direction before (a) and after (b) shear band formation. The applied shear strain is 6% and 8% in (a) and (b) respectively. The  $\theta$  parameter is set to be 0 degree. The local normal stresses become equal to each other at the location where the shear bands formed as indicated by the arrows.

To understand the robustness of the HS stress state inside the shear band, we then analyzed the local stress evolution of the shear band as a function of time. Particularly, how the HS stress state vary with respect to the applied shear flow. Here, the stress state is controlled by the  $\theta$  parameter using Eq. (4.3), ranging from 0 to 90 degrees. As shown in Fig. 4.9(a) to (d), the shear stress exhibits an overshoot and then drops to the shear flow stress, indicating shear band formation. Shortly after, the three normal stresses merge together, thus the HS stress state is achieved. In addition, we set  $\sigma_L$  to be tensile and also observed the HS stress state in the shear band. Therefore the shear band will be in an HS stress state independent of the initial normal stress state. The simulation results from the small-scale simulations show the HS stress state inside a shear band, consistent with the observations obtained from the large-scale PSL tests.

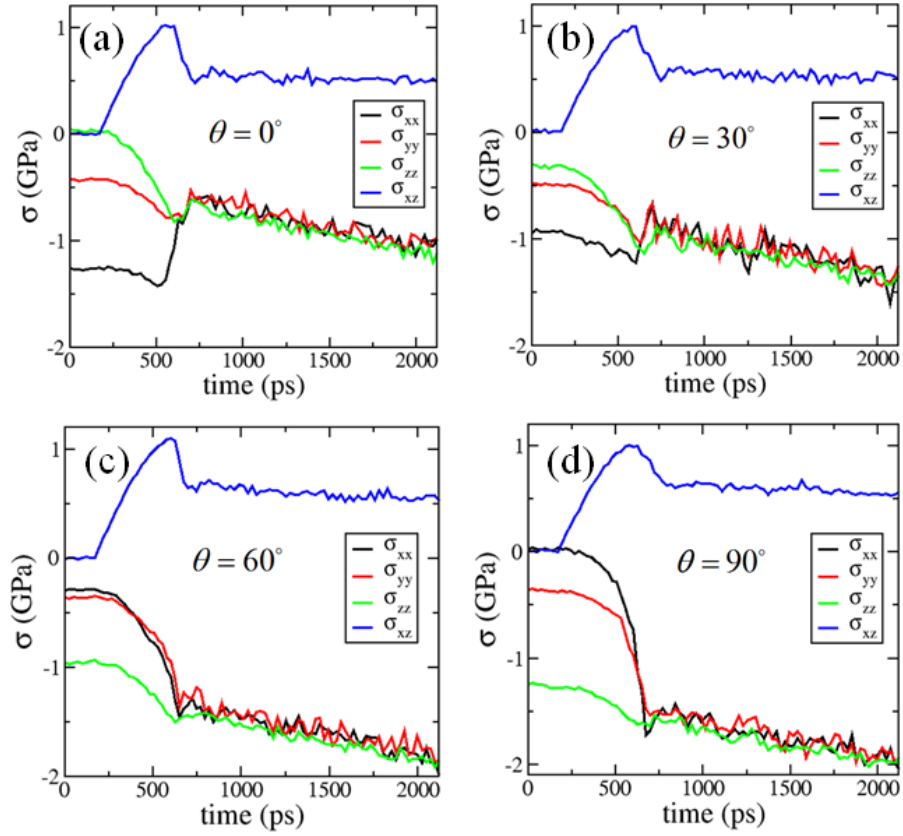


**Figure 4.9.** The evolution in time of the local stress at the location where the shear band forms in simulations under NVE ensemble with the parameter  $\theta$  set from  $0^\circ$  to  $90^\circ$  in (a) to (d). The local HS stress state was achieved when the shear bands forms, independent of  $\theta$ .

#### 4.2.5 The effect of temperature

To comprehend the HS stress state inside the shear band, one would immediately link to the local temperature rise inside the shear band. Both the small-scale and large-scale simulations are under NVE ensemble. Therefore, the temperature inside the shear band can rise as high as 200 K. It should be noted, however, such temperature is still much lower than the glass transition temperature, which is measured to be 680 K for the mWA system.

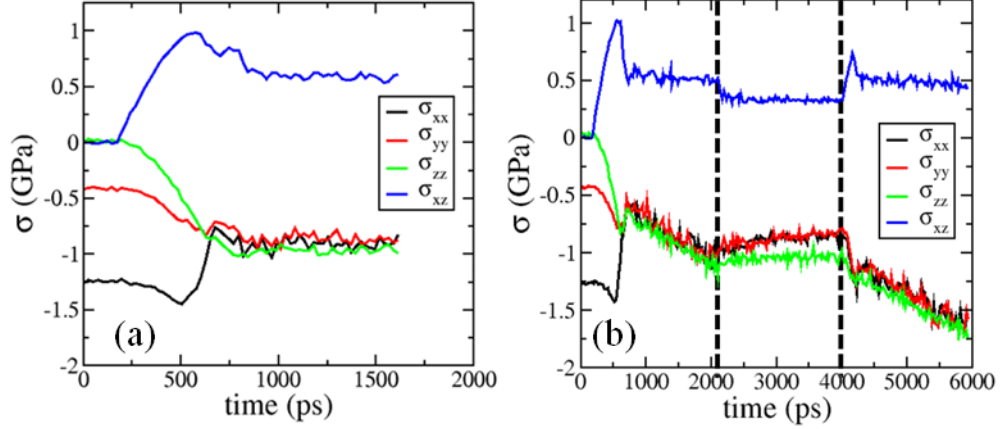


**Figure 4.10.** The evolution of the local stresses at the location where the shear band forms under the NVT ensemble with the temperature at 10 K. A representative result with the  $\theta$  parameter to be  $0^\circ$  is shown. (b). As a continuation of the tests in Fig. 4.9, relaxation without any deformation is conducted from 2.1 ns to 4 ns, as is indicated by dashed line. After 4 ns, shear deformation is resumed. A representative result with the  $\theta$  parameter to be  $0^\circ$  is shown.

To identify the effect of temperature on the stress state of the shear band, we repeated the small-scale simulation while keeping the average temperature of the whole system at 10 K in an NVT ensemble. We have also conducted simulations with local temperature controls where the peak temperature in the RSB is only around 20 K. The results are essentially the same. As shown in Fig. 4.10(a), the HS stress state is again attained in the RSB. The only difference here is that the compressive hydrostatic stress stays constant, instead of increases continuously due to an increasing temperature as shown in Fig. 4.9. Therefore, the HS stress state is not due to the temperature rise in the shear band.

#### 4.2.6 The effect of shear flow

To assess the effect of shear flow on the HS stress state in the shear band, we continued the small-scale simulation in Section 4.2.4 without shearing for 1.9 ns. As can be seen in Fig 4.10(b), the shear stress drops only slightly before leveling off, indicating that the shear band can sustain shear stress under zero strain rate. Without shear flow, the three normal stresses of  $\sigma_{xx}$ ,  $\sigma_{yy}$  and  $\sigma_{zz}$  begin to deviate from each other. After the

holding period, shear on the system resumes for another 2 ns. The shear stress of the system overcomes a yield stress, lower than the initial one, probably due to the combination of softer shear band and higher temperature. Then the system enters the flow state. The HS stress state again emerges in the shear band. This result suggests that the HS stress state results from the driven shear flow. Deviation from the HS stress state of the shear band is expected once the shear flow stops.

#### 4.2.7 The effect of different glass formers

We also conducted small-scale tests on the other six aforementioned glass formers: KA, WA, FeP, M-CuZr, S-CuZr and SW-Si. Representative results are shown in Fig. 4.11. Except in the FeP system and the SW-Si system, the HS stress state is achieved within the atomic fluctuation in the shear band for all the glass formers. It is interesting to note that although the atomic structure of shear bands of SW-Si is close to its liquid structure<sup>117,213</sup>, the deviation from HS state in the RSB of SW-Si indicates that subtle differences exist between RSBs and the liquid state in SW-Si.

In the Fe<sub>80</sub>P<sub>20</sub> glass,  $\sigma_{xx}$  and  $\sigma_{yy}$  elevate above  $\sigma_{zz}$  in the shear band. One feature of the Fe<sub>80</sub>P<sub>20</sub> model glass is that system exhibits strong phase segregation, which is in fact intended in the design of the force field<sup>138</sup>. Therefore exception in the FeP system might be related to the strong tendency for chemical ordering driven by phase segregation.

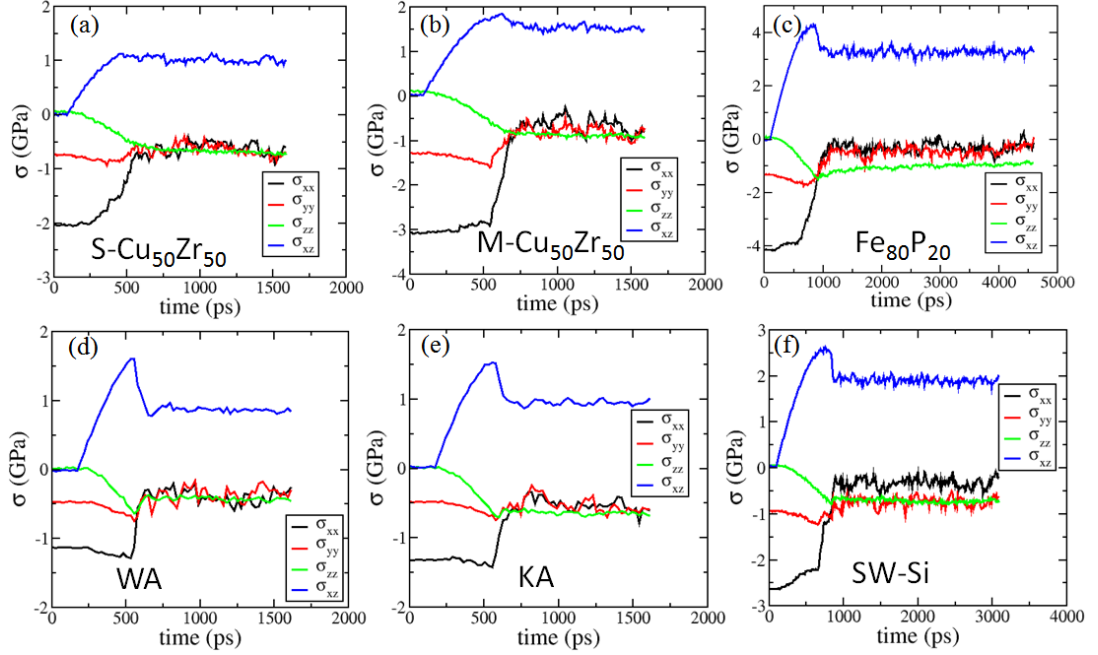


**Figure 4.11.** The evolution in time of the local stresses at the location where the shear band forms for the labeled force fields. The simulations are kept under the NVT ensemble with very low temperature (listed in Table 4.1). Representative results with the  $\theta$  parameter set to  $0^\circ$  are shown. The local HS stress state was achieved within atomic fluctuation in all these glasses when the shear band forms except in the FeP system and the SW-Si system.

Albeit serving as a metallic glass analog<sup>117</sup>, the SW-Si is in fact a covalent system that features a strong angular constraint that controls the rigidity of the local tetrahedral bonding angle<sup>139</sup>. The angular constraint can be tuned by one parameter  $\lambda$ <sup>130,214</sup>, which scales the energy penalty for bond angles deviating from 109 degrees. A larger  $\lambda$  corresponds to a stronger angular constraint or directionality in bonding. Therefore one can conveniently tune  $\lambda$  to test whether the angular constraint has any effect on the stress state in the RSB. For Si,  $\lambda$  is set to be 21 according to the original force field by Stillinger and Weber<sup>139</sup>. For a smaller  $\lambda$  equal to 18.75, the corresponding less-covalent solid can be considered as a hypothetical element intermediate between Ge and Sn<sup>214</sup>. Conversely, tuning  $\lambda$  up is qualitatively tuning silicon towards carbon. In the additional simulations, we modified  $\lambda$  to be 17 and 33. As shown in Fig. 4.12, for  $\lambda$  of 33, the local stress in the shear band  $\sigma_{xx}$  deviates from  $\sigma_{zz}$  even more than the SW Si shown in Fig. 4.11. However, for  $\lambda$  of 17, the HS state is attained in the shear band.

Thus, the force tuning method demonstrates that the deviation from HS stress state in the shear band of SW Si system is caused by the strong angular constraint or directionality in bonding.

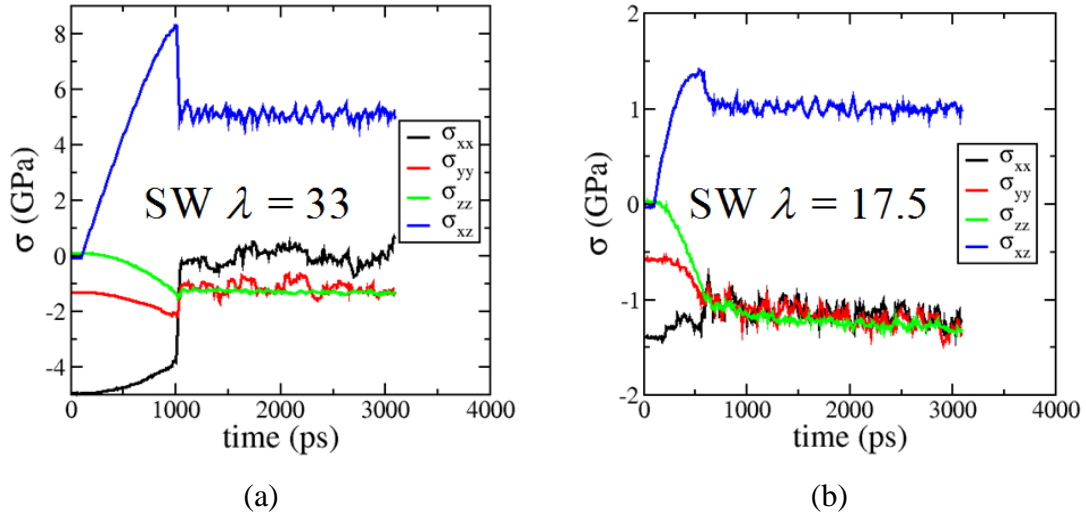


**Figure 4.12.** The evolution in time of the local stresses at the location where the shear band forms in simulations with the  $\theta$  parameter set to  $0^\circ$  for the SW-Si system with modified angular constraint. The simulations are kept under the NVT ensemble with the temperature at 1 K.

#### 4.2.8 The effect of plastic confinement

It's worth noting the possible differences between an across-the-sample RSB and a confined static shear band at the crack tip. For the former case, the magnitude of the hydrostatic stress is angle dependent, which is different from the shear band at the crack tip<sup>195</sup> where elevated level of hydrostatic stress was proposed to prevail based on plastic flow confinement<sup>215–217</sup> from conventional mechanics. It can be further seen that the HS stress state observed here in an RSB cannot be fully explained by plastic confinement. First, the plastic confinement can only elevate the hydrostatic stress, but cannot dictate the three normal stresses to be equal to each other. In addition, the plastic confinement cannot predict the magnitude of hydrostatic stress to be lowered with the angle of the across-the-sample shear band being smaller than 45 degrees as shown in Fig 4.7(a). Moreover, if the stress state is controlled by the plastic flow confinement, then the aspect

ratio of the shear band will have a strong effect on the magnitude of the hydrostatic stress in the shear band <sup>217</sup>. However, as in both the small-scale simulation and large-scale PSL simulation, we did not observe such aspect ratio effect. Therefore, the HS stress state in the across-the-sample RSB should be a result of atomic structural transformation <sup>51,52,60</sup> that is beyond the scope of conventional mechanics.

#### 4.2.9 Summary

We examined the local stress state of the across-the-sample RSB in seven different amorphous solids in MD simulations. Our findings suggest that the HS stress state in RSB might be universal to metallic glasses, but not for systems with a tendency to phase segregate or systems with high covalency. The HS stress state originates from the shear flow induced structural transformation (disorder) instead of elevated temperature, special initial stress state, or the plastic confinement effect. Such liquid feature of the stress state supports the notion that shear banding is like a shear-driven glass-to-liquid transition. An important insight can be obtained for RSBs: the magnitude of the hydrostatic stress in the RSB of metallic glasses can be calculated as  $\sigma_{zz}$ . In uniaxial tests, it is  $\sigma_L \sin^2 \theta$ , where  $\sigma_L$  is the magnitude of the uniaxial loading and  $\theta$  is the angle of the shear band to the loading direction.

## 5. Size Dependent Tensile Fracture via Shear Band Cavitation

Recently developed Pd-based and Zr-based metallic glasses<sup>16,17</sup> stand out as the most damage tolerant materials, with the combination of yield strength above 1.5 GPa, fracture toughness around  $150 \text{ MPa}\sqrt{\text{m}}$  and good ductility under compression and bending. Surprisingly, however, they possess nearly zero tensile ductility<sup>16,17</sup>. The combination of high toughness and extreme tensile brittleness poses an intriguing challenge in this field. This challenge turns out to be extremely difficult to tackle due to spatial and temporal limitations in both experiments and conventional atomic simulations<sup>127</sup>.

In this chapter, we aim to elucidate the “tough but brittle” puzzle via a novel large scale simulation method called perturbative static loading (PSL) method. As discussed in the preceding chapter, the properties of a running shear band are history independent, so we can use perturbations to facilitate shear band nucleation without changing the fracture behavior. With the PSL method, we effectively increase the simulation efficiency by 3 orders of magnitude. As a result, the dimensions of the sample size reach one micron.

The large scale atomic simulations unambiguously demonstrate that tensile fracture is caused by shear band cavitation. It is further revealed that the shear band cavitation is triggered by the critical thermomechanical states inside the shear band. Based on the simulations, we developed a simple model to understand that the size dependency of the tensile fracture of metallic glasses originates from size dependent thermomechanical evolution of the shear band. An analytical material index is derived to predict the tensile ductility of metallic glasses.

### 5.1 Introduction

Metallic glasses (MGs) have emerged as a promising candidate for the new generation of structural materials due to their high strength, corrosion resistance, among

---

Portions of this chapter previously appeared as: Luo, J. & Shi, Y. Tensile fracture of metallic glasses via shear band cavitation. *Acta Mater.* **82**, 483–490 (2015).

other merits<sup>20–22</sup>. However, bulk monolithic metallic glasses exhibit zero tensile ductility due to catastrophic failure along a primary shear band<sup>10,11</sup>. For instance, the recently developed Pd-based MG is among the strongest and toughest materials known, yet still fails catastrophically under uniaxial tension<sup>218</sup>. It is generally understood that a shear band initiates via structural softening (with negligible thermal softening<sup>51,58,60</sup>), then propagates and slips (accompanied with significant temperature rise<sup>10,56</sup>), until it transits into a crack via cavitation. The involvement of cavitation in tensile fracture can be inferred from fractographs of MGs under tension<sup>61,62</sup>, which is different from the scenario ahead of crack tips in bending tests of notched samples<sup>219,220</sup>, or compressive fracture<sup>58</sup>. Quantitative understanding of shear band cavitation is currently lacking, yet crucial to realize MG as practical structural materials.

Several models have been proposed to understand the failure modes of MGs, including the critical temperature rise<sup>56,58,79–81</sup> or thermal runaway<sup>82,83</sup> in the shear band, the critical shear band energy density<sup>26,59</sup>, and the critical shear off distance<sup>61,62,85</sup>. However, there is no direct examination of the above failure criteria in the case of tensile fracture of MGs, as the thermomechanical state of the shear band at the onset of fracture is extremely difficult to characterize in experiments<sup>40,127</sup>. The shear band features a spatial scale of nanometers<sup>39</sup>, evolves with a temporal scale of nanoseconds or shorter<sup>56</sup>, and often propagates deep beneath the surface. As a result, the temperature rise in shear bands was only inferred indirectly in bending<sup>56</sup> or compression<sup>84</sup>, not yet in tension. Moreover, there is no report on the local stress state of a shear band, let alone the stress state at the onset of failure. On the simulation side, a model MG sample under mode-III torsion has been studied, without fracture<sup>79</sup>. Simulations have also been conducted on fracture under hydrostatic tension or with a pre-existing crack<sup>194,195,221</sup> in MG systems. However, simulation on shear band-to-crack transition under uniaxial tension is still lacking. Such simulations are challenging as a large sample (estimated to be microns) is required for the shear band-to-crack transition. In addition, the experimental strain rates are orders of magnitude lower than those in typical molecular-level simulations.

In this study, we employed a uniaxial loading method termed perturbative static loading (PSL) to overcome the above spatial and temporal limitations in molecular

dynamics (MD) simulations. This chapter is organized as follows. Section 5.2 introduces the model glassy system, conventional uniaxial tension results, and the PSL method for large-scale simulation. Next, PSL tests are employed to show size-induced brittle fracture under uniaxial tension in Section 5.3.1. The shear band evolution and the critical cavitation states under uniaxial tension are described in Section 5.3.2. By comparison between large-scale uniaxial tension tests and small-scale simulations under more general loading conditions, the importance of shear flow to cavitation is demonstrated in Section 5.3.3. Based on the cavitation criterion observed in the large-scale simulations, an analytical model is developed to understand shear band-to-crack transition in Section 5.4. Concluding remarks are presented in Section 5.5.

## **5.2 Simulation methodology**

### **5.2.1 Conventional uniaxial tension test**

Conventional displacement-controlled uniaxial tension test was first carried out on a slab-shaped sample with dimensions of  $22(X) \times 2.7(Y) \times 90(Z) \text{ nm}^3$ . The glassy sample was cooled from a liquid isochorically from 2000 K to 10 K in 23 ns. The sample was subjected to displacement-controlled loading, with a strain rate of  $2 \times 10^7 \text{ s}^{-1}$ , by moving the two ends of the sample (serving as grips, with 1.3 nm in length) in the loading direction, while allowing unrestricted motion along transverse directions. The sample is under plane-strain conditions. It is apparent in Fig. 5.1 that a dominant shear band first forms, and then glides until the sample shear fractures. One can further measure the shear band angle, with respect to the loading direction, to be 51 degrees, and the thickness of the shear band to be about 6 nm. Both of these measurements will be used as input parameters for the following large-scale PSL simulations.

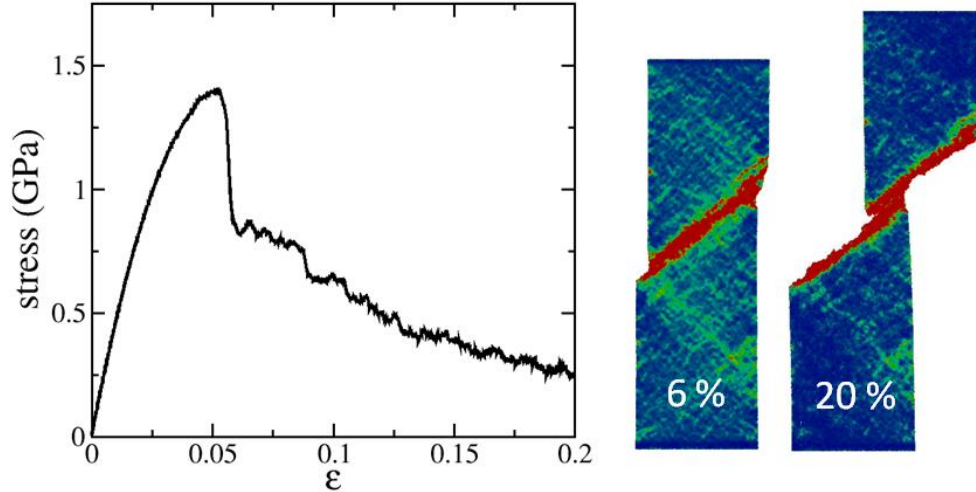


**Figure 5.1. Conventional uniaxial tension tests of an amorphous slab. The left pane shows the stress-strain curve. The right pane shows the atomic configurations at 6% and 20% strain. The atoms are colored according to the local shear strain from blue (0% strain) to red (20% strain). A dominant shear band is apparent, which is similar to the experiment [25].**

### 5.2.2 Perturbative static loading test

It should be noted that a conventional incremental loading test, as in the preceding section, usually leads to the formation of multiple shear bands in large samples, probably due to the extremely high strain rates. The presence of multiple shear bands undermines the sample length (the effective sample length per shear band), thus prevents the shear band-to-crack transition. In the PSL test, only one dominant shear band will form under zero strain rate loading, enabling the modeling of the shear band-to-crack transition in MG samples (up to 1 micron).

The essence of the PSL test is to facilitate the formation of a single cross-sample shear band under tensile loading, which subsequently glides under zero strain rate loading. The PSL test includes four steps. First, a glassy BLJ sample,  $22(X) \times 2.7(Y) \times 90(Z) \text{ nm}^3$  in size, was prepared by quenching a liquid isochorically

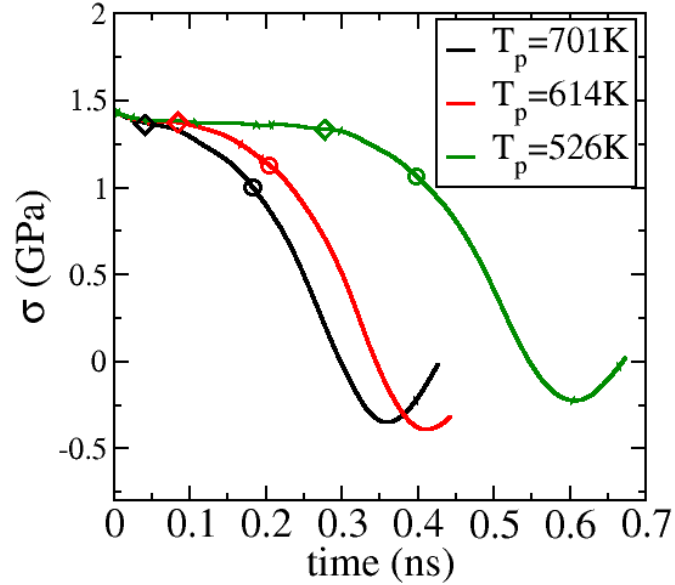


**Figure 5.2.** The tensile stress-time curves in PSL tests for samples with different perturbation temperature  $T_p$ . The pre-strain is 5.0 %. The sample length is 360 nm, just long enough for tensile fracture (as shown in Fig. 5.4). The diamond symbol in each curve indicates the formation of the across-sample shear band and the circle symbol indicates the moment the first cavity appears in the shear band. The initial stress plateau corresponds to the shear band initiation or nucleation. Lower values of  $T_p$  increase the stress plateau duration and delay the shear band initiation, but do not suppress the subsequent fracture behavior of the sample. Cavitation only takes about 0.15 ns (from the diamond symbol to the circle) for this sample, independent of the shear band nucleation time.

from 2000 K to 10 K in 23 ns. The glassy sample was subjected to plane strain uniaxial tensile loading (along Z-axis), with a strain rate of  $2.08 \times 10^8 s^{-1}$ , to pre-strains ranging from 3% to 5%. These pre-strains are within the elastic limit of the model sample (Fig. 5.1) and the experimental observations<sup>13,14</sup>. The second step is to generate a larger pre-strained sample with desired length and width by replicating the sample from the first step. Such replication will not lead to artificial periodicity due to the subsequent shear band formation. The sample aspect ratio was kept at 3:1, low enough to prevent the shape-induced brittleness<sup>177</sup>. Two free surfaces in the X-direction were introduced to permit sample gliding along the shear band. We have found that surface relaxation has minor effect on the shear band evolution. The third step is to generate a structurally perturbed band across the sample. A thin region (6-nm thick, 51 °tilted away from the loading direction, according to the conventional uniaxial tension test shown in Fig. 5.1)

was heated for 5 ps at a perturbation temperature  $T_p$  (details in Table 5.1), then relaxed at 10 K for another 5 ps. The rest of the sample was fixed during this step. Since the properties of the shear band are independent of its thermomechanical history<sup>60</sup>, this perturbation is expected to have little effect on the behavior of the shear band, which would later form. It can be seen in Fig. 5.2 that lower values of  $T_p$  delay the shear band initiation, but do not change the fracture behavior of the sample. In the last step, the pre-strained and perturbed MG sample was subjected to static loading by fixing the two ends of the sample (serving as grips, with 1.3 nm in length) in the loading direction, allowing unrestricted motion along transverse directions. Then the whole sample was kept in an NVE ensemble. Such applied static loading is equivalent to an ideal displacement-controlled uniaxial tension experiment with zero strain rate.

**Table 5.1. The perturbation temperature  $T_p$  for PSL tests with different pre-strains.  $T_p$  was chosen to shorten the shear band formation time under tension. As shown in Fig. 5.2, a lower  $T_p$  leads to longer time for shear band formation, but identical fracture behavior for a sample just long enough to cause fracture at 5 % pre-strain.**

Pre-strain	3%	3.5%	4%	4.5%	5%
$T_p$ (K)	1139	964	877	789	701

## 5.3 Size-induced ductile-to-brittle transition

### 5.3.1 Uniaxial tension test with PSL method

We first applied the PSL test on MG samples with lengths of 180, 260, and 360 nm under identical 5% pre-strains. As Fig. 5.3(c) shows, all three samples develop a dominant shear band and mechanically unload by gliding along the shear band. The amount of unloading (i.e., drop in the tensile stress  $\sigma$ , or increase of the shear off distance  $S$ , shown in Fig. 5.3a) increases with the sample length. The 180-nm-long

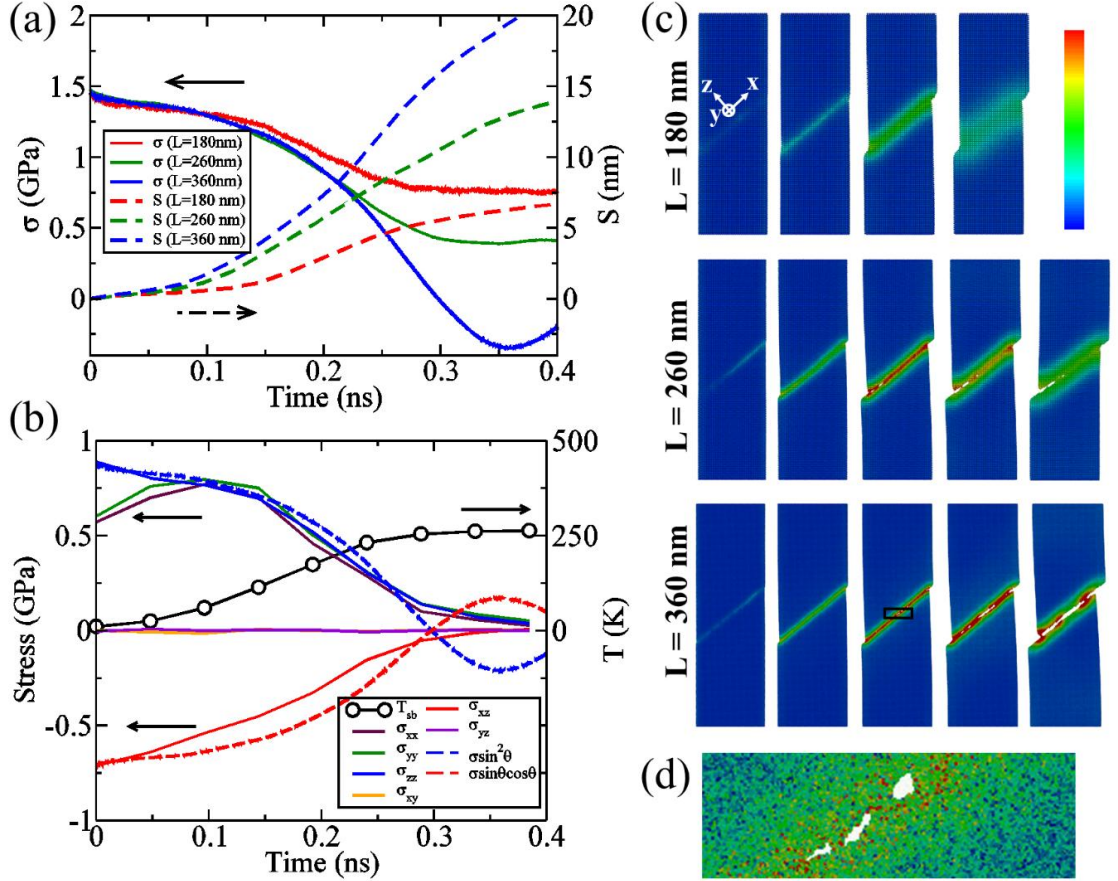


**Figure 5.3.** (a) The overall tensile stress  $\sigma$  (solid lines) and shear off distance  $S$  (dashed lines) during PSL tests on samples with lengths of 180, 260, 360 nm (red, green, blue), with 5% pre-strain. (b) The local stress (solid lines) and temperature (circles) inside the shear band during PSL tests on the 360-nm-long sample with 5% pre-strain. The shear-band-based coordination system is shown in pane (c). The local thermomechanical states were coarse-grained and averaged according to a shear band angle  $\theta = 51^\circ$ . The resolved tensile stress  $\sigma \sin^2 \theta$  (blue dashed line) and shear stress  $\sigma \sin \theta \cos \theta$  (red dashed line) were also shown. (c) The morphology evolution of the samples during PSL simulations. The color represents the local temperature (1.6 nm-grid-size): blue for 0 K; red for 175 K and above. (d) Zoom-in atomic view of the shear band cavitation (black box region in pane c).

sample retains half of the initial tensile stress without cavitation nor fracture (Fig. 5.3c), similar to the experimental observations<sup>25,26</sup>. The 360-nm-long sample cavitates (Fig. 5.3d) and then completely fractures. The 260-nm-long sample exhibits an intermediate behavior. Therefore, the samples exhibit a ductile to brittle transition (DTB) under otherwise identical conditions, as its length increases. The fracture surface of the 360-

nm-long sample exhibit nano-scale corrugations, echoing those from void formation in experiments<sup>61,62,222</sup>. These results demonstrate that brittle tensile fracture in MGs is triggered by shear band cavitation with strong size effect.

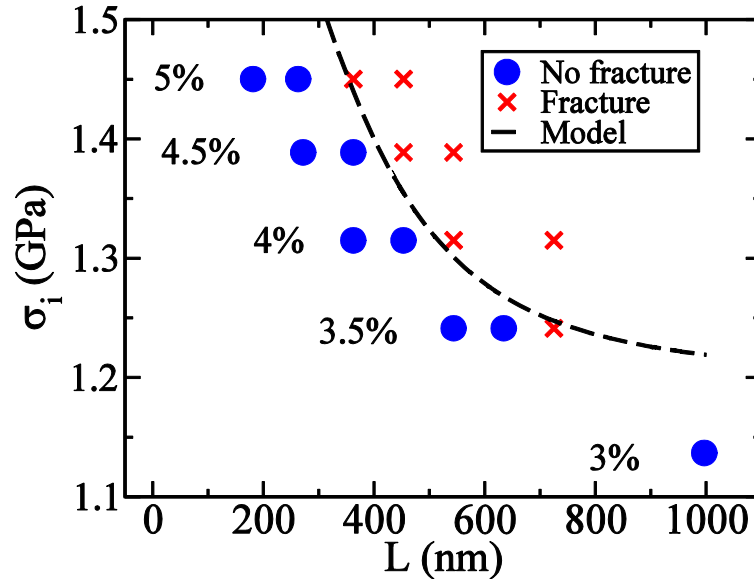


**Figure 5.4.** The PSL test results (red crosses denote fracture and blue circles denote no fracture) for samples with different lengths and the initial tensile stress. Pre-strains were also given. The black dashed line shows the critical cavitation condition predicted by Eq. (5.7), without any free parameter.

Experimentally, an MG sample can form a shear band at different tensile stress levels depending on its defects serving as stress-concentrators. To explore the effect of the initial loading stress, samples with different lengths were subjected to PSL tests under different pre-strains (equivalently, different initial tensile stress). Fig. 5.4 shows size-induced DTB transitions under different initial tensile stress. Importantly, the critical sample length for DTB transition increases as the pre-strain decreases. Multiple samples were tested to examine the sample-to-sample variation on the observed DTB transition. In addition, samples with different aspect ratio of 6:1 or 12:1 exhibit identical fracture behaviors as the original samples. Thus, the aspect ratio does not appear to affect the shear band-to-crack transition in MG, although the sample diameter might be important for shear band nucleation<sup>26,60</sup>.

### 5.3.2 Thermomechanical evolution of the shear band

To better understand the nature of the cavitation inside a shear band under uniaxial tension tests, we examined the thermomechanical (both temperature and stress state) evolution of the shear band. This is in contrast to previous studies focusing on the shear band temperature alone, without considering its stress state<sup>56,58,79–83</sup>. Fig. 5.3(b) shows how the local temperature and all components of the local stress tensor change during a PSL test. Note that we use "xyz" in lower cases for shear band coordinate shown in Fig. 5.3(c), and "XYZ" in upper cases for system coordinate. At the beginning of the PSL tests, the resisting shear stress  $\sigma_{zx}$  (shear-band-based coordination system shown on Fig. 5.3c) equals the resolved driving shear stress  $\sigma \sin \theta \cos \theta$ , where  $\sigma$  is the overall tensile stress of the sample,  $\theta$  is the shear band angle to the loading direction. After the shear band formation,  $\sigma_{zx}$  decreases below  $\sigma \sin \theta \cos \theta$  due to strain softening, resulting in a net driving force for shear gliding. On the other hand, the normal stress in the shear band  $\sigma_{zz}$  matches the resolved tensile stress  $\sigma \sin^2 \theta$  until fracture. Both  $\sigma_{xx}$  and  $\sigma_{yy}$  merge with  $\sigma_{zz}$ , as the shear band exhibits liquid-like behavior.  $\sigma_{xy}$  and  $\sigma_{yz}$  are close to zero during PSL tests. Thus, there are only two independent components in the stress tensor during shear band gliding, given  $\sigma_{xx} = \sigma_{yy} = \sigma_{zz}$  and  $\sigma_{zx} \neq \sigma_{xy} = \sigma_{yz} = 0$ . The temperature of the shear band can also be tracked as the sample glides (Fig. 5.3b), with heat-generation from plastic flow and heat-dissipation from conduction. In Fig. 5.3(c), the 180nm-long-sample eventually cools down once gliding stops. Note that even for the fractured samples, the temperature in the shear band is significantly lower than the glass transition temperature (~680 K for this system). Thus, reaching the glass transition temperature is not a necessary tensile fracture condition for MGs.

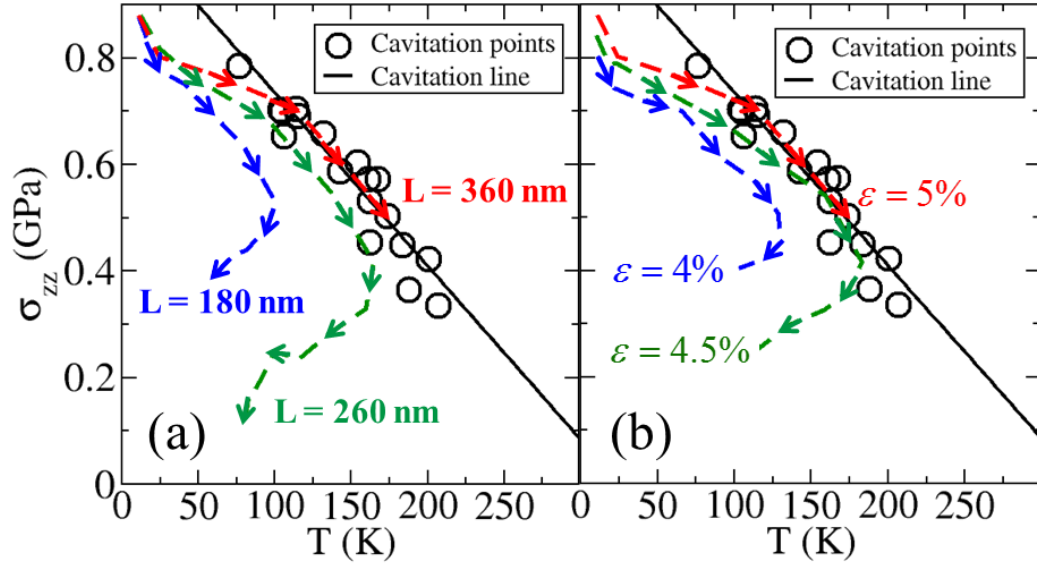


**Figure 5.5. Cavitation map in the normal stress ( $\sigma_{zz}$ ) and temperature ( $T$ ) domain with the thermomechanical state evolution of the shear band during PSL tests for: (a) samples with lengths of 180, 260, 360 nm at 5% initial pre-strain; (b) samples with a length of 360 nm at pre-strains of 4, 4.5, 5.0 %. The thermomechanical states are the average over the shear band with a width of 0.89 nm. The critical cavitation conditions (black circles) were obtained from all PSL tests ending with fracture, with a linear fit as the cavitation line.**

It is convenient to plot the shear band evolution in the  $\sigma_{zz} - T$  domain to examine the effects of the initial tensile stress (Fig. 5.5a) and the sample length (Fig. 5.5b). As the sample length increases under the same 5% pre-strain, or as the initial tensile stress increases with the same sample length, the shear band trajectories shift towards the high temperature/normal stress direction. Eventually, the sample (length of 360 nm and pre-strain of 5%) fractures, once its shear band trajectory reaches certain critical thermomechanical states for shear band cavitation. Here, the critical thermomechanical states for shear band cavitation (cavitation points, identified by the appearance of first cavity) were collected from all PSL test that exhibit brittle fracture. These cavitation points roughly fall on a straight line (the cavitation line, Fig. 5.5) in the  $\sigma_{zz} - T$  domain. The critical shear stress  $\sigma_{zx}$  at cavitation is shown in the next section to be linearly related to the critical normal stress  $\sigma_{zz}$ , justifying the choice of plotting cavitation line in

the  $\sigma_{zz} - T$  domain. Therefore, tensile fracture will occur once the thermomechanical trajectory of the shear band reaches the observed cavitation line.

It should be noted that, the thermomechanical state of the shear band evolves during the PSL test prior to cavitation, very much like a thermomechanical pulse, different from Ref. <sup>194</sup> in which the thermomechanical state is static. Another distinction from Ref. <sup>194</sup> is that the cavitation here occurs under high rate of shear flow, which drives the system far from equilibrium. Due to the dynamical nature of the cavitation problem and the presence of shear flow, it is assumed that whether cavitation occurs solely depends on the instantaneous thermomechanical state of the shear band, independent of its complex thermomechanical history. This is proper in the athermal limit, and is in contrast to the thermally activated static cavitation<sup>194</sup>, which is indeed history-dependent. Such simplification appears to work well, at least for the low temperature regime of interests here, as discussed in the next section.

### **5.3.3 Mapping the thermomechanical condition for shear band cavitation**

To comprehend the thermomechanical conditions for shear band cavitation under uniaxial tension, we focused on the shear band region and explored the critical cavitation states under well-defined loading conditions. To mimic a shear band, a smaller sample ( $8 \times 8 \times 8 \text{ nm}^3$ ) was chosen here, close to the shear band thickness. In addition, the sample was subjected to isothermal simple shear deformation of 200% strain prior to subsequent mechanical tests. The cavitation for this smaller sample was induced by isothermal hydrostatic tension with or without shear. Both the hydrostatic tension strain rate ( $\dot{\epsilon}$ )

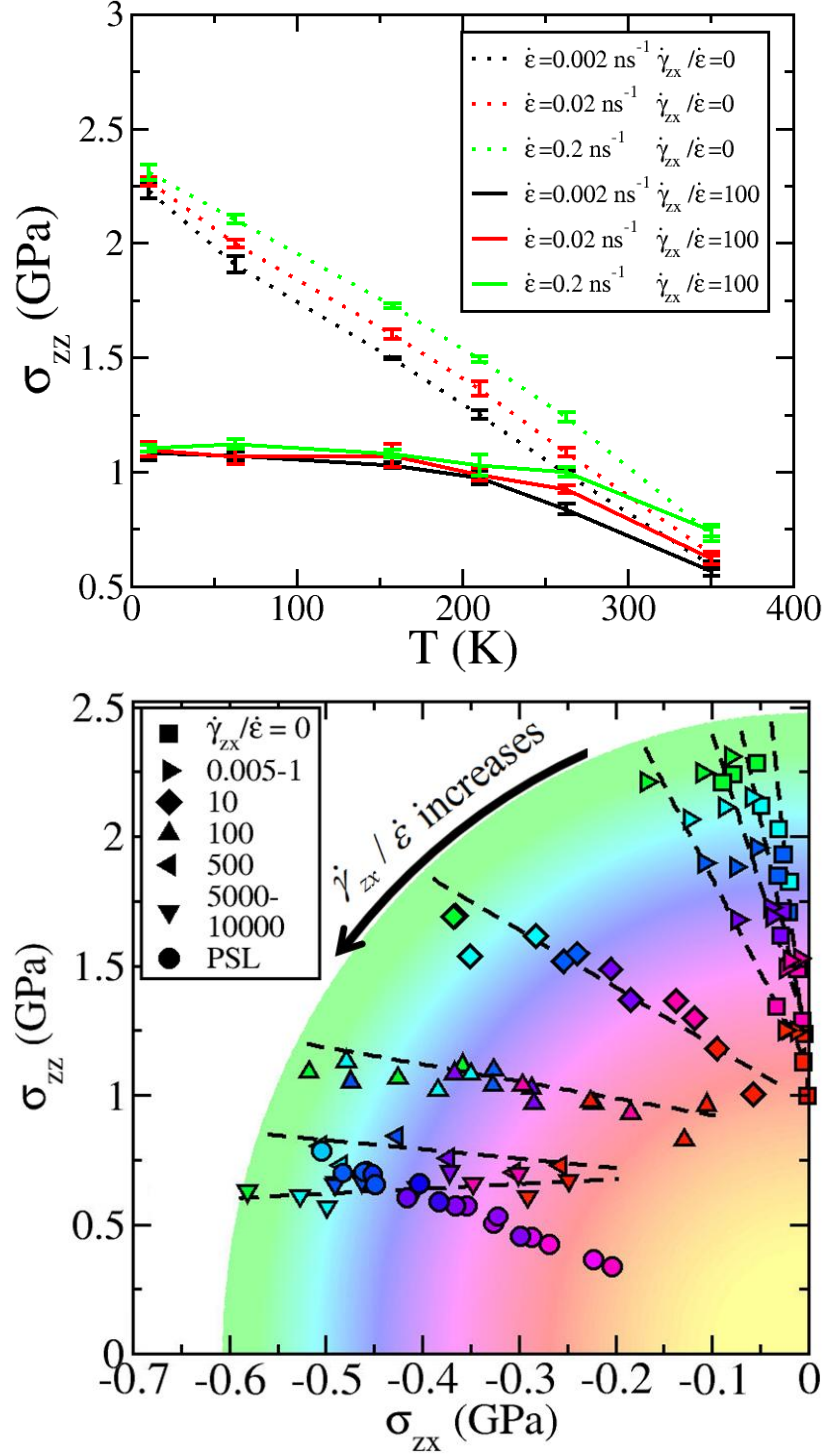


Figure 5.6. (a) The critical thermomechanical states for cavitation were mapped in the  $\sigma_{zz} - T$  domain from small-scale simulations with (solid lines) and without shear (broken lines). The error bar is calculated based on the results of five independent samples. In the label,  $\dot{\epsilon}$  and  $\dot{\gamma}_{zx}$  represent the hydrostatic tension strain rate and the shear strain rate. The cavitation stress decreases almost linearly

with increasing temperature under pure hydrostatic tension. With shear flow, the cavitation stress at given temperature decreases dramatically with increasing  $\dot{\gamma}_{zx} / \dot{\epsilon}$ . (b) The critical thermomechanical states for cavitation (squares for hydrostatic tension tests; triangles and diamonds for hydrostatic tension with shear; circles for PSL tests) were mapped in the  $\sigma_{zz} - \sigma_{zx} - T$  domain for more values of  $\dot{\gamma}_{zx} / \dot{\epsilon}$ . The symbols were colored by temperature (green represents 0 K and yellow represents 328 K), with a color contour guiding the eye. The strain rate ratio  $\dot{\gamma}_{zx} / \dot{\epsilon}$  is given in the legend (groups of points with the same  $\dot{\gamma}_{zx} / \dot{\epsilon}$  are denoted by the dashed lines).

and the shear strain rate ( $\dot{\gamma}_{zx}$ ) were kept constant. The involvement of shear is controlled by  $\dot{\gamma}_{zx} / \dot{\epsilon}$ . Here, the stress-state of the sample under hydrostatic tension with shear is very similar to the stress-state of a shear band during a PSL test:  $\sigma_{xx} = \sigma_{yy} = \sigma_{zz}$  and  $\sigma_{zx} \neq \sigma_{xy} = \sigma_{yz} = 0$ . The cavitation point is identified as the thermomechanical state reaching the maximum  $\sigma_{zz}$ , prior to cavitation induced stress drop. As shown in Fig. 5.6 (a), we can see that as the relative strain rate ratio  $\dot{\gamma}_{zx} / \dot{\epsilon}$  increases from 0 (hydrostatic tension without shear) to 100 (hydrostatic tension with shear), the cavitation line is dramatically lowered. Importantly, under the same relative shear strain rate ratio of  $\dot{\gamma}_{zx} / \dot{\epsilon} = 100$ , even as the loading rate  $\dot{\epsilon}$  decreases from  $0.2 \text{ ns}^{-1}$  to  $0.002 \text{ ns}^{-1}$  (thus, the loading timescale increases from 0.1 ns to 10 ns), the three cavitation lines overlap at the low temperature regime (below 200 K, similar to the temperature range observed in PSL tests as in Figure 5.5). For higher temperatures, there appears to be a time-dependency, similar to the hydrostatic loading without shear flow. Thus, the high rate shear flow drives the system far from equilibrium and leads to time-independent cavitation behavior, different from time-dependent behavior expected from a thermal activation picture<sup>194</sup>.

The critical thermomechanical states for shear band cavitation form a surface when presented in the domain of  $\sigma_{zz} - \sigma_{zx} - T$ . This is somewhat analogous to the thermomechanical conditions for stress-induced glass transition<sup>198</sup>. The first trend of Fig. 5.6 (b) is that, under the same temperature, the critical  $\sigma_{zz}$  and  $\sigma_{zx}$  fall on an elliptical circle, in line with recent experimental and theoretical studies<sup>223,224</sup>. As the temperature

increases, the circles shrink towards the zero-stress origin. The second trend in Fig. 5.6 (b) is that, for the same  $\dot{\gamma}_{zx} / \dot{\epsilon}$ , the critical  $\sigma_{zz}$  and  $\sigma_{zx}$  are almost linearly correlated. As  $\dot{\gamma}_{zx} / \dot{\epsilon}$  increases, the critical  $\sigma_{zz}$  and  $\sigma_{zx}$  sweep from the right-most line (hydrostatic tension tests without shear) to bottom-left lines (tests with high  $\dot{\gamma}_{zx} / \dot{\epsilon}$  ratio). The critical cavitation states in PSL tests shown on Fig. 5.6 (b) fall on a straight line, the projection of which on the  $\sigma_{zz} - T$  domain forms the cavitation line in Fig. 5.5. Moreover, the cavitation states in PSL tests are consistent with small samples with high  $\dot{\gamma}_{zx} / \dot{\epsilon}$ .

These results reveal that shear band cavitation is "shear driven", which is beyond the plastic confinement effect<sup>195</sup> and is different from the "thermally activated" cavitation under static hydrostatic loading<sup>194</sup>. Such shear induced instability, as was also suggested in a coarse-grained model<sup>225,226</sup>, might be generally relevant for liquids and all glassy materials.

#### 5.4 A thermomechanical model for shear band-to-crack transition

Lastly, we developed a thermomechanical model to describe the size-dependent shear band-to-crack transition. To simplify the analytical derivation of the shear band evolution during gliding, it is assumed that: (1) the mechanical equilibrium is maintained in the direction perpendicular to the shear band direction, thus  $\sigma_{zz} = \sigma \sin^2 \theta$ ; (2) the acceleration of the shear band gliding is a constant as,

$$\ddot{S} = (\sigma_i \sin \theta \cos \theta - \tau_f) / \rho d, \quad (5.3)$$

which is the difference between the driving resolved shear stress ( $\sigma_i$  is the initial uniaxial loading stress) and a constant frictional shear flow stress inside the shear band ( $\tau_f$ ), over a constant areal inertia term  $\rho d$  ( $\rho$  is the sample density,  $d$  denotes an effective length scale for this areal inertia). Only material near the shear band is accelerated as the gliding speed is very high (Fig. 5.3). This is different from the rigid-body gliding assumption in compression<sup>58</sup>. Given zero initial gliding speed, we have

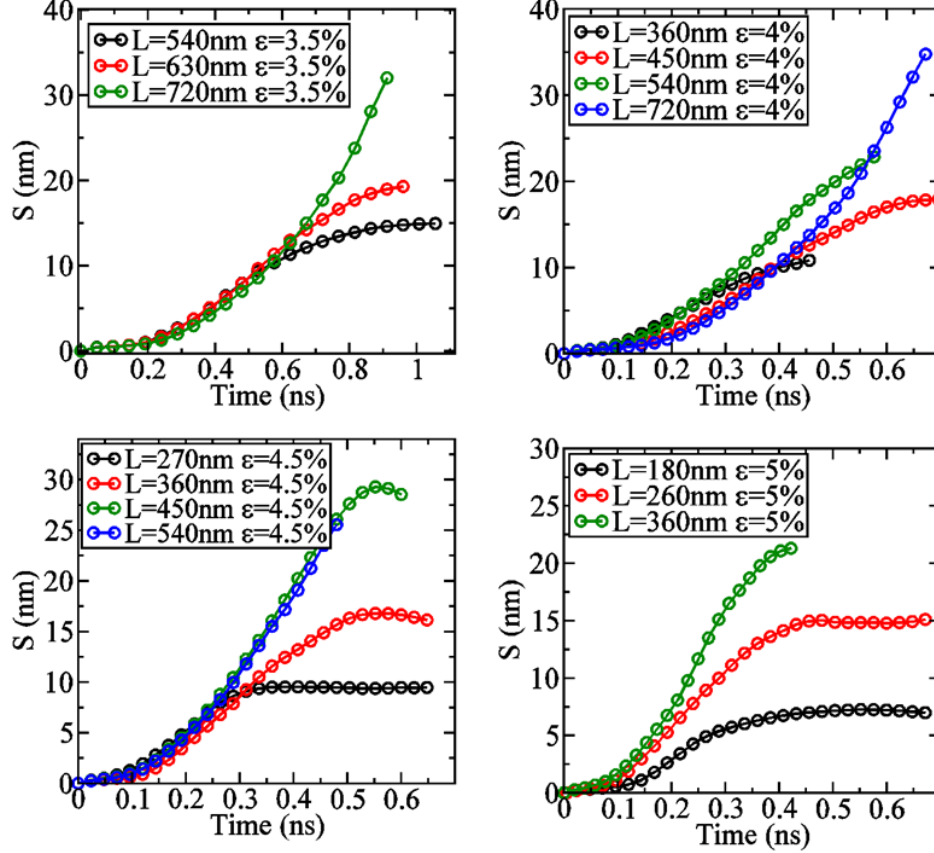


**Figure 5.7. Gliding distance ( $S$ ) as a function of time in PSL tests for samples with various lengths and pre-strains. The sliding starts with a parabolic increase in the gliding distance, almost independent of the sample length. For instance, at the 4% pre-strain (top-right pane), the  $S$ - $t$  curves overlap very well once the curves are shifted horizontally accounting for differences in time when gliding begins. The only exception is the shortest sample with the highest pre-strain. Gliding velocity ( $\dot{S}$ ) can be calculated straightforwardly, from which the initial gliding acceleration ( $\ddot{S}$ ) can be obtained as shown in Fig. 5.8.**

$\dot{S} = \ddot{S} \cdot t$  and  $S = \frac{1}{2} \ddot{S} \cdot t^2$ . Fig. 5.7 shows that  $S$  increases parabolically at the beginning of gliding, consistent with our constant acceleration assumption. Another observation from Fig. 5.7 is that, under the same pre-strain, the curvature of the curves almost overlap for samples with different length (except for the shortest sample with the highest pre-strain). Fig. 5.8 shows  $\ddot{S}$  is indeed linearly dependent on  $\sigma_t \sin \theta \cos \theta$ , not on the sample length. From fitting, one can obtain  $\tau_f = 0.59$  GPa and  $d = 31$  nm.

According to Duhamel<sup>58</sup>, the temperature rise in the shear band after time  $t$  is,

$$\Delta T(t) = \frac{1}{2\rho c_p \sqrt{\pi\alpha}} \int_0^t \frac{f(t-\tau)}{\sqrt{\tau}} d\tau, \quad (5.4)$$

Here,  $c_p$  is the specific heat capacity.  $\alpha$  is the thermal diffusivity.  $f(t)$  is the time-dependent heat flux  $f(t) = \tau_f \dot{S}$ . On the other hand, the instantaneous tensile stress of the sample ( $\sigma$ ) can be written as,

$$\sigma = \sigma_i - \frac{S \cos \theta}{L} E, \quad (5.5)$$

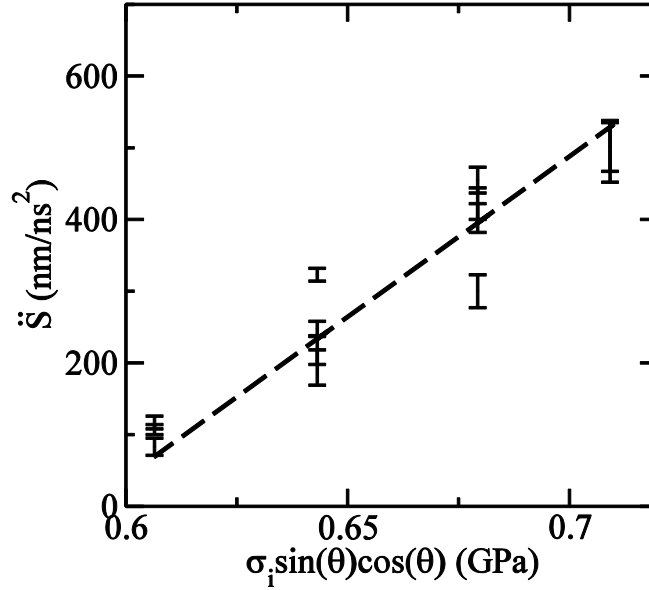


**Figure 5.8. The initial acceleration ( $\ddot{S}$ ) in PSL tests as a function of the initial resolved shear stress ( $\sigma_i \sin \theta \cos \theta$ ). All PSL data (data shown in Fig. 5.7) is included except for the shortest sample with the highest pre-strain. The linear fitting provides  $\tau_f = 0.59$  GPa and  $d = 31$  nm according to Eq. (5.3), with  $\rho = 7142$  kg/m<sup>3</sup>.**

due to elastic unloading.  $L$  is the sample length.  $E$  is the Young's modulus. Combining the expressions for  $\sigma$  and  $\Delta T$ , one can obtain  $T$  (the initial temperature is 10K, thus  $T \approx \Delta T$ ) as a function of  $\sigma$  or  $\sigma_{zz} = \sigma \sin^2 \theta$ ,

$$T = \frac{2^{7/4} \tau_f \sec^{3/4} \theta}{3\sqrt{\pi\alpha} c_p d^{1/4} \rho^{5/4} E^{3/4}} L^{3/4} (\sigma_i \cos \theta \sin \theta - \tau_f)^{1/4} \left( \sigma_i - \frac{\sigma_{zz}}{\sin^2 \theta} \right)^{3/4} \quad (5.6)$$

The cavitation line (Fig. 5.5) can be written as  $\sigma_{zz} = \sigma_{zz,0} \left(1 - \frac{T}{T_c}\right)$ , with  $\sigma_{zz,0} = 1.06$  GPa, and  $T_c = 326K$ , from linear fitting. Thus, the minimal initial tensile stress for cavitation, at the critical condition that Eq. (5.6) gets a tangent to the cavitation line, can be obtained as,

$$\sigma_i^{cavitation} = \frac{\sigma_0 L_0^3 + \sigma_f L^3}{L_0^3 + L^3} \quad (5.7)$$

Here,  $\sigma_0 = \frac{\sigma_{zz,0}}{\sin^2 \theta}$  and  $\sigma_f = \frac{\tau_f}{\sin \theta \cos \theta}$ , calculated as 1.77 GPa and 1.2 GPa, respectively. In addition,  $L_0$  represents a length scale of shear band-to-crack transition (326 nm for the model glass), with the expression as,

$$L_0 = \left( \frac{6\pi^2 c_p^4 T_c^4 E^3 \alpha^2 \rho^5 d}{\sigma_0^4 \sigma_f^4 \sin^5 \theta \cos^2 \theta} \right)^{1/3}, \quad (5.8)$$

**Table 5.2. The material properties for the BLJ glass in the simulation and the  $\text{Cu}_{46}\text{Zr}_{46}\text{Al}_8$  glass in experiments.**

	$\sigma_0$	$\sigma_f$	$T_g$	$d$	$\rho$	$\alpha$	$c_p$	$E$	$\theta$
SI units	GPa	GPa	K	nm	kg/m <sup>3</sup>	m <sup>2</sup> /s	J/kg/K	GPa	degree
$\text{Cu}_{46}\text{Zr}_{46}\text{Al}_8$	3.8 <sup>a</sup>	1.64 <sup>b</sup>	731 <sup>b</sup>	31	7100 <sup>b</sup>	2.3E-6 <sup>b</sup>	391 <sup>b</sup>	89 <sup>c</sup>	55 <sup>d</sup>
BLJ	1.77 <sup>e</sup>	1.20 <sup>f</sup>	701 <sup>g</sup>	31 <sup>f</sup>	7142 <sup>g</sup>	4.1E-7 <sup>g</sup>	358 <sup>g</sup>	42 <sup>h</sup>	51 <sup>i</sup>

<sup>a</sup> Estimated from the highest fracture stress of nanometer-sized  $\text{Cu}_{49}\text{Zr}_{51}$  from Ref.<sup>13</sup>

<sup>b</sup> Taken from Ref.<sup>81</sup>

<sup>c</sup> Taken from Ref.<sup>227</sup>

<sup>d</sup> Estimated from the shear band angle of  $\text{Cu}_{49}\text{Zr}_{51}$  from Ref.<sup>36</sup>

<sup>e</sup> Measured from fitting the cavitation line in PSL tests in Fig. 5.5.

<sup>f</sup> Measured in Fig.5.8.

<sup>g</sup> Measured from independent MD simulations using BLJ force field.

<sup>h</sup> The effective Young's modulus is  $E/(1-\nu^2)$ , under the conditions of plane strain in Y-direction and with free X-surfaces. Young's modulus  $E$  is 36.9GPa. The Poisson's ratio  $\nu$  is 0.36.

<sup>i</sup> Measured in Fig. 5.1.

The critical initial tensile stress for cavitation decreases from  $\sigma_0$  (critical tensile stress for zero length) to  $\sigma_f$  (critical tensile stress for infinite length), as  $L$  increases. Eq. (5.7) delineates the necessary fracture stress with given sample size in Fig. 5.4 very well. For critical cavitation, the time of slipping to reach the cavitation line can be considered a time scale as,

$$t_0 = \frac{L^2}{\pi\alpha} \left( \frac{\sigma_0 \sigma_f}{\rho c_p T_c E} \sin \theta \right)^2, \quad (5.9)$$

which is 0.2 ns for the BLJ system. Using  $\text{Cu}_{46}\text{Zr}_{46}\text{Al}_8$  as an example (material properties are listed in Table 5.2) and assuming  $d$  to be 31 nm ( $L_0$  weakly depends on  $d$ , while  $t_0$  is independent of  $d$ ), we estimated  $L_0$  to be 1.65 microns and  $t_0$  to be 0.3 ns. On a final note, the size-dependent tensile stress for shear band cavitation is a necessary but not sufficient condition for brittle tensile fracture, as shear band nucleation and propagation may require higher stresses.

## 5.5 Summary

In conclusion, the tensile fracture of MGs triggered by cavitation inside a slipping shear band was studied in novel large scale atomic simulations. The critical thermomechanical states for shear band cavitation were obtained. A previously overlooked shear flow weakening mechanism is found to have significant impact on the tensile fracture in the shear band of metallic glasses. Based on our simulation results, an analytical mechanistic model is proposed to rationalize the size dependent tensile fracture and is in agreement with the simulation. The model is useful as a guide to select or design ductile metallic glass system with very long length scale for shear band-to-crack transition, suppressing size-induced brittle tensile fracture.

## 6. Cavitation Map - A Concurrent Multiscale Simulation Study

Although brittle tensile fracture is almost a universal behavior among metallic glasses in experiments, it is only reported in atomic simulations with a very limited selection of force fields (i.e. the mWA system<sup>104</sup> and a FeP system<sup>195</sup>). Size limitation in atomic simulations is one of the reason that brittle tensile fracture is rarely observed in atomic simulations. To understand which force field can capture the size dependent brittle tensile fracture and why, we need to simulate metallic glass samples with sizes beyond micron-scale. To this end, we designed a novel concurrent multi-scale simulation method to examine the shear band evolution in macroscopic samples. The link between covalency in bonding and the tendency of brittle fracture emerges in the simulations. Based on the simulation results, we proposed a general method in the cavitation map to assess whether size dependent brittle tensile fracture can be simulated by a given force field or not.

### 6.1 Introduction

Size dependency is a very important feature of the tensile brittleness of metallic glasses<sup>25,26,59</sup>, but remains very challenging for atomic simulations. Although the size dependent tensile fracture in the submicron regime is observed in direct atomic simulation<sup>104</sup>, full MD simulation on the fracture process in samples with sizes beyond micron scale is still very difficult to realize. Due to such size limitation, there are still puzzles regarding the available atomic simulations. One outstanding question is why cavitation under uniaxial tension is observed only in model glasses simulated by FeP EAM<sup>195</sup> or modified binary Lennard Jones (BLJ) force fields<sup>104</sup> but absent in the Wahnstrom BLJ force field<sup>124</sup> and two CuZr EAM force fields<sup>79,221</sup> until very high hydrostatic stress or strain (not accessible in the shear bands under uniaxial tension) is imposed on the system<sup>194</sup>. For the original BLJ potential and the two CuZr EAM potentials, how large of a sample is required to drive the shear band to fracture under uniaxial tension?

To answer this question, we designed a concurrent multi-scale simulation technique to model uniaxial tension test on metallic glass samples with size up to macroscopic

levels. The size dependent shear band evolution in the multi-scale simulation confirms the speculation that there is an upper limit for the temperature that can be approached in the shear band<sup>79</sup>. The relative magnitude of the cavitation stress under the highest temperature and the resolved normal stress at yield point determines whether the sample will have size dependent tensile fracture via shear band cavitation. According to this criterion, we conclude that under uniaxial tension, cavities will not be able to nucleate in the shear band in the samples modeled by the CuZr EAM potentials and the original BLJ potential, no matter how large the sample size is. Implications on the effect of bonding and the generic potential form on tensile fracture via shear band cavitation will be discussed in the end.

## 6.2 Multi-scale simulation setup

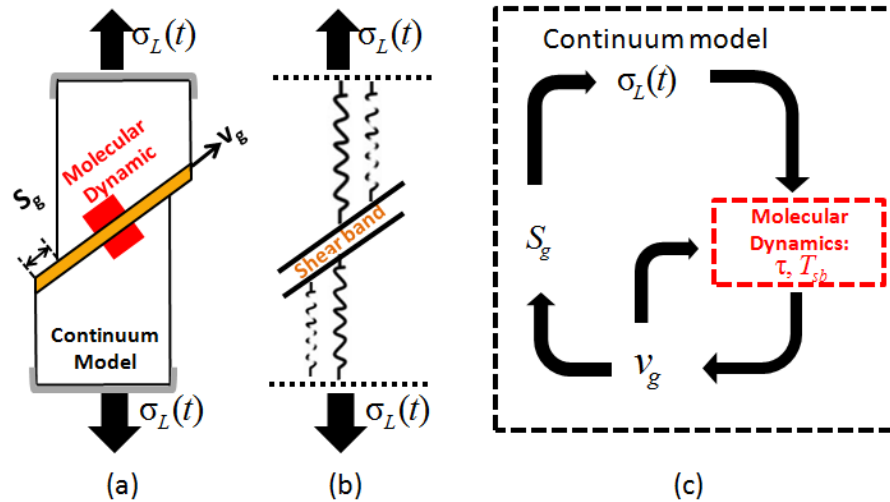


**Figure 6.1. Illustration of the plastic loading in the multi-scale simulation strategy. (a) The whole sample is under the tensile loading stress  $\sigma_L$  imposed by the continuum model. Yellow region represents the shear band. Red region is the small portion treated in MD simulation. The upper part of the sample glides along the shear band with a speed  $v_g(t)$  relative to the lower part. The gliding distance along the shear band is  $S_g(t)$ . (b) An “spring-shear band-spring” composite as an analogy to (a). (c) The flow chart of the multi-scale simulation during the plastic loading.**

The multi-scale simulation strategy is to use MD simulation to capture the detailed deformation (especially the potential cavitation process) in the shear band and use continuum model to simulate the elastic response of the rest of the sample under displacement controlled uniaxial tension test as illustrated in Fig. 6.1(a) and (b). The embedded MD simulation provides the real time shear off distance, shear resistance and temperature in the shear band, and the continuum model feeds the MD simulation with the real time loading, strain rate and temperature boundary conditions, as is illustrated in the control loop in Fig. 6.1(c). In the multi-scale simulation method, the time consuming procedure is the MD simulation. However, since we only simulate a tiny portion of the sample with atomic details, the multi-scale simulation allows significant speed-up and therefore permits simulation on samples up to 100 microns.

### 6.2.1 Elastic loading

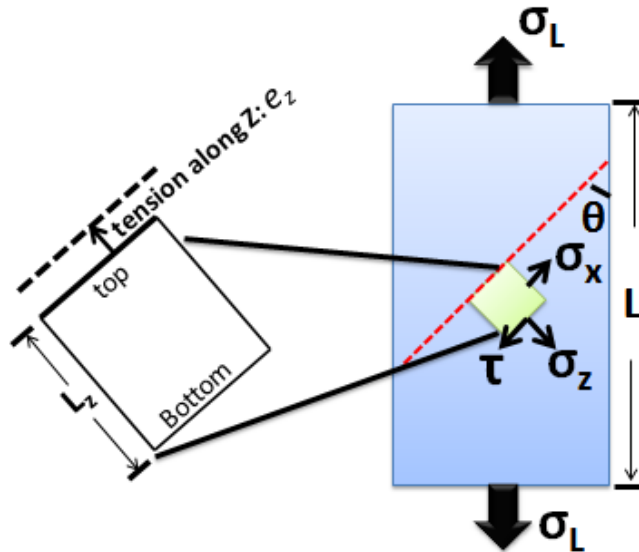


**Figure 6.2. Stress and strain analysis during elastic loading before the shear band forms in the light green small slab in MD simulation. The red dash line indicate the orientation of the to-be-formed shear band.**

The whole loading process starts with elastic loading. During the elastic loading, we assume the tensile loading strain rate imposed on the whole sample is  $e_L$  under plain strain condition (thickness doesn't change) to mimic a thick sample. The stress state of

the small slab within the whole sample is illustrated in Fig. 6.2. We can relate the normal stresses ( $\sigma_x$  and  $\sigma_z$ ) and shear stress ( $\tau$ ) in the shear band to the loading stress  $\sigma_L$  by

$$\sigma_z = \sigma_L \sin^2 \theta \quad (6.1)$$

$$\sigma_x = \sigma_L \cos^2 \theta \quad (6.2)$$

$$\tau = \sigma_L \sin \theta \cos \theta \quad (6.3)$$

$\theta$  is the angle between the to-be-formed shear band and the loading direction. We can also relate the loading strain  $\varepsilon_L$  or loading strain rate  $e_L$  of the whole sample to the tensile strain  $\varepsilon_z$  or tensile strain rate  $e_z$  of the small slab. As shown in Fig. 6.2, the horizontal contraction strain rate is  $\frac{ve_L}{1-v}$  due to Poisson's effect. The velocity of the top of the slab relative to the bottom along  $z$  direction is thus  $\frac{L_z \sin \theta}{L} L e_L \sin \theta - \frac{L_z \cos \theta}{L} L e_L \frac{v}{1-v} \cos \theta$ . Divided by  $L_z$ , we get the tensile strain rate  $e_z$  along  $Z$  direction in the MD simulation as

$$e_z = (\sin^2 \theta - \cos^2 \theta \frac{v}{1-v}) e_L \quad (6.4)$$

Simultaneously we control  $\sigma_x$  and  $\tau_e$  (the shear stress during the elastic loading) according to:

$$\sigma_x = \sigma_z \cot^2 \theta \quad (6.5)$$

$$\tau_e = \sigma_z \cot \theta \quad (6.6)$$

So at any time during the elastic loading, the stress state of the small sample can be matched to a corresponding portion of the whole sample. In simulation, we record  $\varepsilon_z$  and  $\sigma_z$ . By Eq. (6.1) and (6.4), we can get the stress strain curve  $\varepsilon_L \sim \sigma_L$  of the whole sample.

## 6.2.2 Plastic loading

The elastic loading ends and the plastic loading begins when a shear band initiates across the sample in the MD simulation. Here we assume only one shear band forms for the whole sample. As almost all the plastic strain is localized in the shear band during

plastic loading, the rest of the sample is therefore simplified as two elastic springs, which is illustrated in Fig. 6.1 (b). Then the normal stresses in the MD simulations can be synchronized by the spring with the loading stress in the continuum model in real time. We ignore the elastic wave propagation observed in full atomic simulations<sup>104</sup>.

When a shear band forms, there will be a fast drop in the shear stress  $\tau$  due to structural softening<sup>51,60</sup>. However, the tensile stress near the shear band will not drop instantly with the shear stress. Rather it would decrease following the size-dependent elastic unloading mechanism proportional to the shear offset  $S_g$  along the shear band,

$$\sigma_L(t) = \sigma_L(0) - \frac{(S_g \cos \theta - D)}{L} E \quad (6.7)$$

where  $L$  is sample length,  $E$  is the Young's modulus and  $D$  is the displacement of the machine, which is negligible during the fast shear banding process in the experiment and in our multi-scale simulation. Therefore Eq. (6.3) no longer holds. Before the  $S_g$  increases to a certain amount, the condition  $\tau < \sigma_L \sin \theta \cos \theta$  is present. Such transient non-equilibrium condition gives rise to the acceleration of the shear band gliding. The duration of the acceleration depends on sample size  $L$ . We can view the sample as two springs with masses  $M_1$  and  $M_2$  connected by a shear band as in Fig. 6.1. Due to machine confinement, the springs are not allowed to tilt. So the springs can only translate horizontally to accommodate the shear offset in the shear band.

Then we can calculate the real-time acceleration of such horizontal translation according to the differences between the shear component of the loading and the shear resistance in the shear band, which can be written as

$$\Delta \tau(t) = \frac{\sigma_z(t)}{\tan \theta} - \tau(t) \quad (6.8)$$

We assume that the machine stiffness is infinite and the friction perpendicular to the loading direction is zero. The horizontal component of acceleration of spring with  $M_1$  is given by:  $\frac{\Delta \tau - \frac{A}{\sin \theta}}{M_1} \times \sin \theta$ , with  $A$  being the cross section area. So the acceleration of the tip

(connected to the shear band) of spring  $M_1$  along the shear band direction is

$\frac{\Delta \tau - \frac{A}{\sin \theta}}{M_1} \times \sin \theta / \sin \theta = \frac{\Delta \tau - \frac{A}{\sin \theta}}{M_1}$ . Likewise, the acceleration of the tip of spring  $M_2$  along the shear

band direction is  $\frac{\Delta\tau}{M_2} \frac{A}{\sin\theta}$ . Here we ignore the effect of the bending wave propagation seen in full atomic simulations<sup>104</sup>. The real time acceleration of the top of the shear band relative to the bottom of the shear band is:

$$a_g(t) = \ddot{S}_g(t) = \frac{\left(\frac{\sigma_z(t)}{\tan\theta} - \tau(t)\right)A(t)}{\sin\theta} \left(\frac{1}{M_1} + \frac{1}{M_2}\right) \quad (6.9)$$

The MD simulation provides the continuum model with the real-time flow stress  $\tau$  in the shear band. Then the continuum model calculates the shearing off acceleration to get the gliding speed  $v_g$  along the shear band.  $v_g$  will be fed back to the MD simulation to control the shear strain rate of the small portion of the sample according to

$$\dot{\gamma}(t) = \frac{v_g(t)}{L_z(t)} = \frac{\int_{t_0}^t a_g(t)\Delta t}{L_z(t)} \quad (6.10)$$

Integrating  $v_g$  in time, the continuum model yields the shear off distance  $S_g$  and calculates the loading stress  $\sigma_L$  according to Eq. (6.7). In fact, we also considered the unloading from the dilatation in the shear band. But we found the unloading induced by the dilatation in the shear band is less than 1% of that from  $S_g$ . Updating the normal stresses in the shear band according to Eq. (6.7) and shear strain rate according to Eq. (6.10), the MD simulation proceeds to calculate the flow stress  $\tau$  and temperature  $T_{sb}$  in the shear band. The whole process runs into a loop as is illustrated in Fig. 6.1 (c).

### 6.2.3 Temperature control during plastic loading

During the plastic loading, most of the mechanical work will be transferred to heat in the shear band and dissipates away. If we keep the MD simulation in an NVE ensemble, heat cannot dissipate away once the heat front reach the boundary of the simulation box. If we run the simulation in an NVT ensemble, inappropriate amount of heat might be taken away. We solve this problem by coupling the boundary temperature in MD simulation to the continuum model that can calculate the temperature profile near the boundary at time  $t + \Delta t$  based on the temperature profile at time  $t$ .

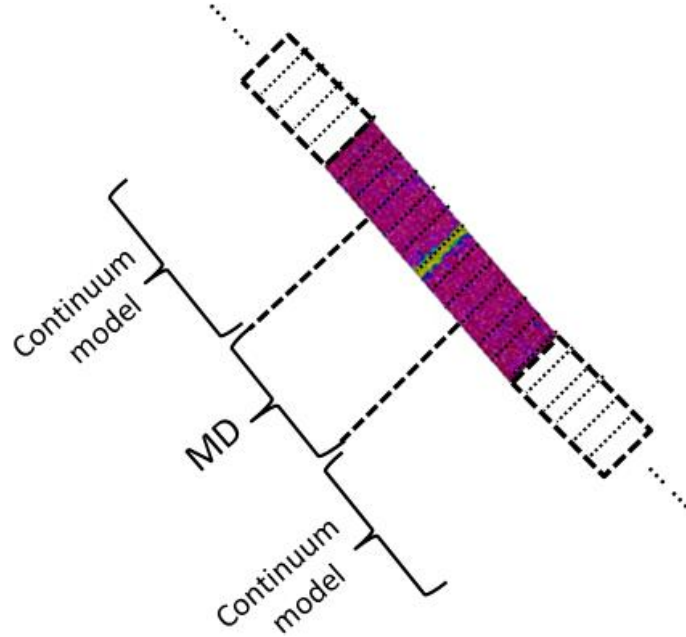


**Figure 6.3. Temperature coupling between MD simulation and continuum model. In the MD simulation, we slice the sample parallel to the shear band and record and feed the continuum model with the temperature in each slice. Then the continuum model updates the whole temperature profile and feeds the boundary temperatures back to the MD simulation. The middle part of the portion in MD simulation is kept in an NVE ensemble.**

As shown in Fig. 6.3, we bin the slab in  $z$  direction so each bin is parallel to the shear band. We begin to measure the temperature in each bin when a shear band forms. The temperature change in each bin of next time step is calculated according to heat conduction equation by the continuum model:

$$T_z(t) - T_z(t - \Delta t) \approx \alpha(T_z) \frac{\partial^2 T}{\partial z^2} \Delta t \approx \alpha(T_z) \frac{(T_{z-\Delta z}(t - \Delta t) + T_{z+\Delta z}(t - \Delta t) - 2T_z(t - \Delta t))}{\Delta z^2} \Delta t \quad (6.11)$$

$\Delta z$  is the bin size, which is set to be 0.9 nm in practice.  $\alpha T_z$  is the thermal diffusivity, which is a function of temperature. We measure thermal conductivity  $\kappa(T)$  via the Muller-Plathe algorithm<sup>228</sup>. We get  $\alpha T_z$  according to  $\alpha(T) = \frac{\kappa(T)}{C_p \rho}$ , with  $C_p$  and  $\rho$  to be

specific heat capacity and density respectively. Then we only control the temperature of the corresponding bins at the two ends of the sample in MD according to the continuum model and let the middle part (shear band is displaced to the middle once initiated) of the

sample evolve in an NVE ensemble. As heat is generated in the shear band not at the ends, no heat source term is needed in Eq. (6.11). The communication between MD simulation and the continuum model takes place every 0.05 ps to ensure the accuracy.

#### **6.2.4 Verification of the multi-scale simulation method**

We verified our multi-scale simulation method by comparing with the full MD simulation. The size of the whole sample is small ( $22.5(x) \times 2.5(y) \times 45(z)$  nm<sup>3</sup>) to allow the full MD simulation. In the multi-scale simulation, the MD simulation part only requires a  $7.5 \times 2.5 \times 15$  nm<sup>3</sup> small slab. We performed multi-scale simulation on 3 independent small slabs to check the statistic reliability. We compared the stress strain curve, gliding distance evolution and temperature profile evolution to the full MD simulation. Excellent agreement was achieved between the direct MD simulation and the multi-scale simulation in all of the 3 aspect.

### **6.3 Size dependent thermomechanical evolution of shear bands**

We start by applying the multi-scale simulation method on Wahnstrom BLJ samples. The sample size  $L$  studied ranges from 88 nm to 88  $\mu$ m. A  $21 \times 2.5 \times 92$  nm<sup>3</sup> slab is simulated with molecular dynamics to mimic a portion near the shear band of the whole sample. The glassy slab is quenched from 2000 K to 10 K in 25 ns. During the elastic loading with the strain rate of  $0.02$  ns<sup>-1</sup>, the shear band forms at around 5% strain. Although larger samples usually have a lower yield stress or fracture stress<sup>26,59,104</sup>, we assume all the samples yield at the same high stress here, to "search" for a fracture event as no fracture is reported on BLJ samples. During the plastic loading, the loading strain rate of the machine is set to be small enough, especially for the large samples, so that during plastic unloading<sup>58</sup> the displacement of the machine can be ignored. The strain rates are summarized in Table 6.1.

**Table 6.1. Loading strain rate summary for different sized samples. The unit for strain rate is in Lennard Jones unit, which is  $2ps^{-1}$ . The common strain rate used is  $10^{-4}$ .**

$L(\mu m)$	0.088	0.88	8.8	88
$e_L$	$10^{-5}$	$10^{-6}$	$10^{-7}$	$10^{-8}$

We present the shear band evolution in the domain of the normal stress and the local temperature to capture its thermomechanical nature. According to Eq. (6.7), a smaller sample is able to unload faster. So the acceleration stage of the shear band is very short according to Eq. (6.9). As a result, the temperature will only increase moderately during the transient shear band acceleration and then cool down as shear band slows down as shown in Fig. 6.4 for  $L = 88$  nm. When  $L$  gets large, the unloading will be slower and the acceleration can be maintained longer. Then the temperature can keep rising in the shear band. Due to the elevated temperature, the shear resistance in the shear band decreases, which can further accelerate the shear band gliding. If the sample size is very large, then effectively no unloading will result from the shear offset. Therefore the temperature in the shear band can keep rising without unloading. This is almost the case for  $L = 88 \mu m$  as shown in Fig. 6.4. But the temperature rise has a limit since the heat source in the shear band is proportional to  $v_g \tau_{sb}$ . When  $\tau_{sb}$  is close to zero, the temperature in the shear band will reach maximum, termed  $T_h$  here as is indicated in Fig. 6.4. It is speculated that  $T_h$  is the glass transition temperature  $T_g$ <sup>79</sup>. But in the experiment<sup>229</sup>, the shear stress is still very high at  $T_g$ , indicating that  $T_h$  can be a little larger than  $T_g$ . However, we found that although the shear band in the 8.8 and 88  $\mu m$  samples can approach  $T_h$  around 788 K, no fracture happened in the shear band.

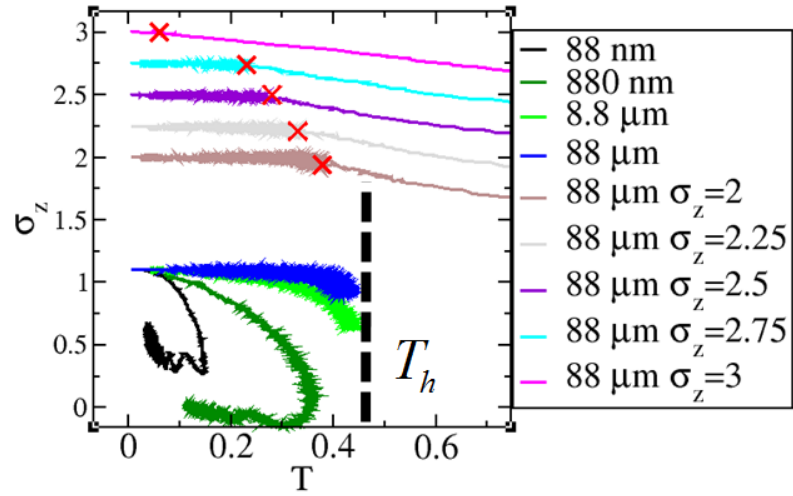


**Figure 6.4.** Thermomechanical evolution of the shear band in samples with listed length under original yield strength or artificially increased strength. There is a limit for temperature rise in the shear band, indicated by  $T_h$ , if the sample does not fracture.

To directly explore the fracture condition, we artificially increase the normal stresses at the beginning of the plastic deformation and only focus on the scenario with  $L = 88 \mu m$ . Fracture happens via cavitation in the shear band when the starting normal stress is equal or higher than 2.5 GPa. The cavitation stress is a function of temperature as indicated by the red crosses in Fig. 6.4.

Full atomic simulations on the modified BLJ samples have shown size dependent tensile fracture via shear band cavitation<sup>104</sup>. Here, we employ the multi-scale simulation to demonstrate it again as shown in Fig. 6.5. The strain rate for the 440 nm sample and for the 1.76  $\mu m$  sample is  $10^{-6}$  and  $10^{-7}$  respectively. The strain rate for other samples can be found in Table 6.1. When  $L$  is larger than 0.88  $\mu m$ , the sample will fracture. The stress states at fracture are shown in Fig. 6.5 (b), which are in agreement with those observed in full atomic simulations<sup>104</sup>. The close-up views of the deformation morphology near the shear band of the 0.88  $\mu m$  sample shown in Fig. 6.5 (c) demonstrate that the cavity forms in the hot shear band and soon propagates into a fatal crack. The crack propagates rapidly, resulting in intensive energy releasing and temperature rise, leaving two vein-like fracture surfaces with liquid-like droplets and

micro-voids, in agreement with experimental observations<sup>61,222</sup> and the full atomic simulation<sup>104</sup>.

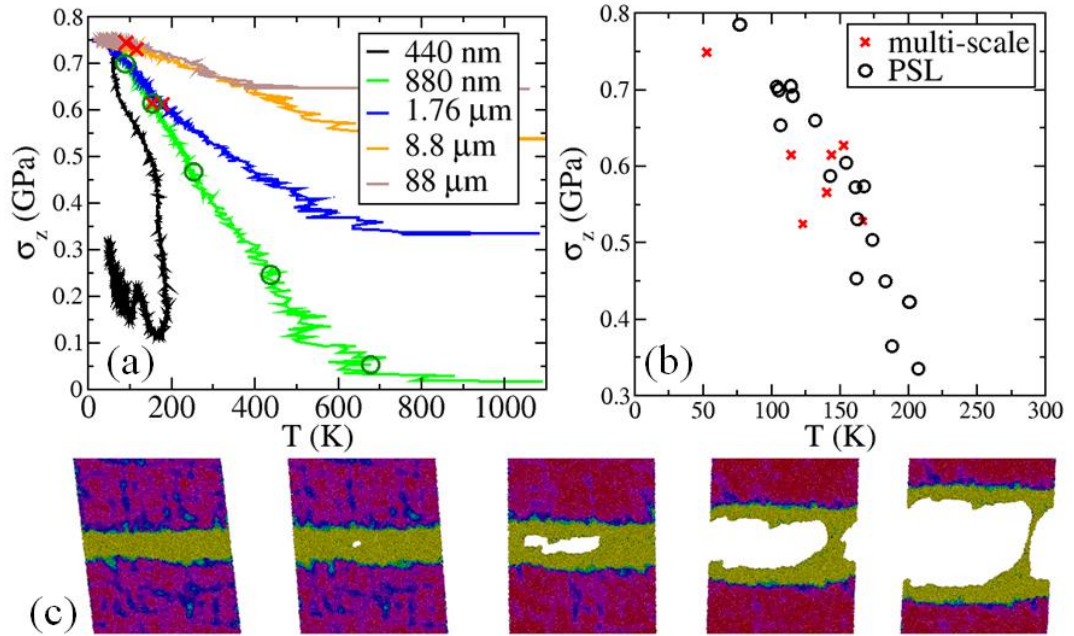


**Figure 6.5.** (a) Trajectories of the shear band in the domain of  $\sigma_z$  and  $T$  for the modified BLJ samples with sizes from 440 nm to 88  $\mu\text{m}$ . Red crosses indicate the cavitation states. (b) Cavitation states collected from the multi-scale simulations and full atomic simulations using perturbative static load (PSL)<sup>104</sup>. (c) Close-up view of the vicinity of the shear band the 0.88  $\mu\text{m}$  sample at the moments indicated by the dark green circles in (a).

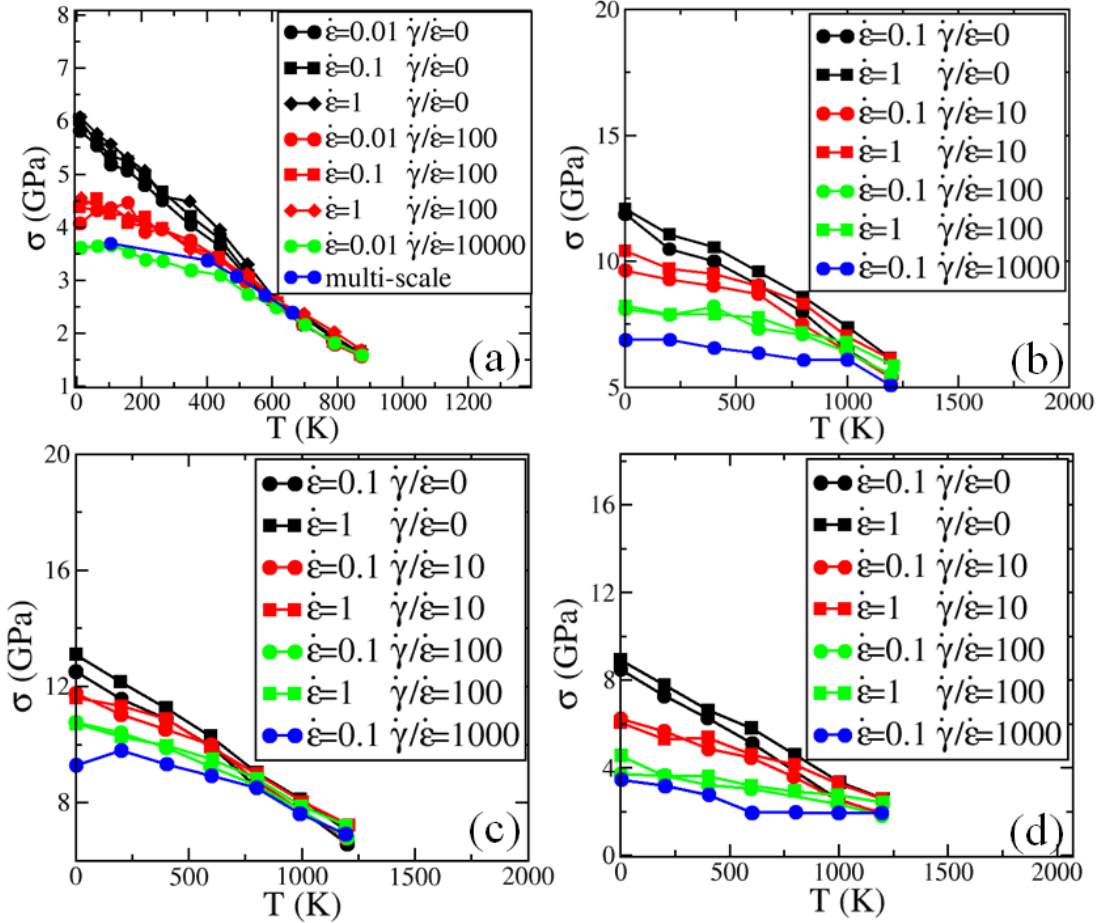


**Figure 6.6.** The cavitation stress as a function of temperature in small scale hydrostatic tension tests with or without shear flow for (a) BLJ, (b) Cu<sub>50</sub>Zr<sub>50</sub> [137], (c) Zr<sub>50</sub>Cu<sub>50</sub> [100], and (d) Fe<sub>80</sub>P<sub>20</sub> [138]. For BLJ, the strain rate  $\dot{\epsilon}$  and  $\dot{\gamma}$  are in the unit of  $0.2 \text{ ns}^{-1}$ . For the other model glasses, the strain rate  $\dot{\epsilon}$  and  $\dot{\gamma}$  are in the unit of  $0.5 \text{ ns}^{-1}$ .

To systematically evaluate the cavitation stress as a function of temperature, we conducted series of hydrostatic tension tests on small samples with dimensions close to the thickness of the shear band under constant strain rate at a range of temperatures. To mimic the shear flow in the shear band, we also conducted hydrostatic tension tests with a constant shear strain rate superimposed on the system. The cavitation stresses are presented in Fig. 6.6(a). If the system is under pure hydrostatic tension, the cavitation stress decreases almost linearly with temperature. The effect of strain rate is small as we lower the hydrostatic tension rate by two orders of magnitude, the cavitation stress at

corresponding temperature is almost the same. If shear flow is imposed on the system, significant drop in the cavitation stress is seen especially for the low temperature range. It is interesting to note that as we lower the shear strain rate by 2 orders of magnitude, the cavitation stress is the same if we also lower the hydrostatic tension strain rate proportionally. Therefore the shear flow weakening effect does not depend on the absolute value of the shear strain rate, but the relative shear strain rate to the hydrostatic tension strain rate. The behavior of the original BLJ sample is essentially the same as the modified BLJ sample<sup>104</sup>. As we further increase the relative shear strain rate, the cavitation stresses observed in the small scale simulation approach those observed in the multi-scale simulation as shown in Fig. 6.6(a).

## 6.4 Cavitation map

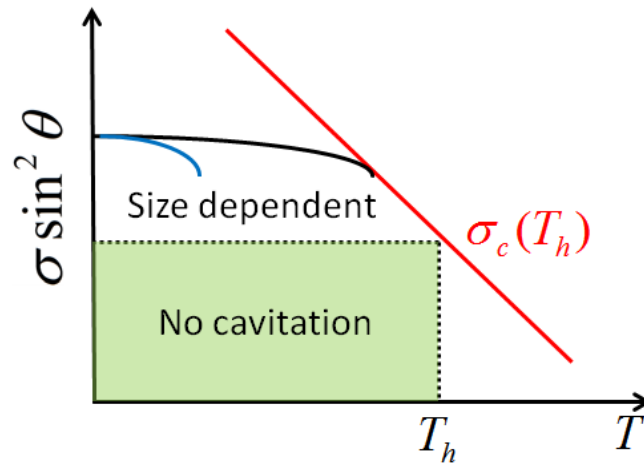


**Figure 6.7. The cavitation map.** When  $\sigma_y \sin^2 \theta$  is smaller than  $\sigma_c(T_h)$ , the shear band trajectory is confined in the light green region in the thermomechanical domain, where no cavitation is expected to happen. When  $\sigma_y \sin^2 \theta$  is larger than  $\sigma_c(T_h)$ , the cavitation in the shear band will depend on sample size. If the sample size is larger, the shear band trajectory (black curve) has a higher possibility to touch the cavitation line (red line). If the sample size is small, the shear band trajectory (blue curve) can avoid the cavitation line.

With the combination of the multi-scale simulation and the small scale simulation, we can now understand quantitatively why original BLJ sample does not cavitate in the shear band. As is illustrated in Fig. 6.7, if the normal stress in the shear band at yield

point  $\sigma_y \sin^2 \theta$  (or ultimate strength under uniaxial tension) is smaller than the cavitation stress at  $T_h$ , which is  $\sigma_c(T_h)$ , then no matter how large the sample is, the shear band cannot access the cavitation stress and therefore will not cavitate; if  $\sigma_y \sin^2 \theta$  is larger than  $\sigma_c(T_h)$ , then the tensile fracture via shear band cavitation will depend on the sample size as was also discussed in the full atomic simulation<sup>104</sup>. Since  $\sigma_y \sin^2 \theta$  is 1.6 GPa, smaller than  $\sigma_c(T_h) \sim 2$  GPa, the original BLJ sample under uniaxial tension could not cavitation in the shear band.

To apply our cavitation criterion to other model glasses, we further conducted the small scale hydrostatic tension tests with or without the shear flow on two  $\text{Cu}_{50}\text{Zr}_{50}$  model glasses<sup>100,137</sup> and the  $\text{Fe}_{80}\text{P}_{20}$  model glass<sup>138</sup>. Three general features in the cavitation stresses remain universal for all the systems as can be seen in Fig. 6.6. First, under pure hydrostatic tension state, cavitation stress decreases almost linearly with increasing temperature. This is probably due to the decrease in surface energy as temperature rises. Second, with the presence of the shear flow, cavitation stress at give temperature decreases with increasing relative shear strain rate to hydrostatic tension strain rate because the relative shear strain rate controls the proportionality between the cavitation normal stress and cavitation shear stress<sup>104</sup>. Third, the effect of the shear flow decreases with increasing temperature because the shear stress decreases to zero when the temperature is high. The  $\text{Fe}_{80}\text{P}_{20}$  model glass exhibits more fluctuations at high temperature probably related to the phase segregation for which the force field is designed<sup>138</sup>. The upper bound of  $T_h$  is estimated to be 1200K for all the three glasses, higher than their glass transition temperature. The ultimate strength under uniaxial tension of all three glasses are measured under the strain rate of  $5 \times 10^{-4} \text{ ps}^{-1}$ . The samples are quenched down to 1K with the quenching rate of 6 K/ps. For FeP glass, the ultimate strength under uniaxial  $\sigma_y$  is around 7.3 GPa.  $\sigma_y \sin^2 \theta$  is larger than  $\sigma_c(T_h)$  around 2 GPa shown Fig. 6.6(d). Therefore the size dependent tensile fracture via shear band cavitation can happen in the model  $\text{Fe}_{80}\text{P}_{20}$  glass. But for the CuZr glass and the ZrCu glass,  $\sigma_y$  is 3.8 GPa and 2.5 GPa respectively and  $\sigma_c(T_h)$  is 5 GPa and 6.6 GPa

respectively. As in tension the shear band angle<sup>212</sup> to the loading direction can be as large as  $60^\circ$ , which will increase the normal stress on the shear band by 50% comparing to the situation in which the shear band angle is  $45^\circ$ . Even we assume the shear band angle to be  $60^\circ$ ,  $\sigma_y \sin^2 \theta$  is much smaller than  $\sigma_c(T_h)$  for the two CuZr glasses as is shown in Fig. 6.6 (b) and (c). For cavitation to occur in the shear band for the CuZr glass and the ZrCu glass, the necessary  $\sigma_y$  is calculated to be 6.7 GPa and 8.8 GPa. Such high yield stress is highly unlikely to be realized even when we estimate the ultimate strength or yield stress will increase 60% if quenched with much slower rates accessible in the experimental time scale<sup>168</sup>.

One uncertainty is the rate dependency of the cavitation stress<sup>194</sup>. For the Wahnstrom BLJ glass<sup>124</sup> and the recently developed CuZr glass<sup>100</sup> the rate dependency of the cavitation stress at high temperature is very small. While the other CuZr glass<sup>137</sup> exhibit stronger rate dependent cavitation stress at high temperature. Further study in this direction is warranted to confirm whether the force field is capable of capturing the shear band cavitation behavior under uniaxial tension at much longer time scale.

The tensile ductility in micron-sized metallic samples is not observed in experiment. Therefore the ductility of the two CuZr glasses and the Wahnstrom glass is highly likely to be overestimated. Intrinsic ductility of metallic glasses was related to the Poisson's ratio<sup>64</sup> and was recently correlated to covalency in the bonding of metallic glasses<sup>130</sup>. In fact, covalent bonding has been associated with the brittleness of intermetallic compounds for a long time<sup>230</sup> and it was proposed by David Pettifor that angular dependent potentials should be developed to explain this bonding effect on ductility<sup>230</sup>. Although the difference between the CuZr EAM potential and FeP EAM potential is difficult to characterize, the difference between Wahnstrom BLJ potential and the modified BLJ potential is clear. It is a repulsive energy bump at second-nearest neighbor distance originated from first-principle studies<sup>152-154</sup> to control the angular constraint or covalency in the bonding of the model glass. It enables the simulation of size dependent tensile fracture via shear band cavitation<sup>104</sup> and reveals the link between Poisson's ratio and intrinsic ductility of metallic glasses<sup>130</sup>. We believe such modification to mimic covalency in bonding conveys a very important message on the force field development

for better characterization of the complicated mechanical behaviors of glasses and even crystals.

## **6.5 Summary**

In summary, the puzzle regarding the size dependent tensile fracture of metallic glasses is solved within hundreds of micron meter scale in space and tens of nano-second scale in time based on the cavitation map. A longer timescale or larger space scale will probably lead to the change in relative magnitude of the ultimate tensile strength and cavitation stress on the cavitation map, but not the general scheme presented by the cavitation map. Further studies are needed to understand the rate dependency of the cavitation stress with the presence of shear flow. Based on the cavitation map, we find the ductility is likely to be overestimated in Wahnstrom BLJ potential and the two widely used CuZr EAM potentials. Better characterization of the electronic interaction, especially the angular component of the interaction (covalency), should be given more attention in future studies.

## 7. Low Cycle Fatigue of Metallic Glass Nanowires

### 7.1 Introduction

Nanometer-scaled metallic glasses have emerged as a scientifically interesting and technologically useful structural material<sup>34,231</sup>. They possess an unusual suite of properties, such as excellent formability<sup>232</sup>, high elastic limit<sup>13,14,26</sup>, high strength<sup>26,36</sup> and high ductility<sup>25,26,36</sup>. Therefore, metallic glasses have great advantages for applications in the fields of microelectromechanical<sup>32</sup>, nanoelectromechanical systems<sup>33</sup>, micromachines<sup>34</sup> and biomedical applications<sup>35</sup>. To utilize the extraordinary properties of nanometer-scaled metallic glasses, bulk metallic glass composites with nanometer-scaled microstructure<sup>233,234</sup>, or bulk metallic glass foams<sup>235</sup> with ligaments of nanometer-sized cross sections have been developed, which significantly enhanced the application prospects of metallic glasses. In the context of the above real-world applications, the fatigue behavior of nanometer-scaled metallic glasses, however, receives much less attention. Such omission is significant, since fatigue failure accounts for more than 90% of all mechanical failures<sup>28</sup>.

The fatigue limit of the submicron-sized metallic glasses was found to be as high as the yield stress<sup>69</sup>. Bulk metallic glass composites with micron-sized microstructures also exhibit enhanced fatigue endurance limit<sup>236</sup>. In the few experiments devoted to the cyclic deformation of nanometer-scaled metallic glasses, work-hardening was observed under cyclic tension<sup>13,26</sup> or in nano-indentation test<sup>237</sup>. However, the exact fatigue fracture mechanism and the quantitative description of the fatigue life of nanometer-scaled metallic glasses are largely unknown.

Molecular dynamics (MD) simulations can provide important atomistic insights on the fatigue failure. In existing MD simulations on the fatigue behavior of metallic glasses, directional localization of free volume<sup>128</sup> and defects<sup>129</sup> were suggested to be important for the fatigue damage initiation. Cyclic loading induced hardening<sup>238</sup> and crystallization<sup>239</sup> have also been observed in recent atomic simulations. However, it is challenging to directly simulate fatigue fracture in MD simulations. The foremost challenge arises from the deficiency of the available atomic force fields<sup>130</sup>, which usually

lead to model metallic glasses that are significantly more ductile than experimental metallic glass systems. For instance, the amorphous nanowire modeled by the widely used Lennard-Jones force field<sup>124</sup> exhibits little damage, let alone fracture, even after extensive push-pull cyclic loading with a strain amplitude as high as 36% in our preliminary result. Moreover, it has been shown that the sample preparation can significantly affect the deformation mode of the nanoscale metallic glass samples.<sup>240</sup> Specifically, nanoscale metallic glass samples made from the traditional cutting method (vitrify a bulk liquid to bulk glass, then cut to a nanowire) have unrelaxed surfaces, which will in turn suppress the shear band formation and likely fatigue fracture. As a result, to our best knowledge, no direct fatigue fracture process of metallic glass nanowires has been observed in MD simulations.

In this study, we conducted cyclic compression tension tests with a large strain range to directly examine the low cycle fatigue fracture behavior of metallic glass nanowires with atomic details. During the cyclic loading, the nanowire hardens under low strain amplitude and softens under higher strain amplitude. The final fracture of the nanowires is caused by rapid shear band formation, true for the entire range of strain amplitudes explored in this study. In the plastic strain controlled fatigue tests, the fatigue life of the nanowire follows the Coffin-Manson relation. This power-law form can be rationalized from the microscopic deformation damage accumulation, which depends on the macroscopic plastic strain amplitude.

## 7.2 Simulation methodology

MD simulations were carried out with LAMMPS<sup>200</sup> (Large-scale Atomic/Molecular Massively Parallel Simulator) package (<http://lammps.sandia.gov>) with a customized force field<sup>130</sup>. The force field is inspired by the Dzugutov potential<sup>241</sup>, which features an energy bump to mimic the Friedel's oscillations<sup>116,149-151</sup> and to control the bonding covalency, thus can reduce the excessive ductility commonly presents in model metallic glasses. In this study, the bump height parameter used is 0.3. The corresponding model glassy nanowire fractures via shear banding (loses half of the tensile stress at around 20% strain) in an uniaxial tensile test<sup>130</sup>. A standard velocity Verlet integrator with a time-step

of 5 fs was used. Temperature control and stress control used in the MD simulations follow the standard Nose-Hoover formulation<sup>162,163</sup>. Similar to a previous study<sup>130</sup>, glassy nanowires with the length of 24.3 nm and diameter of 11.3 nm (about 0.13 million atoms) were chosen. Due to the high loading cycles required in fatigue tests, a study with a larger sample size is very demanding at this moment. The nanowires were melted and equilibrated at a high pressure (9.4 GPa) and high temperature (2000 K) in a cylindrical container and quenched into a metallic glass nanowire with zero pressure and at 60 K, with a cooling rate of  $8.7 \times 10^{11} \text{ K/s}$ . The quenching process mimics the experimental casting<sup>240</sup>. Thus, the as-quenched glassy nanowires have relaxed surfaces<sup>240</sup>. Periodic boundary condition applies only in the axial direction. During fatigue tests, the nanowire was uniaxially loaded by rescaling the simulation box with a strain rate of  $0.4 \text{ ns}^{-1}$ . The temperature was maintained at 60 K (20% of the glass transition temperature  $T_g$ ) during the fatigue tests.

### 7.3 Total-strain-controlled fatigue tests

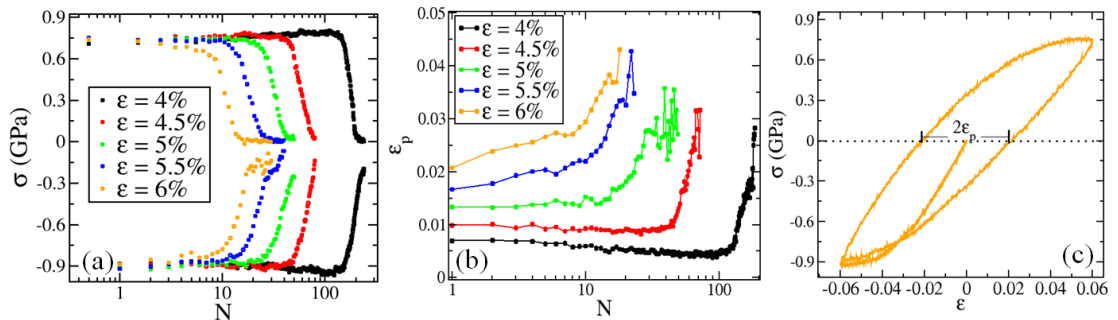


**Figure 7.1.** (a) The peak compression (negative) and tension (positive) stress during total-strain-controlled compression-tension fatigue tests. The applied total strain magnitudes are given in the legend. The stress amplitude decreases sharply towards fatigue fracture. (b) A representative stress-strain hysteresis loop for a fatigue test with a 6% strain amplitude. The strains are positive in tension and negative in compression. As indicated, the plastic strain is defined as half of the strain difference between the two zero-stress points. (c) The plastic strain of every cycle during typical total-strain-controlled fatigue tests. The cycles are shown on a log scale. The applied total strain magnitudes are given in the legend.

First, we applied total-strain-controlled symmetric compression-tension fatigue tests on the nanowires, in which the strain amplitude in tension or compression spans from

4% to 6% with the interval of 0.5%. Five independent samples were tested for each strain amplitude to investigate the statistics of the fatigue behaviors. Shown in Fig. 7.1(a), at the total strains of 4% and 4.5%, the stress exhibits a slightly cyclic-hardening behavior before fracture (upon which the stress drops significantly). However, at higher strain levels, there is generally a cyclic-softening behavior before the stress significantly drops. The fatigue life of the sample was identified as the first cycle in which the peak tensile stress reduces to half of the initial stress amplitude. The tensile stress was chosen here since the fractured sample might still be able to sustain a certain amount of compressive stress. The plastic strain  $\varepsilon_p$  of every cycle is defined to be half of the strain difference between the two zero-stress points, as shown in Fig. 7.1(b). As shown in Fig. 7.1(c), the higher the applied total strain amplitude  $\varepsilon$ , the higher the plastic strain  $\varepsilon_p$  observed. Similar to the stress evolution,  $\varepsilon_p$  also exhibits either softening or hardening behavior, depending on the strain amplitude. For samples with total-strain amplitudes lower than 4.5%,  $\varepsilon_p$  decreases during the majority of the cyclic loading, before surges rapidly upon failure. Cyclic strain induced work hardening behavior was also observed in nano-indentation tests<sup>237,238</sup> and in cyclic tensile tests on metallic glass nanowires<sup>13,26</sup>. With the total-strain amplitude of 5%, the plastic strain  $\varepsilon_p$ , maintains at a constant level until fracture. For samples with total-strain amplitudes higher than 5%, the plastic strain increases during the whole fatigue tests, indicating strain softening behavior.

The sudden increase in the plastic strain marks the onset of fracture in all of the total-strain-controlled fatigue tests. The atomic deformation morphology further reveals that the onset of fracture is caused by the rapid shear band formation and propagation process as shown in the side views of the nanowires of Fig. 7.2. The color coding follows the local atomic shear strain according to a previous study<sup>161</sup>. The top views of the nanowires during fatigue tests evidently show that the shear band initiates at the surface and floods into the nanowire at the later stage of the fatigue test. While the cause

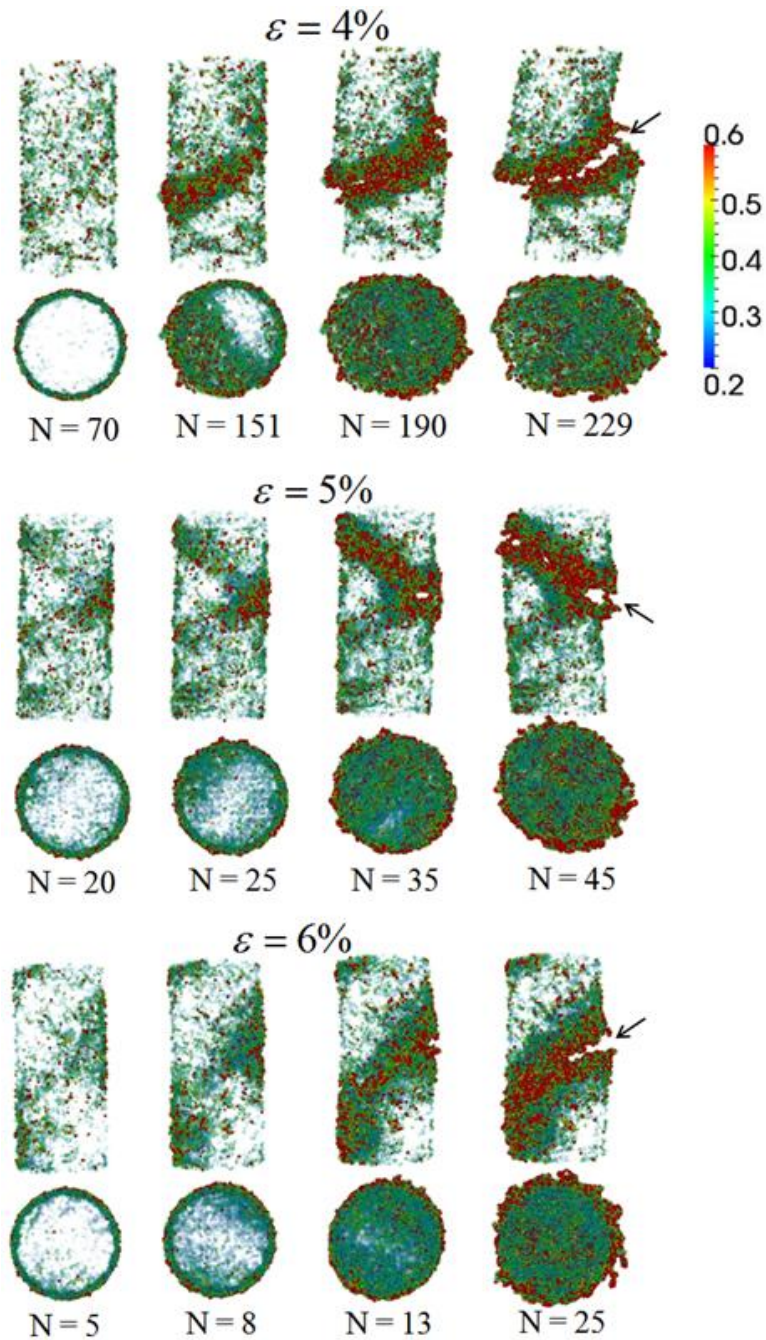


**Figure 7.2.** The side and top views of the deformation morphology of the model metallic glass nanowires during total-strain-controlled fatigue tests with strain amplitudes of 4% (upper panel), 5% (middle panel) and 6% (lower panel). Each arrow indicates the location of the crack inside the shear band after fracture. The atoms were colored according to the local shear strain. The opacity of atoms is also controlled by the local shear strain such that an atom with a shear strain lower than 0.2 is invisible and an atom with a shear strain higher than 0.6 is fully opaque.

of fatigue failure of macroscopic metallic glasses seems complex, with cracks or a mixture of crack and shear banding involved<sup>242,243</sup>, we show here that shear banding is the major failure mechanism for nano-scale metallic glass samples in low cycle fatigue tests. Such shear banding behavior is somewhat similar to the persistent slip bands, which is the major form of damage for crystalline materials under fatigue tests<sup>244–247</sup>. In low cycle fatigue for nano-scale metallic glasses, as we show here, the majority of the fatigue life is spent in the shear band initiation. While in high cycle fatigue tests of macroscopic metallic glass samples, it was reported that the crack propagation process almost takes up the whole fatigue life<sup>74</sup>.

#### 7.4 Plastic-strain-controlled fatigue tests

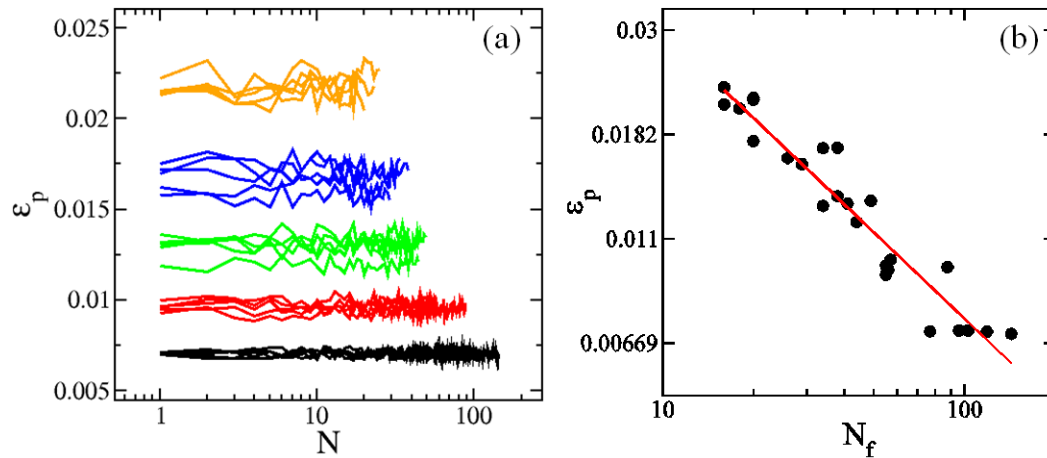


**Figure 7.3.** (a) The plastic strain  $\varepsilon_p$  as a function of the cycle number during plastic-strain-controlled fatigue tests. All five parallel tests are shown, each with initial total strain magnitude of 4% (black), 4.5% (red), 5% (green), 5.5% (blue) and 6% (orange), respectively. (b) Fatigue life as a function of plastic strain for all samples in a log-log plot. The red line is the best fitting according to the Coffin-Manson relation  $\varepsilon_p = \varepsilon_f N_f^c$ , where  $\varepsilon_f = 0.118$  and  $c = -0.6$ .

To better understand or predict the low cycle fatigue behavior of the amorphous nanowires, it is important to evaluate the quantitative relationship between the plastic strain and the fatigue life. In fact, the fatigue life has long been directly associated with the plastic strain in the well-known Coffin-Manson relation<sup>248</sup> in the form of

$\varepsilon_p = \varepsilon_f \times N_f^c$ , where  $N_f$  is the fatigue life,  $\varepsilon_f$  and  $c$  are two fitting parameters termed the fatigue ductility coefficient and the fatigue ductility exponent, respectively.

To directly quantify the effect of plastic strain, we conducted MD simulations of plastic-strain-controlled fatigue tests. Experimental plastic-strain-controlled fatigue tests have been conducted on crystalline materials<sup>244–247,249</sup>, in which the estimation of the elastic strain amplitude was required to determine and tune the plastic strain amplitude in real time. However, the estimation of the elastic strain might not be accurate due to the complicated softening and hardening behavior during the fatigue test. In addition, the estimation of elastic strain can be further obscured if the stress-strain loops during the fatigue tests on the amorphous nanowires do not exhibit well defined yield points, as shown in Fig. 7.1(b). Therefore, more accurate evaluation of the plastic strain should be used, for instance, the definition based on the loading cycle that is completed as in Fig. 7.1(b). The plastic strain measured here does include a small time-dependent irreversible visco-plastic component<sup>250,251</sup>, without any reversible anelastic strain.

In our simulations, the exact control of plastic strain with accurate assessment of the elastic strain was implemented as follows. For each sample, we first conducted one cycle of loading with a total strain between 4 to 6%. The plastic strain measured during the first cycle was set as the target plastic strain. At the beginning of every cycle, the sample system was subjected first to a trial cycle with the total strain applied in the last cycle. If the plastic strain measured during the trial cycle is not within a 5% error of the target plastic strain, another trial cycle will be carried out on the system at the beginning of this cycle with an adjusted total strain (via a feedback loop based on the deviation from the target). For each initial total strain, we run five parallel tests, of which the target strain might be slightly different (see Fig. 7.3(a)) due to sample-to-sample variation.

The validity of the plastic strain controlled fatigue tests is demonstrated in Fig. 7.3(a). In order to keep the plastic strain at constant, the applied total strain in each accepted cycle varies. The variation of the applied total strain during the typical plastic-strain-controlled fatigue tests exhibit again a plastic-strain-dependent work hardening or softening behavior, which is very similar to the fatigue tests with constant total strains as shown in Fig. 7.1(c). While the softening or final fracture of the amorphous nanowire is

clearly associated with the shear band, the exact structural origin for hardening is not clear. As suggested by a recent atomic simulation on amorphous CuZr<sup>238</sup>, the subtle structural change associated with hardening induced by cyclic deformation requires better classification of the atomic structure of amorphous solids.

With plastic-strain-controlled fatigue tests, we can directly plot the fatigue life as a function of the plastic strain. As shown in Fig. 7.3(b), the fatigue life of the metallic glass nanowires varies with the plastic strain in a power-law relation as in  $\varepsilon_p = \varepsilon_f \times N_f^c$ , which is identical to the Coffin-Manson relation<sup>248</sup>. The fatigue ductility exponent  $c$  is found to be - 0.6, similar to that of the crystalline metals in the range between - 0.5 and - 0.7<sup>28</sup>. The fatigue ductility coefficient  $\varepsilon_f$  is found to be 0.118. It is interesting to note that the Coffin-Manson relation was originally observed under the plastic strain controlled fatigue tests on the crystalline copper in experiment<sup>244,246</sup>. Thus, the Coffin-Manson relation appears to be insensitive to the amorphous or crystalline atomic structure of the sample.

## 7.5 Understand the power law from damage accumulation

We further explore why the Coffin-Manson relation is valid in the plastic strain controlled fatigue test for the model metallic glass nanowires. The Coffin-Manson relation is usually rationalized in terms of crack growth via the Paris law  $\frac{da}{dN} = A(\Delta K)^p$ ,<sup>28</sup> where  $a$  is the crack length,  $N$  is applied cycles,  $\Delta K$  is the stress intensity factor range and  $A$  and  $p$  are two fitting parameters. However, in the model metallic glass nanowire, no apparent crack is introduced or formed, except the very late stage of the low cycle fatigue tests. Therefore, fatigue damage evolution in terms of shear band development, instead of crack propagation should be considered here. Here, any atom with a higher than 20% local shear strain is considered part of the damaged region. As shown in Fig. 7.2, a threshold of 20% in the local shear strain delineates the local deformation very well. It should be noted that a different threshold strain for damage (such as 15% or 25%) will not affect the following analysis. Thus, the fatigue damage ( $D$ ) can be quantified as the ratio of the number of atoms in the damaged region relative

to the total number of atoms in the sample, similar to the deformation participation ratio used in an earlier report to quantify shear localization<sup>51</sup>.

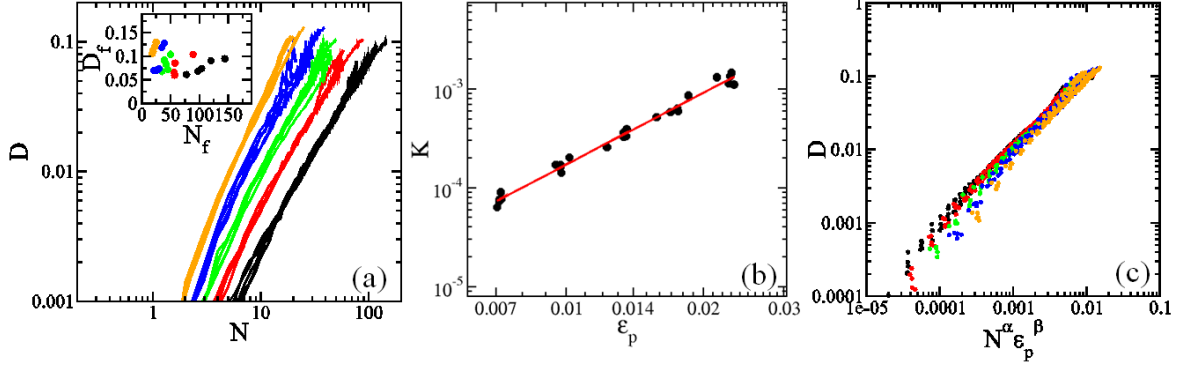


**Figure 7.4.** (a) Accumulative damage  $D$  as a function of the cycle number in plastic-strain-controlled fatigue tests in a log-log plot. According to the damage evolution relation  $D = K(\epsilon_p)N^\alpha$ , the exponent  $\alpha$  is taken as 1.5, independent of the plastic strain. All five independent tests are shown, each with the initial total strain amplitudes of 4% (black), 4.5% (red), 5% (green), 5.5% (blue) and 6% (orange), respectively. The damage at fracture  $D_f$  and life  $N_f$  are shown in the inset with the same color coding. (b) The prefactor  $K$ , defined as  $D/N^\alpha$ , is plotted as a function of the plastic strain  $\epsilon_p$ . The red line is fitted by  $K = A\epsilon_p^\beta$ , where  $A = 11.8$  and  $\beta = 2.4$ . (c) Accumulative damage  $D$  are plotted as a function of  $N^\alpha \epsilon_p^\beta$  ( $\alpha = 1.5$  and  $\beta = 2.4$ , obtained from fitting of the previous two panes) in a log-log plot, showing data collapse for all samples under different plastic strains with an apparent slope of 1.

In Fig. 7.4(a), the accumulative damage during plastic strain controlled fatigue tests are shown to increase with cycle  $N$ . The curves can be effectively described in the form of  $D = K(\epsilon_p)N^\alpha$ , in which  $K(\epsilon_p)$  is the pre-factor that increases with the plastic strain  $\epsilon_p$ . The exponent  $\alpha$  is found to be approximately 1.5 (ranging from 1.3 to 1.6 for all the data). Consequently, the damage per cycle can be written as  $\frac{dD}{dN} \propto N^{\frac{1}{2}}$  or  $\frac{dD}{dN} \propto D^{\frac{1}{3}}$ .

Thus, the damage generation rate is proportional to  $D^{\frac{1}{3}}$  (the size of a three-dimensional shear band nucleus). Next,  $K(\epsilon_p)$  can be obtained from Fig. 7.4(a) via fitting, assuming  $\alpha$  to be 1.5. Fig. 7.4(b) shows that  $K = A\epsilon_p^\beta$ , where  $A = 11.8$  and  $\beta = 2.4$ . Therefore

the accumulated damage can be written as  $D = A\varepsilon_p^\beta N^\alpha$ . Fig. 7.4(c) shows excellent data collapsing in the  $D$  vs.  $\varepsilon_p^\beta N^\alpha$  graph, supporting the damage evolution relation.

The above damage accumulation relation provides a mechanistic explanation of why the fatigue life of the nanowire follows the Coffin-Manson relation. As shown in the inset of Fig. 7.4(a), the damage at fracture ( $D_f$ ) is roughly a constant of  $0.09 \pm 0.03$  for all fatigue tests. Therefore, one can assume fatigue fracture occurs when the damage  $D$  reaches a threshold value  $D_f$ . From  $D_f = A\varepsilon_p^\beta N_f^\alpha$ , we have  $\varepsilon_p = (D_f / A)^{1/\beta} \times N_f^{-\alpha/\beta}$ , identical to the Coffin-Manson relation. Here  $(D_f / A)^{1/\beta}$  was estimated to be  $0.13 \pm 0.02$ , very close to the fatigue coefficient  $\varepsilon_f$  measured as 0.118 in Fig. 7.3(b). In addition, the exponent  $-\alpha / \beta$  can be calculated as -0.625, which is also very close to the fatigue ductility coefficient  $c$  measured as -0.6 in Fig. 7.3(b). Thus, the Coffin-Manson relation is recovered by connecting the microscopic accumulative damage with the macroscopic plastic strain.

Our simulation results reveal that the fatigue failure of metallic glass nanowires is a result of local damage accumulation, which is further controlled by the macroscopic plastic strain via a power law. In other words, if the plastic strain is zero, then no fatigue failure is expected because no damage will be accumulated. Therefore the fatigue limit of metallic glass samples free from defects should approach the yield strength itself. This is in line with a recent experimental finding<sup>69</sup> that micrometer scale metallic glass samples have exceptionally high fatigue limits. Note that the fatigue limit of macroscopic samples will likely be degraded by the local damage accumulation triggered inevitably by defects or stress concentrators.

## 7.6 Summary

In conclusion, shear banding appears to be the main failure mode of model metallic glass nanowires under low cycle fatigue tests. The fatigue life in plastic-strain-controlled cyclic loading obeys the Coffin-Manson relation. The accumulation of the local atomic damage was found to be controlled by the macroscopic plastic strain via a power law,

from which the Coffin-Manson relation can be derived. Our study provides a quantitative relation to assess the fatigue reliability of nanoscale metallic glass samples under cyclic loading.

## 8. Conclusions and Outlooks

### 8.1 Conclusions

Our micron scale atomic simulations revealed that brittle tensile failure of metallic glasses is caused by shear band cavitation, for which the critical thermomechanical states were captured. Contrary to the common belief, our results indicate that reaching glass transition temperature in the shear band is not a necessary fracture condition for metallic glasses under tension. Importantly, the simulations revealed that fast shear flow can reduce the critical stress for cavitation by a surprisingly large amount. If the shear flow is restricted (for example, ahead of the crack tip in a tough metallic glasses), the resistance of a shear band to cavitation can remain quite high. This shear flow activated cavitation mechanism explains why tough metallic glasses can be extremely brittle under tension. An analytical model was also derived to describe the size dependency of the shear band cavitation. When sample length is large, our model is numerically similar to the modified energy based model<sup>59</sup>. When sample size approaches zero, our model converges to the highest fracture strength while the energy based model diverges to infinite. Our analytical model can serve as a quantitative guide in selecting and designing ductile metallic glasses via tuning the thermal properties of metallic glasses. It is also a guide to the design safer nano- and micro-mechanical systems using metallic glasses.

We further designed a concurrent multi-scale simulation method to capture the shear band evolution in macroscopic samples under tension. A cavitation map is derived from the multi-scale simulations to quantitatively evaluate whether a given force field can display size dependent tensile fracture via shear band cavitation or not. It is found that some widely used sophisticated many-body force fields might overestimate the tensile ductility. Angular constraint in the force field is demonstrated to be an important factor of tuning the tensile ductility of metallic glasses.

On the fatigue properties of metallic glass nanowires, we conducted plastic strain controlled low cycle fatigue tests to quantitatively evaluate the damage accumulation mechanism. It was found that the failure is caused by shear banding. The microscopic

damage that leads to shear banding is controlled by the macroscopic plastic strain via a power law. Based on the damage accumulation law, we derived that the low cycle fatigue life of metallic glasses follows the well-known Coffin-Manson relationship. During the fatigue tests, we also observed load-dependent work hardening or softening behavior. It is interesting that the plastic strain controlled damage accumulation law is not affected by the apparent hardening or softening behavior of the nanowires.

Using force tuning methods, we were able to directly demonstrate that both the tensile ductility and fatigue resistance are controlled by the angular constraint or covalency in the bonding. A large angular constraint was shown to reduce the fracture toughness, tensile ductility and fatigue resistance. Interestingly, a large angular constraint was also observed to lower the Poisson's ratio of the glassy sample. Therefore the link between Poisson's ratio and plasticity is the angular constraint in the bonding. The insight gained through force tuning can help guide the composition selection in the design of more ductile and reliable metallic glasses. In practice, we could not tune the covalency without changing the bonding strength. Therefore we need to focus on the ratio of the covalency and bonding strength instead of covalency alone.

## 8.2 Outlooks

We identify several important but challenging questions that have not been solved currently. First, we have made it clear how a running shear band transits to a crack by cavitation, but it is unclear how a shear band propagates across the sample. It is argued that the shear banding process happens in an autocatalytic manner<sup>178,253</sup>, but the exact mechanism is unclear. At this moment, a variety of mechanisms have been proposed in the literature, including the dislocation model<sup>98</sup>, shear crack model<sup>79,179</sup>, Eshelby inclusion alignment model<sup>43,44</sup> and general stacking fault model<sup>156</sup>. Therefore, it would be important to test these models in independent atomic simulations without any input from the continuum level theory. Such atomic simulations will require a large sample size and possibly long simulation time with a high temporal and spatial resolution, therefore posing a serious challenge in computing resources and data analysis.

Another challenge is to directly measure and understand the fracture toughness of metallic glasses. Since the sample size in the current simulation is at most micron level, the large fracture toughness can be directly measured is therefore at most on the order of  $1 \text{ MPa}\sqrt{\text{m}}$  given the fracture stress is around 1 GPa. To study the sample with the fracture toughness on the order of  $100 \text{ MPa}\sqrt{\text{m}}$  would require a sample dimension that is four orders of magnitude larger, which is almost impossible to achieve in atomic simulations in the near future. Therefore, new multi-scale simulation method should be developed in this regard. Such simulations are required in order to understand the controlling factor for crack shielding mechanism to achieve high fracture toughness in metallic glasses.

A seemingly simple yet difficult to answer question is to analytically understand the Poisson's ratio of glasses. At this moment, we can analytically derive the Poisson's ratio of a glass with or without angular constraint, if only affine elastic deformation is considered. However, in reality, the non-affine relaxation during elastic loading in glasses makes it challenging to analytically calculate the Poisson's ratio. Therefore, a better understanding of the structural relaxation during elastic loading is the key to this question.

The fatigue properties of metallic glasses still remain mostly undefined. Currently, we were only able to deal with low cycle fatigue tests on nanoscale samples. How the damage will be accumulated in a larger sample during high cycle fatigue tests is still far beyond our reach. Some acceleration techniques in time are required in order to study the damage accumulation mechanism over an extended period of cyclic loading.

## References

1. Klement, W., Willens, R. H. & Duwez, P. Non-crystalline structure in solidified gold–silicon alloys. *Nature* **187**, 869–870 (1960).
2. Pampillo, C. A. & Chen, H. S. Comprehensive plastic deformation of a bulk metallic glass. *Mater. Sci. Eng.* **13**, 181–188 (1974).
3. Drehman, A. J. Bulk formation of a metallic glass: Pd<sub>40</sub>Ni<sub>40</sub>P<sub>20</sub>. *Appl. Phys. Lett.* **41**, 716 (1982).
4. Inoue, A. Stabilization of metallic supercooled liquid and bulk amorphous alloys. *Acta Mater* **48**, 306 (2000).
5. Peker, A. & Johnson, W. L. A highly processable metallic glass: Zr<sub>41.2</sub>Ti<sub>13.8</sub>Cu<sub>12.5</sub>Ni<sub>10.0</sub>Be<sub>22.5</sub>. *Appl. Phys. Lett.* **63**, 2342 (1993).
6. Wang, W. Roles of minor additions in formation and properties of bulk metallic glasses. *Prog. Mater. Sci.* **52**, 540–596 (2007).
7. Li, Y. *et al.* Formation of bulk metallic glasses and their composites. *MRS Bull.* **32**, 624–628 (2011).
8. Ding, S. *et al.* Combinatorial development of bulk metallic glasses. *Nat. Mater.* (2014).
9. Zhong, L., Wang, J., Sheng, H., Zhang, Z. & Mao, S. X. Formation of monatomic metallic glasses through ultrafast liquid quenching. *Nature* **512**, 177–180 (2014).
10. Schuh, C., Hufnagel, T. & Ramamurty, U. Mechanical behavior of amorphous alloys. *Acta Mater.* **55**, 4067–4109 (2007).
11. Greer, A. L. Metallic glasses... on the threshold. *Mater. Today* **12**, 14–22 (2009).
12. Johnson, W. & Samwer, K. A Universal criterion for plastic yielding of metallic glasses with a  $(T/T_g)^{2/3}$  temperature dependence. *Phys. Rev. Lett.* **95**, 195501 (2005).
13. Tian, L. *et al.* Approaching the ideal elastic limit of metallic glasses. *Nat. Commun.* **3**, 609 (2012).
14. Jiang, Q. K. *et al.* Super elastic strain limit in metallic glass films. *Sci. Rep.* **2**, 852 (2012).
15. Schroers, J. & Johnson, W. Ductile bulk metallic glass. *Phys. Rev. Lett.* **93**, (2004).
16. Demetriou, M. D. *et al.* A damage-tolerant glass. *Nat. Mater.* **10**, 123–128 (2011).
17. Xu, J. & Ma, E. Damage-tolerant Zr–Cu–Al-based bulk metallic glasses with record-breaking fracture toughness. *J. Mater. Res.* **29**, 1489–1499 (2014).
18. Johnson, W. L. *et al.* Beating crystallization in glass-forming metals by millisecond heating and processing. *Science* **332**, 828–833 (2011).
19. Schroers, J. Processing of bulk metallic glass. *Adv. Mater.* **22**, 1566–1597 (2010).
20. Schroers, J. & Johnson, W. L. Ductile bulk metallic glass. *Phys Rev Lett* **93**, 255506 (2004).
21. Das, J. *et al.* ‘Work-hardenable’ ductile bulk metallic glass. *Phys. Rev. Lett.* **94**, 205501 (2005).
22. Chen, M., Inoue, A., Zhang, W. & Sakurai, T. Extraordinary plasticity of ductile bulk metallic glasses. *Phys. Rev. Lett.* **96**, 245502 (2006).
23. Liu, Y. H. *et al.* Super plastic bulk metallic glasses at room temperature. *Science* **315**, 1385–1388 (2007).

24. Qu, R. T., Calin, M., Eckert, J. & Zhang, Z. F. Metallic glasses: Notch-insensitive materials. *Scr. Mater.* **66**, 733–736 (2012).
25. Guo, H. *et al.* Tensile ductility and necking of metallic glass. *Nat. Mater.* **6**, 735–739 (2007).
26. Jang, D. & Greer, J. R. Transition from a strong-yet-brittle to a stronger-and-ductile state by size reduction of metallic glasses. *Nat. Mater.* **9**, 215–219 (2010).
27. Luo, J. H., Wu, F. F., Huang, J. Y., Wang, J. Q. & Mao, S. X. Superelongation and atomic chain formation in nanosized metallic glass. *Phys. Rev. Lett.* **104**, (2010).
28. Dieter, G. E. *Mechanical Metallurgy*. (McGraw-Hill, 1986).
29. Menzel, B. C. & Dauskardt, R. H. The fatigue endurance limit of a Zr-based bulk metallic glass. *Scr. Mater.* **55**, 601–604 (2006).
30. Menzel, B. C. & Dauskardt, R. H. Response to comments on ‘The fatigue endurance limit of a Zr-based bulk metallic glass.’ *Scr. Mater.* **57**, 69–71 (2007).
31. Wang, G. Y., Landes, J. D., Peker, A. & Liaw, P. K. Comments on ‘The fatigue-endurance limit of a Zr-based bulk metallic glass.’ *Scr. Mater.* **57**, 65–68 (2007).
32. Ashby, M. & Greer, A. Metallic glasses as structural materials. *Scr. Mater.* **54**, 321–326 (2006).
33. Sharma, P., Kaushik, N., Kimura, H., Saotome, Y. & Inoue, A. Nano-fabrication with metallic glass—an exotic material for nano-electromechanical systems. *Nanotechnology* **18**, 035302 (2007).
34. Kumar, G., Desai, A. & Schroers, J. Bulk metallic glass: The smaller the better. *Adv. Mater.* **23**, 461–476 (2011).
35. Schroers, J., Kumar, G., Hodges, T. M., Chan, S. & Kyriakides, T. R. Bulk metallic glasses for biomedical applications. *JOM* **61**, 21–29 (2009).
36. Tian, L., Shan, Z.-W. & Ma, E. Ductile necking behavior of nanoscale metallic glasses under uniaxial tension at room temperature. *Acta Mater.* **61**, 4823–4830 (2013).
37. Pekarskaya, E., Kim, C. P. & Johnson, W. L. In situ transmission electron microscopy studies of shear bands in a bulk metallic glass based composite. *J. Mater. Res.* **16**, 2513–2518 (2011).
38. Donovan, P. E. & Stobbs, W. M. The structure of shear bands in metallic glasses. *Acta Metall.* **29**, 1419–1436 (1981).
39. Zhang, Y. & Greer, A. L. Thickness of shear bands in metallic glasses. *Appl. Phys. Lett.* **89**, 071907 (2006).
40. Greer, A. L., Cheng, Y. Q. & Ma, E. Shear bands in metallic glasses. *Mater. Sci. Eng. R Rep.* **74**, 71–132 (2013).
41. Falk, M. L. & Langer, J. S. Dynamics of viscoplastic deformation in amorphous solids. *Phys. Rev. E* **57**, 7192 (1998).
42. Argon, A. S. & Shi, L. T. Development of visco-plastic deformation in metallic glasses. *Acta Metall.* **31**, 499–507 (1983).
43. Dasgupta, R., Hentschel, H. G. E. & Procaccia, I. Microscopic mechanism of shear bands in amorphous solids. *Phys. Rev. Lett.* **109**, 255502 (2012).
44. Homer, E. R. & Schuh, C. A. Mesoscale modeling of amorphous metals by shear transformation zone dynamics. *Acta Mater.* **57**, 2823–2833 (2009).
45. Schall, P., Weitz, D. A. & Spaepen, F. Structural rearrangements that govern flow in colloidal glasses. *Science* **318**, 1895–1899 (2007).

46. Fan, Y., Iwashita, T. & Egami, T. How thermally activated deformation starts in metallic glass. *Nat. Commun.* **5**, 5083 (2014).
47. Homer, E. R. Examining the initial stages of shear localization in amorphous metals. *Acta Mater.* **63**, 44–53 (2014).
48. Srolovitz, D., Vitek, V. & Egami, T. An atomistic study of deformation of amorphous metals. *Acta Metall.* **31**, 335–352 (1983).
49. Pampillo, C. A. Localized shear deformation in a glassy metal. *Scr. Metall.* **6**, 915–917 (1972).
50. Chen, H. S., Leamy, H. J. & O'Brien, M. J. Bending deformation in metallic glasses. *Scr. Metall.* **7**, 415–419 (1973).
51. Shi, Y. & Falk, M. Strain localization and percolation of stable structure in amorphous solids. *Phys. Rev. Lett.* **95**, 095502 (2005).
52. Shi, Y. & Falk, M. L. Stress-induced structural transformation and shear banding during simulated nanoindentation of a metallic glass. *Acta Mater.* **55**, 4317–4324 (2007).
53. Cao, A. J., Cheng, Y. Q. & Ma, E. Structural processes that initiate shear localization in metallic glass. *Acta Mater.* **57**, 5146–5155 (2009).
54. Wright, W. J., Byer, R. R. & Gu, X. High-speed imaging of a bulk metallic glass during uniaxial compression. *Appl. Phys. Lett.* **102**, 241920 (2013).
55. Song, S. X. & Nieh, T. G. Direct measurements of shear band propagation in metallic glasses – An overview. *Intermetallics* **19**, 1968–1977 (2011).
56. Lewandowski, J. J. & Greer, A. L. Temperature rise at shear bands in metallic glasses. *Nat. Mater.* **5**, 15–18 (2005).
57. Liu, Z. Y., Yang, Y. & Liu, C. T. Size-affected shear-band speed in bulk metallic glasses. *Appl. Phys. Lett.* **99**, 171904 (2011).
58. Cheng, Y., Han, Z., Li, Y. & Ma, E. Cold versus hot shear banding in bulk metallic glass. *Phys. Rev. B* **80**, 134115 (2009).
59. Wang, C.-C. *et al.* Sample size matters for Al<sub>88</sub>Fe<sub>7</sub>Gd<sub>5</sub> metallic glass: Smaller is stronger. *Acta Mater.* **60**, 5370–5379 (2012).
60. Shimizu, F., Ogata, S. & Li, J. Yield point of metallic glass. *Acta Mater.* **54**, 4293–4298 (2006).
61. Zhang, Z. ., Eckert, J. & Schultz, L. Difference in compressive and tensile fracture mechanisms of Zr<sub>59</sub>Cu<sub>20</sub>Al<sub>10</sub>Ni<sub>8</sub>Ti<sub>3</sub> bulk metallic glass. *Acta Mater.* **51**, 1167–1179 (2003).
62. Wu, F. F., Zhang, Z. F. & Mao, S. X. Size-dependent shear fracture and global tensile plasticity of metallic glasses. *Acta Mater.* **57**, 257–266 (2009).
63. Mukai, T., Nieh, T. ., Kawamura, Y., Inoue, A. & Higashi, K. Dynamic response of a Pd<sub>40</sub>Ni<sub>40</sub>P<sub>20</sub> bulk metallic glass in tension. *Scr. Mater.* **46**, 43–47 (2002).
64. Lewandowski, J. J., Wang, W. H. & Greer, A. L. Intrinsic plasticity or brittleness of metallic glasses. *Philos. Mag. Lett.* **85**, 77–87 (2005).
65. Wang, W. H. The elastic properties, elastic models and elastic perspectives of metallic glasses. *Prog. Mater. Sci.* **57**, 487–656 (2012).
66. Gu, X. J., Poon, S. J., Shiflet, G. J. & Lewandowski, J. J. Ductile-to-brittle transition in a Ti-based bulk metallic glass. *Scr. Mater.* **60**, 1027–1030 (2009).

67. Gu, X. J., Poon, S. J., Shiflet, G. J. & Lewandowski, J. J. Compressive plasticity and toughness of a Ti-based bulk metallic glass. *Acta Mater.* **58**, 1708–1720 (2010).
68. Kumar, G., Prades-Rodel, S., Blatter, A. & Schroers, J. Unusual brittle behavior of Pd-based bulk metallic glass. *Scr. Mater.* **65**, 585–587 (2011).
69. Jang, D., Maaß, R., Wang, G., Liaw, P. K. & Greer, J. R. Fatigue deformation of micro-sized metallic glasses. *Scr. Mater.* **68**, 773–776 (2013).
70. Yang, B. *et al.* In-situ thermographic observation of mechanical damage in bulk-metallic glasses during fatigue and tensile experiments. *Intermetallics* **12**, 1265–1274 (2004).
71. Wang, G. Y. *et al.* Fatigue behavior of bulk-metallic glasses. *Intermetallics* **12**, 885–892 (2004).
72. Freels, M., Wang, G. Y., Zhang, W., Liaw, P. K. & Inoue, A. Cyclic compression behavior of a Cu–Zr–Al–Ag bulk metallic glass. *Intermetallics* **19**, 1174–1183 (2011).
73. Zhang, Z. F., Eckert, J. & Schultz, L. Fatigue and fracture behavior of bulk metallic glass. *Metall. Mater. Trans. A* **35**, 3489–3498 (2004).
74. Hess, P., Menzel, B. & Dauskardt, R. Fatigue damage in bulk metallic glass II: Experiments. *Scr. Mater.* **54**, 355–361 (2006).
75. Gilbert, C. J., Schroeder, V. & Ritchie, R. O. Mechanisms for fracture and fatigue-crack propagation in a bulk metallic glass. *Metall. Mater. Trans. A* **30**, 1739–1753 (1999).
76. Gilbert, C. J., Ritchie, R. O. & Johnson, W. L. Fracture toughness and fatigue-crack propagation in a Zr–Ti–Ni–Cu–Be bulk metallic glass. *Appl. Phys. Lett.* **71**, 476 (1997).
77. Launey, M. E., Busch, R. & Kruzic, J. J. Effects of free volume changes and residual stresses on the fatigue and fracture behavior of a Zr–Ti–Ni–Cu–Be bulk metallic glass. *Acta Mater.* **56**, 500–510 (2008).
78. Schroeder, V., Gilbert, C. J. & Ritchie, R. O. A comparison of the mechanisms of fatigue-crack propagation behavior in a Zr-based bulk amorphous metal in air and an aqueous chloride solution. *Mater. Sci. Eng. A* **317**, 145–152 (2001).
79. Shimizu, F., Ogata, S. & Li, J. Theory of shear banding in metallic glasses and molecular dynamics calculations. *Mater. Trans.* **48**, 2923–2927 (2007).
80. Yang, B. *et al.* Localized heating and fracture criterion for bulk metallic glasses. *J. Mater. Res.* **21**, 915–922 (2006).
81. Miracle, D. B., Concustell, A., Zhang, Y., Yavari, A. R. & Greer, A. L. Shear bands in metallic glasses: Size effects on thermal profiles. *Acta Mater.* **59**, 2831–2840 (2007).
82. Braeck, S. & Podladchikov, Y. Spontaneous thermal runaway as an ultimate failure mechanism of materials. *Phys. Rev. Lett.* **98**, 095504 (2007).
83. Manning, M., Daub, E., Langer, J. & Carlson, J. Rate-dependent shear bands in a shear-transformation-zone model of amorphous solids. *Phys. Rev. E* **79**, 016110 (2009).
84. Georgarakis, K. *et al.* Shear band melting and serrated flow in metallic glasses. *Appl. Phys. Lett.* **93**, 031907 (2008).

85. Qu, R. T., Wu, F., Zhang, Z.-F. & Eckert, J. Direct observations on the evolution of shear bands into cracks in metallic glass. *J. Mater. Res.* **24**, 3130–3135 (2011).
86. Lewandowski, J., Wang, W. & Greer, A. Intrinsic plasticity or brittleness of metallic glasses. *Philos. Mag. Lett.* **85**, 77–87 (2005).
87. Greaves, G. N., Greer, A. L., Lakes, R. S. & Rouxel, T. Poisson's ratio and modern materials. *Nat. Mater.* **10**, 823–837 (2011).
88. Anand, L. & Su, C. A theory for amorphous viscoplastic materials undergoing finite deformations, with application to metallic glasses. *J. Mech. Phys. Solids* **53**, 1362–1396 (2005).
89. Henann, D. L. & Anand, L. Fracture of metallic glasses at notches: Effects of notch-root radius and the ratio of the elastic shear modulus to the bulk modulus on toughness. *Acta Mater.* **57**, 6057–6074 (2009).
90. Poon, S. J., Zhu, A. & Shiflet, G. J. Poisson's ratio and intrinsic plasticity of metallic glasses. *Appl. Phys. Lett.* **92**, 261902 (2008).
91. Murali, P. *et al.* Atomic scale fluctuations govern brittle fracture and cavitation behavior in metallic glasses. *Phys. Rev. Lett.* **107**, 215501 (2011).
92. Kumar, G., Prades-Rodel, S., Blatter, A. & Schroers, J. Unusual brittle behavior of Pd-based bulk metallic glass. *Scr. Mater.* **65**, 585–587 (2011).
93. Knuyt, G., De Schepper, L. & Stals, L. M. Calculation of elastic constants for an amorphous metal. *Mater. Sci. Eng.* **98**, 527–529 (1988).
94. Knuyt, G. & Stals, L. M. Calculation of some metallic-glass properties, based on the use of a Gaussian distribution for the nearest-neighbour distance III. Elastic constants. *Philos. Mag. Part B* **64**, 299–315 (1991).
95. Jiang, M. Q. & Dai, L. H. Short-range-order effects on intrinsic plasticity of metallic glasses. *Philos. Mag. Lett.* **90**, 269–277 (2010).
96. Heggen, M., Spaepen, F. & Feuerbacher, M. Creation and annihilation of free volume during homogeneous flow of a metallic glass. *J. Appl. Phys.* **97**, 033506 (2005).
97. Shi, Y., Katz, M., Li, H. & Falk, M. Evaluation of the disorder temperature and free-volume formalisms via simulations of shear banding in amorphous solids. *Phys. Rev. Lett.* **98**, 185505 (2007).
98. Takeuchi, S. & Edagawa, K. Atomistic simulation and modeling of localized shear deformation in metallic glasses. *Prog. Mater. Sci.* **56**, 785–816 (2011).
99. Gu, X. J., Poon, S. J., Shiflet, G. J. & Widom, M. Ductility improvement of amorphous steels: Roles of shear modulus and electronic structure. *Acta Mater.* **56**, 88–94 (2008).
100. Cheng, Y., Ma, E. & Sheng, H. Atomic level structure in multicomponent bulk metallic glass. *Phys. Rev. Lett.* **102**, 245501 (2009).
101. Cheng, Y. Q. & Ma, E. Atomic-level structure and structure–property relationship in metallic glasses. *Prog. Mater. Sci.* **56**, 379–473 (2011).
102. Rodney, D., Tanguy, A. & Vandembroucq, D. Modeling the mechanics of amorphous solids at different length scale and time scale. *Model. Simul. Mater. Sci. Eng.* **19**, 083001 (2011).
103. Falk, M. L. & Maloney, C. E. Simulating the mechanical response of amorphous solids using atomistic methods. *Eur. Phys. J. B* **75**, 405–413 (2010).

104. Luo, J. & Shi, Y. Tensile fracture of metallic glasses via shear band cavitation. *Acta Mater.* **82**, 483–490 (2015).
105. Deng, D., Argon, A. S. & Yip, S. Simulation of plastic deformation in a two-dimensional atomic glass by molecular dynamics IV. *Philos. Trans. R. Soc. Math. Phys. Eng. Sci.* **329**, 613–640 (1989).
106. Yamamoto, R., Matsuoka, H. & Doyama, M. A three-dimensional computer simulation for the tensile deformation of amorphous iron. *Phys. Status Solidi A* **51**, 163–172 (1979).
107. Kobayashi, S., Maeda, K. & Takeuchi, S. Computer simulation of deformation of amorphous Cu<sub>57</sub>Zr<sub>43</sub>. *Acta Metall.* **28**, 1641–1652 (1980).
108. Tsamados, M., Tanguy, A., Goldenberg, C. & Barrat, J.-L. Local elasticity map and plasticity in a model Lennard-Jones glass. *Phys. Rev. E* **80**, 026112 (2009).
109. Widmer-Cooper, A. & Harrowell, P. Predicting the long-time dynamic heterogeneity in a supercooled liquid on the basis of short-time heterogeneities. *Phys. Rev. Lett.* **96**, 185701 (2006).
110. Manning, M. L. & Liu, A. J. Vibrational modes identify soft spots in a sheared disordered packing. *Phys. Rev. Lett.* **107**, 108302 (2011).
111. Ding, J., Patinet, S., Falk, M. L., Cheng, Y. & Ma, E. Soft spots and their structural signature in a metallic glass. *Proc. Natl. Acad. Sci.* **111**, 14052–14056 (2014).
112. Peng, H. L., Li, M. Z. & Wang, W. H. Structural signature of plastic deformation in metallic glasses. *Phys. Rev. Lett.* **106**, 135503 (2011).
113. Wakeda, M., Shibutani, Y., Ogata, S. & Park, J. Relationship between local geometrical factors and mechanical properties for Cu–Zr amorphous alloys. *Intermetallics* **15**, 139–144 (2007).
114. Tanaka, H., Kawasaki, T., Shintani, H. & Watanabe, K. Critical-like behaviour of glass-forming liquids. *Nat. Mater.* **9**, 324–331 (2010).
115. Rodney, D. & Schuh, C. Distribution of thermally activated plastic events in a flowing glass. *Phys. Rev. Lett.* **102**, 235503 (2009).
116. Shi, Y. F. & Falk, M. L. Atomic-scale simulations of strain localization in three-dimensional model amorphous solids. *Phys. Rev. B* **73**, 214201 (2006).
117. Argon, A. S. & Demkowicz, M. J. What can plasticity of amorphous silicon tell us about plasticity of metallic glasses? *Metall. Mater. Trans. A* **39**, 1762–1778 (2008).
118. Maloney, C. & Lemaître, A. Amorphous systems in athermal, quasistatic shear. *Phys. Rev. E* **74**, 016118 (2006).
119. Lundberg, M., Krishan, K., Xu, N., O’Hern, C. S. & Dennin, M. Reversible plastic events in amorphous materials. *Phys. Rev. E* **77**, 041505 (2008).
120. Falk, M. Molecular-dynamics study of ductile and brittle fracture in model noncrystalline solids. *Phys. Rev. B* **60**, 7062–7070 (1999).
121. Zhao, P., Li, J. & Wang, Y. Heterogeneously randomized STZ model of metallic glasses: Softening and extreme value statistics during deformation. *Int. J. Plast.* **40**, 1–22 (2013).
122. Zhao, P., Li, J. & Wang, Y. Extended defects, ideal strength and actual strengths of finite-sized metallic glasses. *Acta Mater.* **73**, 149–166 (2014).
123. Rycroft, C. & Bouchbinder, E. Fracture toughness of metallic glasses: Annealing-induced embrittlement. *Phys. Rev. Lett.* **109**, 194301 (2012).

124. Wahnström, G. Molecular-dynamics study of a supercooled two-component Lennard-Jones system. *Phys. Rev. A* **44**, 3752–3764 (1991).
125. Stillinger, F. H. & Weber, T. A. Computer simulation of local order in condensed phases of silicon. *Phys. Rev. B* **31**, 5262 (1985).
126. Cheng, Y. & Ma, E. Configurational dependence of elastic modulus of metallic glass. *Phys. Rev. B* **80**, 064104 (2009).
127. Spaepen, F. Metallic glasses: Must shear bands be hot? *Nat. Mater.* **5**, 7–8 (2006).
128. Cameron, K. & Dauskardt, R. Fatigue damage in bulk metallic glass I: Simulation. *Scr. Mater.* **54**, 349–353 (2006).
129. Shi, Y., Louca, D., Wang, G. & Liaw, P. K. Compression-compression fatigue study on model metallic glass nanowires by molecular dynamics simulations. *J. Appl. Phys.* **110**, 023523 (2011).
130. Shi, Y., Luo, J., Yuan, F. & Huang, L. Intrinsic ductility of glassy solids. *J. Appl. Phys.* **115**, 043528 (2014).
131. Frenkel, D. *Understanding Molecular Simulation: From Algorithms to Applications Ch. 4* (Academic Press, San Diego, 2002).
132. Allen, M. P. & Tildesley, D. J. *Computer Simulation of Liquids Ch. 3* (Oxford Univ. Press, Oxford, 1989).
133. Lindorff-Larsen, K., Piana, S., Dror, R. O. & Shaw, D. E. How Fast-Folding Proteins Fold. *Science* **334**, 517–520 (2011).
134. Abraham, F. F. *et al.* Simulating materials failure by using up to one billion atoms and the world’s fastest computer: Brittle fracture. *Proc. Natl. Acad. Sci.* **99**, 5777–5782 (2002).
135. Finnis, M. W. & Sinclair, J. E. A simple empirical  $N$ -body potential for transition metals. *Philos. Mag. A* **50**, 45–55 (1984).
136. Kob, W. Testing mode-coupling theory for a supercooled binary Lennard-Jones mixture I: The van Hove correlation function. *Phys. Rev. E* **51**, 4626–4641 (1995).
137. Mendeleev, M. I., Sordelet, D. J. & Kramer, M. J. Using atomistic computer simulations to analyze x-ray diffraction data from metallic glasses. *J. Appl. Phys.* **102**, 043501 (2007).
138. Ackland, G. J., Mendeleev, M. I., Srolovitz, D. J., Han, S. & Barashev, A. V. Development of an interatomic potential for phosphorus impurities in  $\alpha$ -iron. *J. Phys. Condens. Matter* **16**, S2629–S2642 (2004).
139. Stillinger, F. H. & Weber, T. A. Computer simulation of local order in condensed phases of silicon. *Phys. Rev. B* **31**, 5262–5271 (1985).
140. Nosé, S. A unified formulation of the constant temperature molecular dynamics methods. *J. Chem. Phys.* **81**, 511 (1984).
141. Hoover, W. Canonical dynamics: Equilibrium phase-space distributions. *Phys. Rev. A* **31**, 1695–1697 (1985).
142. Parrinello, M. Polymorphic transitions in single crystals: A new molecular dynamics method. *J. Appl. Phys.* **52**, 7182 (1981).
143. Van Beest, B., Kramer, G. & van Santen, R. Force-fields for silicas and aluminophosphates based on abinitio calculations. *Phys. Rev. Lett.* **64**, 1955–1958 (1990).
144. Wahnstrom, G. Molecular-dynamics study of a supercooled 2-component Lennard-Jones system. *Phys Rev A* **44**, 3752–3764 (1991).

145. Steeb, S. & Lamparter, P. Structure of binary metallic glasses. *J Non-Cryst Solids* **156**, 24–33 (1993).
146. Giessen, B. C., Madhava, M., Polk, D. E. & Vandersande, J. Refractory amorphous inter-transition metal-alloys. *Mater Sci Eng* **23**, 145–150 (1976).
147. Shi, Y. F. & Falk, M. L. Structural transformation and localization during simulated nanoindentation of a noncrystalline metal film. *Appl. Phys. Lett.* **86**, 011914 (2005).
148. Shi, Y. F. Size-independent shear band formation in amorphous nanowires made from simulated casting. *Appl. Phys. Lett.* **96**, 121909 (2010).
149. Dzугutov, M. Glass-formation in a simple monatomic liquid with icosahedral inherent local order. *Phys. Rev. A* **46**, R2984–R2987 (1992).
150. Dzугutov, M., Simdyankin, S. I. & Zetterling, F. H. M. Decoupling of diffusion from structural relaxation and spatial heterogeneity in a supercooled simple liquid. *Phys. Rev. Lett.* **89**, 195701 (2002).
151. Dzугutov, M. Formation of a dodecagonal quasi-crystalline phase in a simple monatomic liquid. *Phys. Rev. Lett.* **70**, 2924–2927 (1993).
152. Moriarty, J. Density-functional formulation of the generalized pseudopotential theory. II. *Phys. Rev. B* **26**, 1754–1780 (1982).
153. Moriarty, J. Density-functional formulation of the generalized pseudopotential theory. III. Transition-metal interatomic potentials. *Phys. Rev. B* **38**, 3199–3231 (1988).
154. Moriarty, J. & Widom, M. First-principles interatomic potentials for transition-metal aluminides: Theory and trends across the 3d series. *Phys. Rev. B* **56**, 7905–7917 (1997).
155. Hausleitner, C. & Hafner, J. Hybridized nearly-free-electron tight-binding-bond approach to interatomic forces in disordered transition-metal alloys. I. Theory. *Phys. Rev. B* **45**, 115 (1992).
156. Demkowicz, M. J. & Argon, A. S. High-density liquidlike component facilitates plastic flow in a model amorphous silicon system. *Phys Rev Lett* **93**, 025505 (2004).
157. Molinero, V., Sastry, S. & Angell, C. A. Tuning of tetrahedrality in a silicon potential yields a series of monatomic (metal-like) glass formers of very high fragility. *Phys. Rev. Lett.* **97**, 075701–4 (2006).
158. Fusco, C., Albaret, T. & Tanguy, A. Role of local order in the small-scale plasticity of model amorphous materials. *Phys. Rev. E* **82**, 066116 (2010).
159. Pugh, S. F. XCII. Relations between the elastic moduli and the plastic properties of polycrystalline pure metals. *Philos. Mag.* **45**, 823 (1954).
160. Rouxel, T., Ji, H., Guin, J. P., Augereau, F. & Rufflé B. Indentation deformation mechanism in glass: Densification versus shear flow. *J. Appl. Phys.* **107**, 094903 (2010).
161. Falk, M. L. Molecular-dynamics study of ductile and brittle fracture in model noncrystalline solids. *Phys. Rev. B* **60**, 7062–7070 (1999).
162. Nose, S. A unified formulation of the constant temperature molecular-dynamics methods. *J Chem Phys* **81**, 511–519 (1984).
163. Hoover, W. G. Canonical dynamics - equilibrium phase-space distributions. *Phys. Rev. A* **31**, 1695–1697 (1985).

164. Xiao, Q., Sheng, H. W. & Shi, Y. Dominant shear bands observed in amorphous ZrCuAl nanowires under simulated compression. *MRS Commun.* **2**, 13–16 (2012).
165. Yuan, F. & Huang, L. Molecular dynamics simulation of amorphous silica under uniaxial tension: From bulk to nanowire. *J. Non-Cryst. Solids* **358**, 3481–3487 (2012).
166. Shi, Y. F. & Falk, M. L. Stress-induced structural transformation and shear banding during simulated nanoindentation of a metallic glass. *Acta Mater.* **55**, 4317–4324 (2007).
167. Tian, L. *et al.* Approaching the ideal elastic limit of metallic glasses. *Nat. Commun.* **3**, 609 (2012).
168. Cheng, Y. Q. & Ma, E. Intrinsic shear strength of metallic glass. *Acta Mater.* **59**, 1800–1807 (2011).
169. Rice, J. Dislocation nucleation from a crack tip - an analysis based on the Peierls concept. *J. Mech. Phys. Solids* **40**, 239–271 (1992).
170. Shi, Y. F., Katz, M. B., Li, H. & Falk, M. L. Evaluation of the disorder temperature and free-volume formalisms via simulations of shear banding in amorphous solids. *Phys. Rev. Lett.* **98**, 185505 (2007).
171. Manning, M. L., Langer, J. S. & Carlson, J. M. Strain localization in a shear transformation zone model for amorphous solids. *Phys. Rev. E* **76**, 056106–16 (2007).
172. Greer, A. L., Cheng, Y. Q. & Ma, E. Shear bands in metallic glasses. *Mater. Sci. Eng. R Rep.* **74**, 71–132 (2013).
173. Scott, G. D. & Kilgour, D. M. The density of random close packing of spheres. *J. Phys. Appl. Phys.* **2**, 863–866 (1969).
174. Makishima, A. & Mackenzie, J. D. Calculation of bulk modulus, shear modulus and Poisson's ratio of glass. *J. Non-Cryst. Solids* **17**, 147–157 (1975).
175. Zwanzig, R. & Mountain, R. D. High-frequency elastic moduli of simple fluids. *J. Chem. Phys.* **43**, 4464 (1965).
176. Ericksen, J. L. on the Cauchy--Born rule. *Math. Mech. Solids* **13**, 199–220 (2008).
177. Wu, Z., Zhang, Y.-W., Jhon, M. H., Gao, H. & Srolovitz, D. J. Nanowire failure: long = brittle and short = ductile. *Nano Lett.* **12**, 910–914 (2012).
178. Schuh, C. A., Hufnagel, T. C. & Ramamurty, U. Mechanical behavior of amorphous alloys. *Acta Mater.* **55**, 4067–4109 (2007).
179. Shimizu, F., Ogata, S. & Li, J. Yield point of metallic glass. *Acta Mater.* **54**, 4293–4298 (2006).
180. Cheng, Y. Q., Han, Z., Li, Y. & Ma, E. Cold versus hot shear banding in bulk metallic glass. *Phys. Rev. B* **80**, 134115 (2009).
181. Rouxel, T., Ji, H., Hammouda, T. & Moréac, A. Poisson's ratio and the densification of glass under high pressure. *Phys. Rev. Lett.* **100**, 225501 (2008).
182. Novikov, V. N. & Sokolov, A. P. Poisson's ratio and the fragility of glass-forming liquids. *Nature* **431**, 961–963 (2004).
183. Yannopoulos, S. N. & Johari, G. P. Glass behaviour: Poisson's ratio and liquid's fragility. *Nature* **442**, E7–E8 (2006).
184. Egami, T., Poon, S. J., Zhang, Z. & Keppens, V. Glass transition in metallic glasses: A microscopic model of topological fluctuations in the bonding network. *Phys. Rev. B* **76**, 024203 (2007).

185. Turnbull, D. & Cohen, M. H. Free-volume model of the amorphous phase: Glass transition. *J. Chem. Phys.* **34**, 120 (1961).
186. Spaepen, F. A microscopic mechanism for steady state inhomogeneous flow in metallic glasses. *Acta Metall.* **25**, 407–415 (1977).
187. Shi, Y. & Falk, M. L. Structural transformation and localization during simulated nanoindentation of a noncrystalline metal film. *Appl. Phys. Lett.* **86**, 011914 (2005).
188. Schall, P. & van Hecke, M. Shear bands in matter with granularity. *Annu. Rev. Fluid Mech.* **42**, 67–88 (2010).
189. Lemaître, A. Rearrangements and dilatancy for sheared dense materials. *Phys. Rev. Lett.* **89**, 195503 (2002).
190. Argon, A. S., Megusar, J. & Grant, N. J. Shear band induced dilations in metallic glasses. *Scr. Metall.* **19**, 591–596 (1985).
191. Megusar, J., Argon, A. S. & Grant, N. J. Plastic flow and fracture in Pd80Si20 near T<sub>g</sub>. *Mater. Sci. Eng.* **38**, 63–72 (1979).
192. Klaumünzer, D. *et al.* Probing shear-band initiation in metallic glasses. *Phys. Rev. Lett.* **107**, 185502 (2011).
193. Pan, J., Chen, Q., Liu, L. & Li, Y. Softening and dilatation in a single shear band. *Acta Mater.* **59**, 5146–5158 (2011).
194. Guan, P., Lu, S., Spector, M. J. B., Valavala, P. K. & Falk, M. L. Cavitation in amorphous solids. *Phys. Rev. Lett.* **110**, 185502 (2013).
195. Murali, P., Narasimhan, R., Guo, T. F., Zhang, Y. W. & Gao, H. J. Shear bands mediate cavitation in brittle metallic glasses. *Scr. Mater.* **68**, 567–570 (2013).
196. Viasnoff, V. & Lequeux, F. Rejuvenation and overaging in a colloidal glass under shear. *Phys. Rev. Lett.* **89**, 065701 (2002).
197. Lacks, D. & Osborne, M. Energy landscape picture of overaging and rejuvenation in a sheared glass. *Phys. Rev. Lett.* **93**, 255501 (2004).
198. Guan, P., Chen, M. & Egami, T. Stress-temperature scaling for steady-state flow in metallic glasses. *Phys. Rev. Lett.* **104**, 205701 (2010).
199. Cheng, Y. Q. & Ma, E. Intrinsic shear strength of metallic glass. *Acta Mater.* **59**, 1800–1807 (2011).
200. Plimpton, S. Fast parallel algorithms for short-range molecular dynamics. *J. Comput. Phys.* **117**, 1–19 (1995).
201. Albano, F. & Falk, M. L. Shear softening and structure in a simulated three-dimensional binary glass. *J. Chem. Phys.* **122**, 154508 (2005).
202. Haruyama, O. *et al.* Volume and enthalpy relaxation in Zr55Cu30Ni5Al10 bulk metallic glass. *Acta Mater.* **58**, 1829–1836 (2010).
203. Polk, D. & Turnbull, D. Flow of melt and glass forms of metallic alloys. *Acta Metall.* **20**, 493–498 (1972).
204. Shi, Y. & Falk, M. Atomic-scale simulations of strain localization in three-dimensional model amorphous solids. *Phys. Rev. B* **73**, 214201 (2006).
205. Jiang, W. H., Pinkerton, F. E. & Atzmon, M. Mechanical behavior of shear bands and the effect of their relaxation in a rolled amorphous Al-based alloy. *Acta Mater.* **53**, 3469–3477 (2005).
206. Li, J., Wang, Z. & Hufnagel, T. Characterization of nanometer-scale defects in metallic glasses by quantitative high-resolution transmission electron microscopy. *Phys. Rev. B* **65**, 144201 (2002).

207. Yang, B. *et al.* Dynamic evolution of nanoscale shear bands in a bulk-metallic glass. *Appl. Phys. Lett.* **86**, 141904 (2005).
208. Klaumünzer, D., Maaß, R. & Löffler, J. F. Stick-slip dynamics and recent insights into shear banding in metallic glasses. *J. Mater. Res.* **26**, 1453–1463 (2011).
209. Liu, Y. *et al.* Thermodynamic origins of shear band formation and the universal scaling law of metallic glass strength. *Phys. Rev. Lett.* **103**, 065504 (2009).
210. Langer, J. & Manning, M. Steady-state, effective-temperature dynamics in a glassy material. *Phys. Rev. E* **76**, 056107 (2007).
211. Fujita, K. *et al.* Effects of loading rates, notch root radius and specimen thickness on fracture toughness in bulk metallic glasses. *J. Alloys Compd.* **434-435**, 22–27 (2007).
212. Gao, Y. F., Wang, L., Bei, H. & Nieh, T. G. On the shear-band direction in metallic glasses. *Acta Mater.* **59**, 4159–4167 (2011).
213. Demkowicz, M. & Argon, A. High-density liquidlike component facilitates plastic flow in a model amorphous silicon system. *Phys. Rev. Lett.* **93**, 025505 (2004).
214. Molinero, V., Sastry, S. & Angell, C. A. Tuning of tetrahedrality in a silicon potential yields a series of monatomic (metal-like) glass formers of very high fragility. *Phys. Rev. Lett.* **97**, 075701 (2006).
215. Varias, A. G., Suo, Z. & Shih, C. F. Ductile failure of a constrained metal foil. *J. Mech. Phys. Solids* **39**, 963–986 (1991).
216. Tvergaard, V. Failure by ductile cavity growth at a metal-ceramic interface. *Acta Metall. Mater.* **39**, 419–426 (1991).
217. He, M. Y., Evans, A. G. & Hutchinson, J. W. Interface cracking phenomena in constrained metal layers. *Acta Mater.* **44**, 2963–2971 (1996).
218. Demetriou, M. D. *et al.* A damage-tolerant glass. *Nat. Mater.* **10**, 123–128 (2011).
219. Xi, X. *et al.* Fracture of brittle metallic glasses: brittleness or plasticity. *Phys. Rev. Lett.* **94**, 125510 (2005).
220. Wang, G. *et al.* Nanoscale periodic morphologies on the fracture surface of brittle metallic glasses. *Phys. Rev. Lett.* **98**, 235501 (2007).
221. Murali, P. *et al.* Atomic scale fluctuations govern brittle fracture and cavitation behavior in metallic glasses. *Phys. Rev. Lett.* **107**, 215501 (2011).
222. Qu, R. T., Stoica, M., Eckert, J. & Zhang, Z. F. Tensile fracture morphologies of bulk metallic glass. *J. Appl. Phys.* **108**, 063509 (2010).
223. Qu, R. T., Eckert, J. & Zhang, Z. F. Tensile fracture criterion of metallic glass. *J. Appl. Phys.* **109**, 083544 (2011).
224. Chen, Y., Jiang, M. Q., Wei, Y. J. & Dai, L. H. Failure criterion for metallic glasses. *Philos. Mag.* **91**, 4536–4554 (2011).
225. Furukawa, A. & Tanaka, H. Violation of the incompressibility of liquid by simple shear flow. *Nature* **443**, 434–438 (2006).
226. Furukawa, A. & Tanaka, H. Inhomogeneous flow and fracture of glassy materials. *Nat. Mater.* **8**, 601–609 (2009).
227. Pauly, S., Gorantla, S., Wang, G., Kühn, U. & Eckert, J. Transformation-mediated ductility in CuZr-based bulk metallic glasses. *Nat. Mater.* **9**, 473–477 (2010).
228. Müller-Plathe, F. A simple nonequilibrium molecular dynamics method for calculating the thermal conductivity. *J. Chem. Phys.* **106**, 6082 (1997).

229. Li, H., Fan, C., Choo, H. & Liaw, P. K. Temperature-dependent mechanical property of Zr-Based metallic glasses. *Mater. Trans.* **48**, 1752–1754 (2007).
230. Davies, T. J. & Ogburn, A. A. A possible route to improving the ductility of brittle intermetallic compounds. *J. Alloys Compd.* **228**, 105–111 (1995).
231. Chen, M. A brief overview of bulk metallic glasses. *NPG Asia Mater.* **3**, 82–90 (2011).
232. Kumar, G., Tang, H. X. & Schroers, J. Nanomoulding with amorphous metals. *Nature* **457**, 868–872 (2009).
233. Hofmann, D. C. *et al.* Designing metallic glass matrix composites with high toughness and tensile ductility. *Nature* **451**, 1085–1089 (2008).
234. Kim, J.-Y., Jang, D. & Greer, J. R. Nanolaminates utilizing size-dependent homogeneous plasticity of metallic glasses. *Adv. Funct. Mater.* **21**, 4550–4554 (2011).
235. Brothers, A. H. & Dunand, D. C. Ductile bulk metallic glass foams. *Adv. Mater.* **17**, 484–486 (2005).
236. Launey, M. E., Hofmann, D. C., Johnson, W. L. & Ritchie, R. O. Solution to the problem of the poor cyclic fatigue resistance of bulk metallic glasses. *Proc. Natl. Acad. Sci.* **106**, 4986–4991 (2009).
237. Packard, C. E., Witmer, L. M. & Schuh, C. A. Hardening of a metallic glass during cyclic loading in the elastic range. *Appl. Phys. Lett.* **92**, 171911 (2008).
238. Deng, C. & Schuh, C. A. Atomistic mechanisms of cyclic hardening in metallic glass. *Appl. Phys. Lett.* **100**, 251909 (2012).
239. Wang, C.-C. *et al.* Real-time, high-resolution study of nanocrystallization and fatigue cracking in a cyclically strained metallic glass. *Proc. Natl. Acad. Sci.* **110**, 19725–19730 (2013).
240. Shi, Y. Size-independent shear band formation in amorphous nanowires made from simulated casting. *Appl. Phys. Lett.* **96**, 121909 (2010).
241. Dzugutov, M. Glass formation in a simple monatomic liquid with icosahedral inherent local order. *Phys. Rev. A* **46**, R2984–R2987 (1992).
242. Menzel, B. C. & Dauskardt, R. H. Fatigue damage initiation and growth from artificial defects in Zr-based metallic glass. *Acta Mater.* **56**, 2955–2965 (2008).
243. Chuang, C.-P. *et al.* Fatigue-induced damage in Zr-Based bulk metallic glasses. *Sci. Rep.* **3**, 2578 (2013).
244. Polák, J., Obrtlík, K., Hájek, M. & Vavšek, A. Cyclic stress-strain response of polycrystalline copper in a wide range of plastic strain amplitudes. *Mater. Sci. Eng. A* **151**, 19–27 (1992).
245. Polak, J. & Vasek, A. Fatigue damage in polycrystalline copper below the fatigue limit. *Int. J. Fatigue* **16**, 403–408 (1994).
246. Cheng, A. S. & Laird, C. The high cycle fatigue life of copper single crystals tested under plastic-strain-controlled conditions. *Mater. Sci. Eng.* **51**, 55–60 (1981).
247. Winter, A. T. Etching studies of dislocation microstructures in crystals of copper fatigued at low constant plastic strain amplitude. *Philos. Mag.* **28**, 57–64 (1973).
248. Manson, S. S. & Dolan, T. J. Thermal stress and low cycle fatigue. *J. Appl. Mech.* **33**, 957 (1966).
249. Vinogradov, A. *et al.* Cyclic response of ultrafine-grained copper at constant plastic strain amplitude. *Scr. Mater.* **36**, 1345–1351 (1997).

250. Tomida, T. & Egami, T. Molecular-dynamics study of structural anisotropy and anelasticity in metallic glasses. *Phys. Rev. B* **48**, 3048–3057 (1993).
251. Zhang, Y., Mattern, N. & Eckert, J. Study of structural anisotropy in Cu<sub>50</sub>Zr<sub>45</sub>Al<sub>5</sub> metallic glass under uniaxial compression by molecular dynamics simulations. *Intermetallics* **30**, 154–157 (2012).
252. Srolovitz, D., Vitek, V. & Egami, T. An atomistic study of deformation of amorphous metals. *Acta Metall.* **31**, 335–352 (1983).